AD A080963

AFML-TR-79-4188

PROPERTY SCREENING AND EVALUATION OF CERAMIC TURBINE ENGINE MATERIALS

D. C. LARSEN

IIT Research Institute
Chicago, Illinois 60616

DTIC
ELECTE
FEB 2 7 1980

C

OCTOBER 1979

TECHNICAL REPORT AFML-TR-79-4188
Final Report for Period 1 July 1975 - 1 August 1979

Approved for public release; distribution unlimited.

AIR FORCE MATERIALS LABORATORY
AIR FORCE WRIGHT AERONAUTICAL LABORATORIES
AIR FORCE SYSTEMS COMMAND
WRIGHT-PATTERSON AIR FORCE BASE, OHIO 45433

80 2 25 023

ROBERT RUH
Project Engineer

FOR THE COMMANDER

HENRY C. GRAHAM
Chief
Processing and High Temperature Materials Branch
Metals and Ceramics Division

REPORT DOCUMENTATION PAGE		READ INSTRUCTIONS BEFORE COMPLETING FORM
1. REPORT NUMBER AFML-TR-79-4188	2. GOVT ACCESSION NO.	3. RECIPIENT'S CATALOG NUMBER
4. TITLE (and Subtitle) Property Screening and Evaluation of Ceramic Turbine Engine Materials		5. TYPE OF REPORT & PERIOD COVERED Final Technical Report, 1 July 1975 — 1 Aug 1979
		6. PERFORMING ORG. REPORT NUMBER AFML-TR-79-4188
7. AUTHOR(s) D.C. Larsen IIT Research Institute Chicago, Illinois 60616		8. CONTRACT OR GRANT NUMBER(s) F33615-75-C-5196
9. PERFORMING ORGANIZATION NAME AND ADDRESS IIT Research Institute Chicago, Illinois 60616		10. PROGRAM ELEMENT, PROJECT, TASK AREA & WORK UNIT NUMBERS ILIR0069
11. CONTROLLING OFFICE NAME AND ADDRESS Air Force Materials Laboratory Processing & High Temperature Materials Branch Metals and Ceramics Division, AFML/LLM		12. REPORT DATE October 79
		13. NUMBER OF PAGES 151
14. MONITORING AGENCY NAME & ADDRESS(If different from Controlling Office)		15. SECURITY CLASS. (of this report) Unclassified
		15a. DECLASSIFICATION/DOWNGRADING SCHEDULE

16. DISTRIBUTION STATEMENT (of this Report)

Approved for public release; distribution unlimited.

17. DISTRIBUTION STATEMENT (of the abstract entered in Block 20, if different from Report)

18. SUPPLEMENTARY NOTES

19. KEY WORDS (Continue on reverse side if necessary and identify by block number)

Turbine Ceramics   Mechanical Properties
Silicon Nitride   Thermal Properties
Silicon Carbide
Silicon-Base Ceramics

20. ABSTRACT (Continue on reverse side if necessary and identify by block number)

An overview is presented of the pertinent thermal and mechanical properties of 26 structural silicon-base non-oxide ceramics that are candidates for advanced heat engine applications. Included are hot pressed, sintered and reaction sintered Si_3N_4 and SiC, and Sialon. Data are presented for flexure strength, elastic properties, strength degradation at long times due to subcritical crack growth, long term oxidation effects, creep resistance, fracture toughness, thermal expansion, thermal diffusivity, and thermal shock resistance. All materials are evaluated using the same test equipment so

DD FORM 1473 1 JAN 73   EDITION OF 1 NOV 65 IS OBSOLETE

that valid comparisons can be made between materials. Emphasis is placed on predominant behavioral trends as related to material microstructure and purity as determined by processing method. Structure-property relations are developed.

FOREWORD

IITRI is greatly appreciative of the many organizations that have supplied test samples or material billets to this program. The support of the DOE (S. M. Wander, for fracture surface analysis) and the Navy (I. Machlin, for slow crack growth studies) is gratefully acknowledged. Special thanks are given to the following people for helpful discussions: Robert Ruh, H. C. Graham, R. W. Rice, S. W. Freiman, M. G. Mendiratta, P. L. Land, S. A. Bortz, and Y. Harada.

IITRI personnel who have contributed to this program include J. L. Sievert and B. Norikane (flexure properties and computer data base maintenance), W. R. Logan (creep test, exposure), H. H. Nakamura (thermal expansion, thermal shock), G. C. Walther (fracture toughness), G. Jeka (creep testing), T. B. Wade (test fixture design), and J. Adams (microscopy).

TABLE OF CONTENTS

LIST OF ILLUSTRATIONS

PROPERTY SCREENING AND EVALUATION OF CERAMIC TURBINE ENGINE MATERIALS

SECTION I

INTRODUCTION

Structural ceramics are candidates for use in severe-environment applications such as encountered in advanced systems including gas turbines using "clean" or coal-derived fuels for stationary or vehicular power generation, military aircraft, gasifiers, heat exchangers, etc. Such utilization of ceramics offers several potential advantages, including increased efficiency, decreased weight, lower life cycle cost, and decreased complexity through the use of non-cooled components. For ceramics to become a reality in such applications, various requirements must be met including: the development of overall life prediction methodology; employment of realistic design methodology; and demonstration of fabrication process feasibility for the required ceramic component configurations.

The biggest challenges for designers in using ceramics include: dealing with the statistical nature of these brittle materials; low fracture toughness and surface sensitivity; the existence of subcritical crack growth; the lack of data regarding the environmental effects of oxidation, corrosion, erosion, and deposition from fuel; batch-to-batch variability resulting from inadequate process control; and lack of an NDE technology capable of detecting critical strength-limiting flaws.

These challenges are compounded by the fact that new candidate materials for advanced heat engine applications are continually emerging, and their properties are strongly dependent on microstructure, purity, and processing history. It is for this reason that this program was established. The purpose of this program is to support various current systems design efforts through the comprehensive screening characterization

1

of a wide variety of silicon-base ceramics that have potential use as components in high temperature gas turbines, radomes and other high performance/severe environment applications. Silicon nitride and silicon carbide, in hot-pressed, reaction bonded, and pressureless sintered forms are currently the most promising materials for these applications.

In this program thermal and mechanical property data are generated on candidate materials and the results are interpreted with respect to microstructure, purity, secondary phases, and environmental effects. Failure modes and the nature of the critical strength-controlling flaws are being determined by SEM and optical fractography. Structure-property relations are developed, and generated data are compared to literature data.

This report summarizes and overviews the pertinent properties obtained on twenty-six (26) silicon-base ceramics that are candidates for advanced heat engine applications. Emphasis is placed on predominant behavioral trends for each material type to aid in material selection. Details of this work are found in the widely distributed semiannual interim technical reports issued on this program.

This properties screening and evaluation work is a continuing effort in this laboratory. A follow-on program with the same objectives and scope has been initiated (AFML Contract F33615-79-C-5100). In the continuing work both new materials and new versions of previously evaluated materials are included. In the new program, all generated property data will be compared to and correlated with data generated on the present program. Since these two programs overlap, some data analysis conducted on the present materials will be presented early in the follow-on program.

SECTION II

MATERIALS

A wide variety of silicon-base ceramics have emerged
during recent years that have potential application as
components in high temperature gas turbines and other advanced
heat engines. Silicon nitride and silicon carbide, in hot-
pressed, reaction bonded, and pressureless sintered forms are
currently the most promising materials for this application.
These materials range from commercially available (which in
most cases are in a continual state of development), to highly
developmental. Also, certain materials have been specifically
developed for lower cost, less stringent applications. Thus,
the intended application and the processing maturity must be
considered when comparing materials performance.

Available Si_3N_4 and SiC bodies represent a large family
of materials with wide property variation and broad response
characteristics during interaction with severe environments.
Even though some are termed commercially available, they are in
a continual state of development and change. In general,
property differences between materials of a given type are
directly related to: 1) existence of secondary phases, 2)
purity, 3) microstructural aspects such as pore size and
distribution, grain size, etc., 4) oxidation rates, 5) phase
stability, 6) microstructural stability, 7) existence of
subcritical crack growth, and 8) the nature of the critical
strength-controlling flaws (e.g., contaminant inclusions,
pores/pore agglomerates, large grains, unreacted particles,
impurity particles, etc.) and how the critical flaws change
with time, temperature, and environmental exposure.

Table 1 contains a listing of all materials evaluated on
this program arranged according to material type (excluding
various developmental AFML materials). All materials, with
the exception of the Norton materials investigated early in
the program (NC-132, NC-435, NC-350) were supplied without
charge by the respective manufacturers. In cases where material
billets rather than as-sintered or machined test samples were

3

TABLE 1

MATERIALS EVALUATED TO DATE ON IITRI/AFML PROGRAM
(Contract F33615-75-C-5196)

A. Hot-Pressed Si_3N_4

- Norton NC-132 HP-Si_3N_4 (1% MgO)

- Norton NCX-34 HP-Si_3N_4 (8% Y_2O_3)

- Harbison-Walker HP-Si_3N_4 (10% CeO_2)

- Kyocera SN-3 HP-Si_3N_4

- Naval Research Laboratory HP-Si_3N_4 + ZrO_2 Compositions
  (4-16 wt.% ZrO_2)

- Ceradyne Ceralloy 147A, HP-Si_3N_4 (1% MgO)

- Ceradyne Ceralloy 147Y, HP-Si_3N_4 (15% Y_2O_3)

- Ceradyne Ceralloy 147Y-1, HP-Si_3N_4 (8% Y_2O_3)

B. Sintered Si_3N_4

- Kyocera SN-205 Sintered Si_3N_4

- Kyocera SN-201 Sintered Si_3N_4

- GTE Sylvania Sintered Si_3N_4 + 6% Y_2O_3

C. Reaction Sintered Si_3N_4

- Norton NC-350 RS-Si_3N_4

- Kawecki-Berylco RS-Si_3N_4

- Ford Injection Molded RS-Si_3N_4

- AiResearch Slip-Cast RS-Si_3N_4 (Airceram RBN-101)

- Raytheon Isopressed RS-Si_3N_4

- Indussa/Nippon Denko RS-Si_3N_4

- AiResearch Injection Molded RS-Si_3N_4 (Airceram RBN-122)

- Norton NC-350 RS-Si_3N_4 (new improved)

TABLE 1 (contd)

D. **SiC Materials**

  ● Norton NC-435 Siliconized SiC

  ● General Electric Boron-Doped Sintered β-SiC

  ● Carborundum Sintered α-SiC

  ● UKAEA/British Nuclear Fuels Refel Si/SiC
    (diamond ground & as-processed)

  ● Ceradyne Ceralloy 146A, HP-SiC (2% Al_2O_3)

  ● Ceradyne Ceralloy 146I, HP-SiC (2% B_4C)

  ● Norton NC-203 HP-SiC ($\sim$2% Al_2O_3)

E. **Other Materials**

  ● AFML-General Electric SiAlON Materials
    (GE-129 & GE-130)

  ● Various AFML Developmental Si_3N_4 Materials

  ● Corning Glass Pyroceram 9606 Glass-Ceramic

supplied, AFML has arranged for machining under a separate contract.

Table 2 contains density and machining information on all materials, as well as the date each material was received. The date received is important since several materials are termed commercially available, but are actually still being developed. Some materials have undergone various processing improvements recently which have resulted in improved properties. The two Norton NC-350 entries in Table 2 are an example of this. The indication of the date received thus permits an assessment of the performance of the material as determined in this program, with respect to its maturity level. Some suppliers consider their material originally supplied to this program "old," and thus have supplied new upgraded versions (e.g., Norton NC-350). It is expected that this will continue with other manufacturers as improved processing techniques yield upgraded materials.

TABLE 2

ADDITIONAL MATERIALS INFORMATION

Material	Sample ID Code, 1st letter	Bulk Density, gm/cc	Surface Finish, μin. rms	Comments[a]	Date Received
1 Norton NC-132 HP-Si_3N_4 (1% MgO)	1	3.18	12	Diamond ground at Norton	11/75
2 Norton NCX-34 HP-Si_3N_4 (8% Y_2O_3)	5	3.37	15	Diamond ground at Bomas	8/77
3 Harbison-Walker HP-Si_3N_4 (10% CeO_2)	H	3.34	5	Supplied diamond ground	7/77
4 Kyocera SN-3 HP-Si_3N_4	A	3.06	8	Supplied diamond ground	2/77
5 Norton NC-435 Si/SiC	4	2.96	5	Diamond ground at Norton	1/76
6 Carborundum Sintered α-SiC	8	3.16	10	Supplied diamond ground	3/77
7 General Electric Sintered SiC	G	3.04	12	Supplied diamond ground	2/77
8 UKAEA/BNF Refel Si/SiC	U	3.11	8	Supplied diamond ground (designated batch 1 in material ID notation)	5/77
9 Kyocera SN-201 Sintered Si_3N_4	B	3.00	15	Supplied diamond ground	2/77
10 Kyocera SN-205 Sintered Si_3N_4	2	2.81	20	Supplied diamond ground	2/77
11 Norton NC-350 RS-Si_3N_4	3	2.41-2.55	6	Diamond ground at Norton	1/76

7

TABLE 2 (cont.)

Material	Sample ID Code, 1st letter	Bulk Density, gm/cc	Surface Finish, μin. rms	Comments[a]	Date Received
12 Kawecki-Berylco RS-Si$_3$N$_4$	K	2.35- 2.53	20- 60	Supplied as-fabricated, diamond ground as reqd. to meet dimension spec.	6/76
13 AiResearch (slip-cast) RS-Si$_3$N$_4$ (RBN-101)	7	2.85	16	Diamond ground at Bomas	8/77
14 Ford (injection molded) RS-Si$_3$N$_4$	F	2.75	29	Supplied as-sintered	8/77
15 Raytheon (iso-pressed) RS-Si$_3$N$_4$	6	2.43	10- 30	Supplied rough ground; ultrasonic machined at Bullen; finish diamond ground at IITRI.	3/77
16 Indussa/Nippon Denko RS-Si$_3$N$_4$	N	2.08	110	Diamond ground at AFML (very porous material)	7/77
17 Naval Res. Lab. HP-Si$_3$N$_4$ + 4-16 w/o ZrO$_2$	R	3.1- 3.4	8	Supplied diamond ground	3/77
18 Ceradyne Ceralloy 147A HP-Si$_3$N$_4$ (1% MgO)	X	3.22	20	Diamond ground at Bomas	11/77
19 Ceradyne Ceralloy 147Y HP-Si$_3$N$_4$ (15% Y$_2$O$_3$)	Z	3.37	18	Diamond ground at Bomas	11/77
20 Ceradyne Ceralloy 147Y-1 HP-Si$_3$N$_4$ (8% Y$_2$O$_3$)	Y	3.29	15	Diamond ground at Bomas	11/77
21 GTE Sylvania Sintered Si$_3$N$_4$ (6% Y$_2$O$_3$)	C	3.23	12	Supplied diamond ground	6/78
22 AiResearch (injection molded) RS-Si$_3$N$_4$ (RBN-122)	9	2.66	50- 80	Supplied as processed	11/77

8

TABLE 2 (concluded)

Material	Sample ID Code, 1st letter	Bulk Density, gm/cc	Surface Finish, μin. rms	Comments[a]	Date Received
23 Norton NC-350 RS-Si_3N_4 (new generation)	3	2.38	22	As-nitrided (designated batch 6 in IITRI sample ID notation)	~ 6/77
24 UKAEA/BNF Refel Si/SiC (as-processed)	U	3.09	40-70	Supplied as-processed (designated batch 2)	11/77
25 Ceradyne Ceralloy 146A HP-SiC (2% Al_2O_3)	V	3.22	18	Diamond ground at Bomas	11/77
26 Ceradyne Ceralloy 146I HP-SiC (2% B_4C)	W	3.21	15	Diamond ground at Bomas	11/77

[a]All diamond machined specimens were longitudinally ground (i.e., parallel to the tensile axis of the test bar). Norton refers to Morton Company, Worcester, MA. Bomas refers to Bomas Machine Specialties, Inc., Boston, MA. Bullen refers to Bullen Ultrasonics Company, Eaton, OH.

9

SECTION III
TEST PLAN

Tables 3, 4, and 5 present the various pre- and post-test characterization parameters and general test matrix for this program. For any given material the specific tests that are conducted are a function of number of test samples available, expected properties (determines specific test temperatures), and intended use of the material. In general, tests are conducted at room temperature to establish a baseline, and in the appropriate elevated temperature range where the properties (e.g., strength) are expected to begin to change rapidly (i.e., $T > 1000°C$). All testing is being performed in air. The maximum test temperature is $1500°C$. For strength behavior it is important to recognize this as a screening effort where the typical test sample population is five to ten for any given test temperature.

TABLE 3

PRE-TEST CHARACTERIZATION PARAMETERS

- Density-Porosity Characterization

- Microstructural Analysis

- Impurity Content
  - Cations- Spectrographic (AFML)
  - Oxygen - Neutron Activation Analysis (AMMRC)

- Ultrasonic NDE Inspection

- Phase Identification - XRD (AFML)

- X-radiographic Inspection (AFML)

- Surface Finish.

TABLE 4

SCREENING TESTS CONDUCTED[a]

- Flexural Strength-Modulus (4 point), Stress-Strain
  (25°C, 1000°-1500°C)

- Fracture Toughness
  - Double Torsion (selected materials)
  - Controlled Flaw (primarily) (25°C, 1000-1500°C)

- Creep (stepwise) (1300°-1500°C)

- Stress Rupture (selected samples) (1300°-1500°C)

- Long Term Oxidation Exposure (100 and 1000 hr at ~1400°C)
  Residual Strength at 25°C, microstructural changes

- Thermal Expansion (25-1500°C)

- Thermal Diffusivity (25°C, 800-1500°C)

- Thermal Shock
  - Water Quench/Internal Friction/Residual Strength
  - Analytical Thermal Stress Resistance Parameters

- Hot Gas Exposure-Fatigue (NASA-Lewis) (selected samples)

- Dynamic Young's Modulus (room temperature, selected samples
  to elevated temperatures)

- Tensile Strength, Modulus (Norton NC-132 HP-Si_3N_4 at 25°C)

- Microstructural Stability after various exposures

- Slow Crack Growth Evaluated on Selected Materials Using
  Differential Strain Rate Tests, with Prediction of very
  Long Time Stress Rupture Behavior (sponsored by Navy)
  (1200°-1500°C).

---

[a]Tests conducted in air atmosphere.

TABLE 5

POST-TEST ANALYSIS

- Correlation of Properties

- Comparison with Literature Data

- Establish Structure-Property Relations

- Interpretation of Mechanisms

- Failure Mode Analysis, Identification of Critical Flaws by Fractographic Techniques. Performed on Virgin and Exposed Flexural Test Bars Broken at 25°C and at Elevated Temperatures.

SECTION IV

MATERIALS CHARACTERIZATION

Materials characterization parameters include X-ray phase identification and spectrographic metallic impurity analysis (both performed by AFML). Table 6 compiles the phases present in the materials studied to date, as determined by X-ray diffraction. Spectrographic impurity analysis results are presented in Table 7. Elements present in quantity < 0.2% were measured by emission spectrographic analysis. Quantitative wet chemical analysis was employed to determine the amount of the elements present in quantities > 0.2%. Oxygen analysis of these materials is presently being conducted at USAMMRC.

TABLE 6

X-RAY DIFFRACTION ANALYSIS RESULTS

Material	Phases Present	
	Major	Minor
Norton NC-132 HPSN	β-Si_3N_4	Si_2N_4O
Norton NCX-34 HPSN	β-Si_3N_4	$Y_2O_3 \cdot Si_3N_4$
Harbison-Walker HPSN	β-Si_3N_4	α-Si_3N_4
Kyocera SN-3 HPSN	β-Si_3N_4	α-Si_3N_4, Si_2N_2O
Ceradyne 147A HPSN	β-Si_3N_4	
Ceradyne 147Y-1 HPSN	β-Si_3N_4	
Ceradyne 147Y HPSN	β-Si_3N_4	$YSiO_2N$
Norton NC-350 RSSN	α-Si_3N_4	β-Si_3N_4
KBI RSSN	a	a
KBI RSSN	α-Si_3N_4	β-Si_3N_4
Ford IMRS-SN	α-Si_3N_4	β-Si_3N_4
AiResearch SCRS-SN	a	a
Raytheon IPRS-SN	α-Si_3N_4	β-Si_3N_4
Indussa/Nippon Denko RSSN	α-Si_3N_4	β-Si_3N_4
AiResearch IMRS-SN	α-Si_3N_4	β-Si_3N_4
Kyocera SN-205 SSN	β-Si_3N_4	α-Si_3N_4
Kyocera SN-201 SSN	β-Si_3N_4	
Carborundum SSC	α-SiC (I, III, and/or IV)	
General Electric SSC	β-SiC	
Norton NC-435 Si/SiC	α-SiC	Si
UKAEA/BNF Refel Si/SiC	α-SiC (I, III, and/or IV)	Si
Ceradyne 146A HPSC	α-SiC (I, III, and/or IV)	
Ceradyne 146I HPSC	α-SiC (I, III, and/or IV)	

[a]Approximately equal amounts of α-Si_3N_4 and β-Si_3N_4.

15

TABLE 7

METALLIC IMPURITY ANALYSIS[a]

| Material | Weight Percent Element[b] | | | | | | | | | Total Wt% Metallic Impurities incl. Trace Elements |
	Al	Fe	Mn	Cr	Ca	Mg	B	W	Others	
	Hot-Pressed Si_3N_4									
Norton NCK-34 (8% Y_2O_3)	0.3	0.5	0.05	0.02	0.05			2.25	0.15Co	3.6% + 5.3% Y
Harbison-Walker (10% CeO_2)	0.53	0.6			0.1	0.005		0.1		1.3% + 7% Ce
Norton NC-132 (1% MgO)	0.17	0.55	0.05	0.02	0.04	0.84		2.1	0.20Co	4%
Kyocera SN-3	2.6	1.4-1.9	0.04	0.1	0.2-0.33	1.9-2.3			0.1Na, 0.23K	7%
Ceradyne (1% MgO)	0.5	0.77	.014		0.22	0.7		0.31		2.5-4.6%
Ceradyne (8% Y_2O_3)	1.0	1.4	0.03		0.17	0.1				2.6% + 6% Y
Ceradyne (15% Y_2O_3)	1.0	1.1	0.024		0.18					2.3% + 12.4% Y
	Hot-Pressed SiC									
Ceradyne (2% Al_2O_3)	1.0	0.44			<0.1		0.1	0.43	0.06Co	2.1-3.9%
Ceradyne (2% B_4C)	1.5	0.1					0.92			2.5-3.3%
	Si/SiC									
UKAEA/BNF Refel (diamond ground)		0.27								0.3% + Si
UKAEA/BNF Refel (as-processed)	0.1	0.58								0.6-0.7% + Si
Norton NC-435	0.14	0.4	0.05		0.02	0.02		<0.02		0.65% + Si

16

TABLE 7 (cont.)

Material	Al	Fe	Mn	Cr	Ca	Mg	B	W	Others	Total Wt% Metallic Impurities incl. Trace Elements
				Sintered SiC						
Carborundum (α-SiC)	0.06-0.09	0.18-0.27					0.41	0.07		0.6%
General Electric (β-SiC)	0.1	0.19-0.29					0.42-0.47	1.1-1.2	.075Co	1.9-2.5%
				Sintered Si_3N_4						
Kyocera SN-201	3.5-3.8	1.3-1.8	0.03	0.1	0.25-0.39	2.1-2.6				6-8.6%
Kyocera SN-205	4.9-5.0	1.4-2.3	0.04	0.1	0.25-0.45	2.4-3.2				5-11%
				Reaction Sintered Si_3N_4						
Norton NC-350 (original batch 1)	0.14	0.4	0.05	0.02	0.04	0.01		<0.02		0.7%
KBI	0.15-0.2	0.41-0.61	0.02	<0.1	0.13-0.17	0.02		0.02		0.8-2%
AiResearch (SC)	0.25	1.1								1.4%
Ford (IM)	0.1	1.0	0.1							1.2%
Raytheon (IP)	0.95	1.3								2.3%
Indussa/Nippon Denko	0.43	0.4		0.1	0.25					1.2%
AiResearch (IM)	0.54	1.1	0.016		0.029					1.4-1.7%

[a] Emission spectrographic analysis for elements present in quantity <0.2%; quantitative wet chemical analysis for elements >0.2%. Does not include oxygen and unreacted silicon impurities.

[b] Elements present in amount <0.1 wt% usually not recorded, but appear as trace elements in the summed total of metallic impurities.

17

SECTION V

FLEXURE STRENGTH, ELASTIC MODULUS, AND STRESS-STRAIN BEHAVIOR

Silicon-base non-oxide ceramics that are candidates for advanced heat engine applications are the various forms of Si_3N_4 and SiC that are available. Their properties are related to microstructure and purity, which are determined by processing technique and starting powders.

5.1 General Behavior of Silicon-Base Ceramics

Silicon nitride materials include hot-pressed, sintered, and reaction bonded forms. Hot-pressed materials are highly dense and thus have excellent room-temperature properties. The room temperature 4-point bend strength can be as high as 130 ksi. However, the oxide densification aids employed result in oxide secondary phases at grain boundaries that degrade properties at elevated temperature (T>1200°C). It is generally believed that a significant strength decrease at elevated temperatures in hot-pressed materials (oxide doped) is caused by plasticity in intergranular regions which leads to grain boundary sliding. This promotes subcritical crack growth, thereby allowing flaws to grow during loading, which means that the critical stress intensity is reached at a lower macroscopic stress than if the cracks were not able to grow. Magnesia-doped $HP-Si_3N_4$ is the most common, but recently yttria, zirconia, and ceria-based materials have been developed in an effort to create a more refractory, more deformation-resistant grain boundary phase. However, the potential of improved high-temperature properties using dopants such as Y_2O_3 has not been consistently observed in all Y_2O_3, CeO_2, or ZrO_2 doped materials. In the case of Y_2O_3-doped $HP-Si_3N_4$, this has been attributed to the formation of unstable $Y_2O_3 \cdot Si_3N_4$ phases. Materials with these additions are still in relatively early developmental stages compared to MgO-doped $HP-Si_3N_4$. Thus, their optimum processing parameters are not yet established, their behavior is not as well understood, and their full potential has probably not yet been attained.

18

Reaction-sintered Si_3N_4 has the potential of fabrication to near net shape, presently an economical advantage in a complex turbine part. These materials are more porous than hot-pressed materials and thus have lower strengths at low temperatures (typically 30-40 ksi). However, the reaction sintering process involves lower impurity concentrations and a purer product results. The lack of significant oxide grain boundary phases accounts for the extremely good properties of reaction bonded Si_3N_4 at temperatures as high as 1500°C (typically 40-50 ksi with linear stress-strain behavior). Current developmental efforts involve ways of increasing density (and thereby strength) without sacrificing purity.

Sintered silicon nitride (conventional, pressureless sintered) materials are more dense than reaction bonded materials due to the use of oxide sintering aids. However, the oxide additives affect the high temperature properties in a manner similar to the oxide densification aids used in hot-pressing Si_3N_4. This is particularly true if Al_2O_3 and/ or MgO is used as a sintering aid. Recent notable developments in sintered Si_3N_4 involve the use of Y_2O_3 dopants (typically 6-8%). This material shows much promise.

Silicon carbides have high modulus ($\sim 60 \times 10^6$ psi) and intermediate strength (nominally 50-70 ksi) relative to silicon nitrides. SiC is fabricated in silicon infiltrated, sintered, and hot pressed forms. The high temperature behavior of the siliconized SiC materials is primarily controlled by the amount and distribution of the free silicon phase present. This phase, typically present in 5-15 vol.%, limits the upper use temperatures of such self-bonded materials to T<1300°C. The sintered forms of SiC evaluated are extremely dense and pure and show particular promise at temperatures at and above 1500°C (and possibly for long time use). Sintered SiC maintains its strength to 1500°C (~ 60 ksi) and exhibits linear stress-strain behavior. Hot-pressed SiC exhibits high room temperature strength (100 ksi). Densification is usually attained through the use of $\sim 2\%$ Al_2O_3 or B_4C as a processing additive. The

19

resultant intergranular phases lead to increasing non-linear
stress-strain and strength reduction as temperatures approach
1500°C.

5.2 Properties at Room Temperature

The room temperature 4-point bend strengths and relaxed
elastic moduli (determined with strain gages) for all Si_3N_4
materials evaluated on this program are compiled in Table 8.
Sample populations were typically seven to ten. Strength data
are plotted as a function of bulk density and volume fraction
porosity in Figs. 1 and 2, respectively. Density (and thus
strength) generally increases with respect to processing method
in the following progression: reaction sintered with few
additives, reaction sintered with iron additives, sintered with
oxide additives, hot-pressed with magnesia additive, and finally
hot-pressed with yttria additive. A least-squares regression
of the linearized form of the exponential strength-porosity
relation $\sigma = \sigma_o e^{-bp}$ gives

$$\sigma = 90.6e^{-5.65P} \tag{1}$$

as shown in Fig. 2. The strength behavior of the twenty-three
(23) hot-pressed, sintered, and reaction bonded Si_3N_4 materials
is well described by the strength-porosity data fit. This
empirical strength-porosity relation is not strictly valid at
low porosity, however, even though it accurately describes the
strength of the high density hot-pressed materials in this region.
This is the case because the fracture strength of the hot-pressed
materials is not expected to be related directly to porosity
as it is for the lower density sintered and reaction-bonded
materials. That is, the critical strength-controlling flaws
in the lower density materials are expected to be pores or pore
clusters, while fracture sources in high density hot-pressed
materials have been traced to large grains, metal inclusions,
unreacted particles, surface or subsurface machining damage, or
a single isolated pore not affecting the overall density.

TABLE 8

SUMMARY OF ROOM-TEMPERATURE POROSITY, STRENGTH, AND ELASTIC MODULUS DATA FOR VARIOUS Si_3N_4 MATERIALS

SYMBOL	MATERIAL	BULK DENSITY (gm/cc)	THEORETICAL DENSITY[a]	P VOLUME FRACTION POROSITY	ROOM TEMPERATURE 4-POINT FLEX.[c] STRENGTH KSI	RELAXED ROOM TEMPERATURE YOUNG'S[b] MODULUS 10^6 psi
○	Norton NC-132 HP-Si_3N_4 (MgO) Batch 1	3.177	3.2	.007	90.91	48.4
○	Norton NC-132 HP-Si_3N_4 (MgO) Batch 2	3.186	3.2	.004	115.21	45.7
■	Kyocera SN-205 Sintered Si_3N_4	2.801	3.2	.125	37.77	27.9
◇	Norton NC-350 RB-Si_3N_4 (Diamond Ground) Batch 1	2.523	3.2	.212	30.87	25.5
◇	Norton NC-350 RB-Si_3N_4 (Diamond Ground) Batch 2	2.396	3.2	.251	23.53	23.5
◇	Norton NC-350 RB Si_3N_4 (Diamond Ground) Batch 3	2.539	3.2	.207	33.96	27.7
▲	Norton MCX-34 HP-Si_3N_4 + 8% Y_2O_3	3.372	3.391	.006	126.73	48.6
△	Raytheon Isopressed RS-Si_3N_4	2.447	3.2	.235	21.55	23.8
◆	AiResearch Slip-Cast RS-Si_3N_4	2.862	3.2	.106	37.92	32.0
◆	Kyocera SM-3 HP-Si_3N_4	3.072	3.2	.04	74.86	36.6
◆	Kyocera SM-201 Sintered Si_3N_4	3.005	3.2	.061	49.61	34.4
◆	Ford Injection Molded RS-Si_3N_4	2.742	3.2	.143	38.18	30.7
◆	Harbison-Walker HP-Si_3N_4 + 10% CeO_2	3.327	3.387	.018	76.78	46.9
○	Kawecki-Berylco RS-Si_3N_4 Batch 1	2.509	3.2	.216	23.27	21.5
○	Kawecki-Berylco RS-Si_3N_4 Batch 2	2.454	3.2	.233	21.80	21.1
○	Kawecki-Berylco RS-Si_3N_4 Batch 3	2.349	3.2	.266	18.08	20.0
●	Indussa/Nippon Denko RS-Si_3N_4	2.084	3.2	.349	10.58	11.9
△	AiResearch Injection Molded RS-Si_3N_4	2.660	2.2	.169	32.58	30.2
●	GTE Laboratories Sintered Si_3N_4 + 6% Y_2O_3	3.256	3.271	.005	78.00	42.1
●	Ceradyne Ceralloy 147A, HP-Si_3N_4 + 1% MgO	3.221	3.2	.001	87.09	47.9
●	Ceradyne Ceralloy 147-Y-1, HP-Si_3N_4 + 8% Y_2O_3	3.289	3.295	.002	83.25	45.4
●	Ceradyne Ceralloy 147-Y, HP-Si_3N_4 + 15% Y_2O_3	3.369	3.383	.004	87.85	44.7
◆	Norton NC-350 RB-Si_3N_4 (as-fired) Batch 6[c]	2.385	3.20	.255	42.09	---

a NOTE: The theoretical density of all sintered and react'on bonded Si_3N_4 materials was assumed to be 3.200 gm/cc. The theoretical density of the HP-Si_3N_4 + .1% MgO materials was also assumed to be 3.200 gm/cc. The theoretical density of the Y_2O_3 - and CeO_2 doped HPSN was computed from the nominal chemical composition assuming $\rho(CeO_2)$ = 7.13 and $\rho(Y_2O_3)$ = 5.01. The only exception to this is for MCX-34, which contains .2% tungsten; the composition of MCX-34 was assumed to be 88% Si_3N_4 + 9% Y_2O_3 + 3% WC. The assumptions on the other Y_2O_3 - and - CeO_2-doped materials will be reviewed when spectrographic analyses are complete.

b Young's modulus determined with strain gages in 4-point flexure.

c The as-fired Norton NC-350 is an upgraded version of the original diamond ground NC-350 RS-Si_3N_4
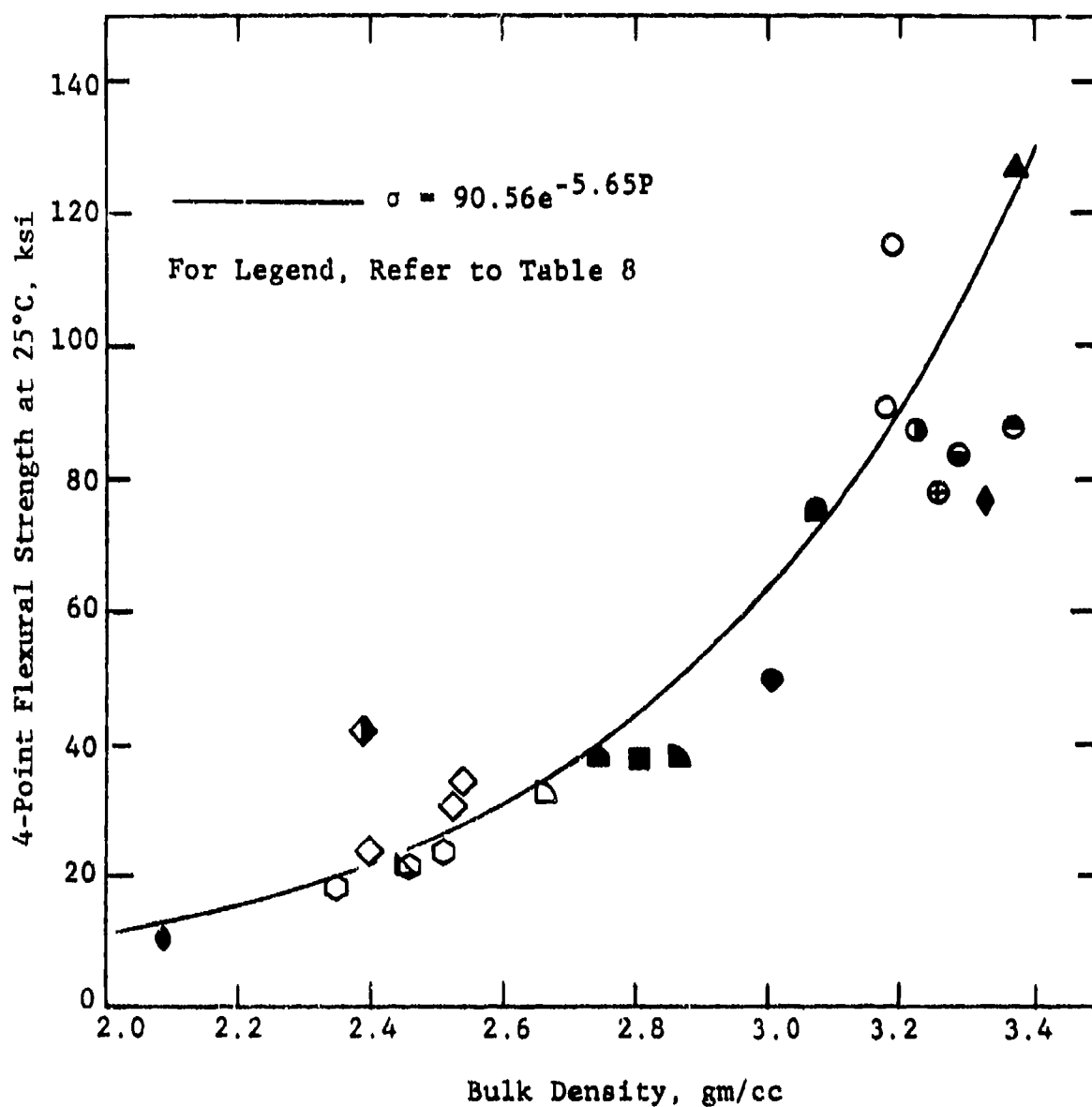
Figure 1. Room-Temperature Flexural Strength vs. Bulk Density for Various Si_3N_4 Materials

22
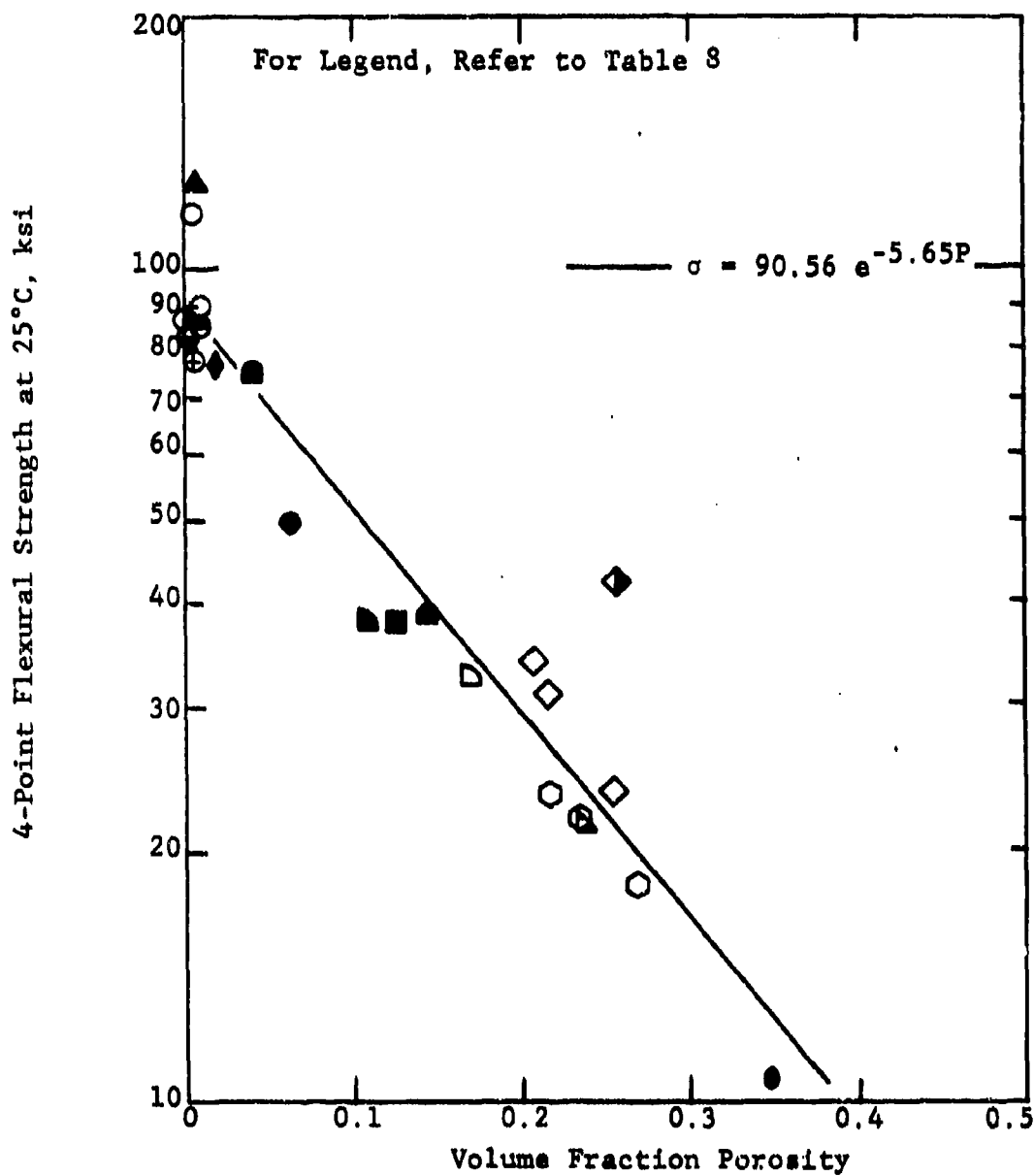
Figure 2. Room-Temperature Flexural Strength vs. Volume
Fraction Porosity for Various Si_3N_4 Materials

23

Fracture surface analysis has been conducted on this
program with a 6-60X stereoscopic optical microscope with
photographic attachment. The objective of this examination
was to attempt to identify the general nature of the fracture
sources (more detailed SEM/EDX examination on these materials
will be reported on Contract F33615-79-C-5100). Norton
NC-132 HP-Si$_3$N$_4$ was clearly the most processing-mature material
in that the fracture sources that could be identified were
predominantely machining-induced flaws at the (diamond-ground)
surface. All other hot-pressed materials exhibited fracture
sources consisting of inclusions and other subsurface processing
defects. Kyocera SN-3 HPSN had the most processing defects,
with many inclusion particles present throughout the structure.
The reaction sintered silicon nitride materials exhibited
fracture sources consisting of inclusions, pores, and pore
agglomerates, i.e., predominantly processing defects where the
fracture source could be located. Norton NC-350 has extremely
uniform microstructure and many fracture sources were not
detectable with the low-power optical microscope. Of those
fracture origins that were identified, most were pores and
pore agglomerates. Only a few inclusions were observed.
Mendiratta[1] has conducted a more detailed SEM analysis of the
fracture surfaces of the NC-350 test bars. It was found that
NC-350 RS-Si$_3$N$_4$ exhibited a relatively uniform distribution of
2-5 μm pores, and occasional 10-20 μm pores/pore agglomerates.
Pores and pore agglomerates were the most dominant fracture-
originating flaws.

Reaction sintered materials from Ford, AiResearch (RBN-
101), and Raytheon exhibited fracture sources consisting of
inclusion particles and pores. The fracture origins in
Indussa/Nippon-Denko RS-Si$_3$N$_4$ were mainly large voids, but two
types of large inclusions were also identified to be present
at many locations throughout the structure. AiResearch Airceram
RBN-122 showed occasional bands of (presumably) unreacted
silicon. Fracture sources were mainly inclusion particles
with some origins being voids. It is interesting to note that

24

for all of the above-mentioned RS-Si$_3$N$_4$ materials except NC-350, a substantial number of the fracture origins were inclusions. Referring to Table 7 it is illustrated that all these materials had significantly greater Fe impurity than did NC-350. Presumably, these materials are doped with more iron than NC-350, which results in Fe-rich inclusions acting as fracture sources.

The RS-Si$_3$N$_4$ material from Kawecki-Berylco (KBI) had the same high purity as NC-350, but much lower fracture strength. The most dominant fracture origins were pores and pore agglomerates. Much unreacted silicon material was present, either in bands or within areas of high porosity. Mendiratta[1] frequently observed such pores that contain unreacted material to be of size ~50 μm. This unreacted silicon was observed to exude from the sample surface in some 1500°C flexure tests (the melting point of silicon is 1410°C). As discussed in Section XI, it is believed that the presence of the unreacted material in KBI RS-Si$_3$N$_4$ was responsible for the higher than expected thermal diffusivity values obtained.

It is especially interesting to note in Figs. 1 and 2 the single datum for a "new improved" version of Norton NC-350 RS-Si$_3$N$_4$ (tested in the as-fired condition) which falls distinctly above the trend line, i.e., symbol ◆. This is an indication of the achievement of significant processing improvements in reaction sintering technology. More of this new generation NC-350 material will be evaluated on Contract F33615-79-C-5100.

The relaxed elastic moduli obtained during flexure testing of all Si$_3$N$_4$ materials are plotted as a function of porosity in Fig.3 (data compiled in Table 8). The dynamic moduli (obtained by a flexural resonant frequency method) of all Si$_3$N$_4$ materials are compiled in Table 9 (where the static moduli are repeated for comparison). The 25°C relaxed and dynamic elastic moduli for all Si$_3$N$_4$ materials are plotted as a function of volume fraction porosity in Fig. 4. Good agreement is obtained between the static and dynamic moduli at room temperature.

25
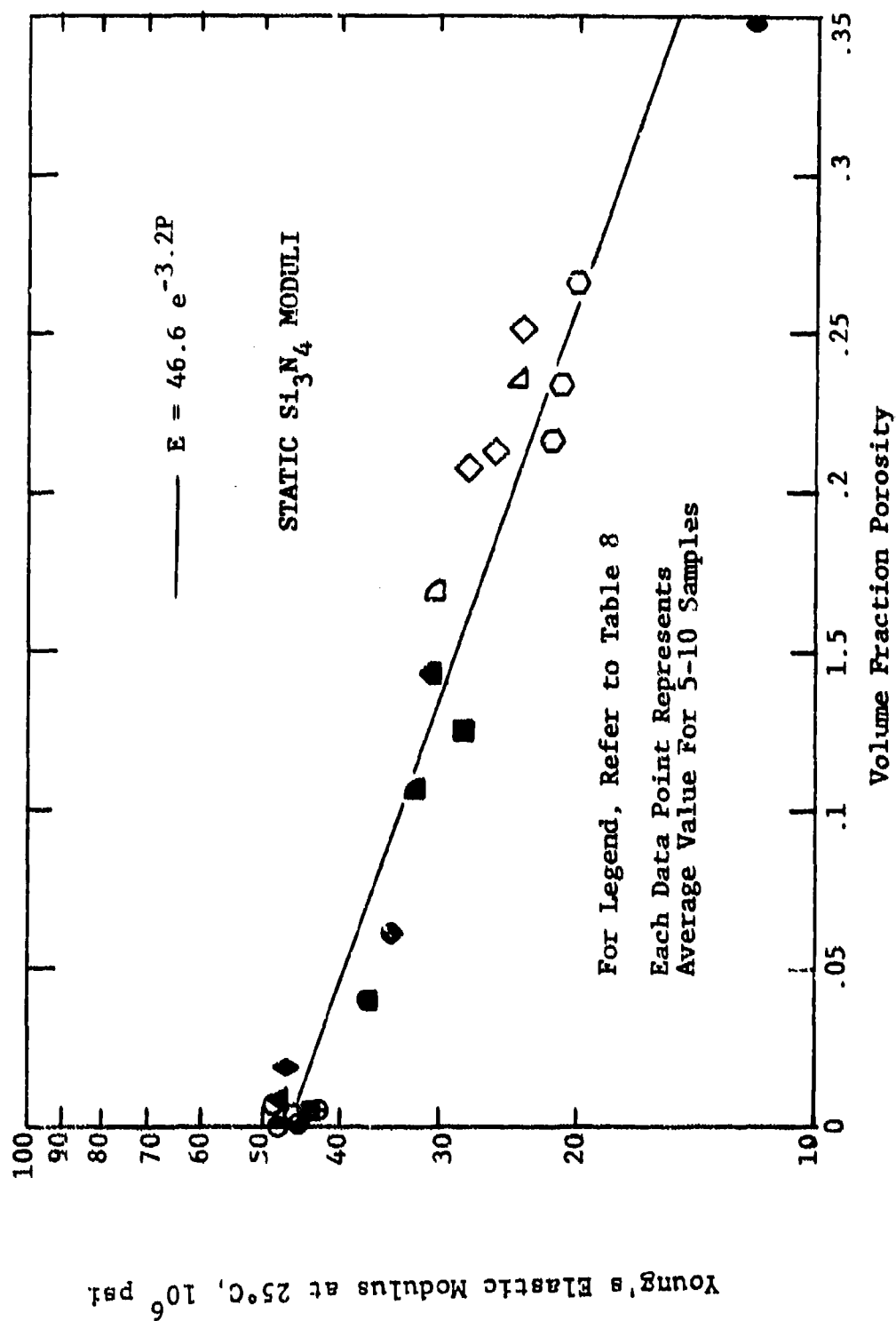
Figure 3. Room-Temperature Elastic Modulus vs. Porosity for Various Si_3N_4 Materials

26

TABLE 9

SUMMARY OF ROOM-TEMPERATURE RELAXED AND DYNAMIC ELASTIC MODULUS DATA FOR VARIOUS Si_3N_4 MATERIALS

SYMBOL FOR DYNAMIC MODULUS IN Figure 4	Material	Bulk Density (sonic) (gm/cc) [a]	Theo Density [b]	Volume Fraction Porosity [a]	Young's Modulus (sonic) 10⁶ psi [d]	Static Young's Modulus and (bulk density) 10⁶ psi [c]
◆	Norton NC-132 HP-Si₃N₄ + 1% MgO (Batch 1)	3.177	3.2	.007	45.0	48.4 (3.177)
◆	Norton NC-132 HP-Si₃N₄ + 1% MgO (Batch 2)	3.162	3.2	.012	44.5	45.7 (3.186)
▲	Norton NCX-34, HP-Si₃N₄ + 8% Y₂O₃	3.386	3.391	.001	44.5	48.6 (3.372)
△	Ceradyne Ceralloy 147-A, HP-Si₃N₄ + 1% MgO	3.312	3.2	0	45.8	47.9 (3.221)
◻	Ceradyne Ceralloy 147-Y, HP-Si₃N₄ + 15% Y₂O₃	3.370	3.383	.004	41.6	44.7 (3.369)
◇	Ceradyne Ceralloy 147-Y-1, HP-Si₃N₄ + 8% Y₂O₃	3.218	3.295	.023	42.8	45.4 (3.289)
◇	Kyocera SN-3 HP-Si₃N₄	3.060	3.2	.044	35.9	36.6 (3.072)
◀	Kyocera SN-201 Sintered Si₃N₄	2.994	3.2	.064	34.7	34.4 (3.005)
◐	Kyocera SN-205 Sintered Si₃N₄	2.819	3.2	.119	27.6	27.9 (2.801)
◓	Norton NC-350 RS-Si₃N₄ (Batch 1)	2.470	3.2	.228	25.6	25.5 (2.523)
⊕	Norton NC-350 RS-Si₃N₄ (Batch 2)	2.392	3.2	.253	22.7	23.5 (2.396)
●	Norton NC-350 RS-Si₃N₄ (Batch 3)	2.524	3.2	.211	26.8	27.7 (2.539)
●	Kawecki-Berylco (KBI) RS-Si₃N₄ (Batch 1)	2.325	3.2	.273	18.6	21.5 (2.509)
◗	KBI RS-Si₃N₄ (Batch 2)	2.347	3.2	.267	18.8	21.1 (2.454)
○	KBI RS-Si₃N₄ (Batch 3)	2.432	3.2	.240	23.1	20.0 (2.349)
▼	Ford (IM) RS-Si₃N₄	2.762	3.2	.137	28.3	30.7 (2.742)
▽	AiResearch (SC) RS-Si₃N₄	2.881	3.2	.099	31.4	32.0 (2.862)
▽	AiResearch (IM) RS-Si₃N₄	2.646	3.2	.173	26.6	30.2 (2.660)
◻	Raytheon (IP) RS-Si₃N₄	2.492	3.2	.249	21.5	23.8 (2.447)

a Average values for dynamic modulus samples
b Theoretical density computed for nominal chemical composition
c Determined with strain gage transducers during 4-point flexure strength test at 0.02 in.
d Dynamic elastic modulus determined by flexural resonant frequency method
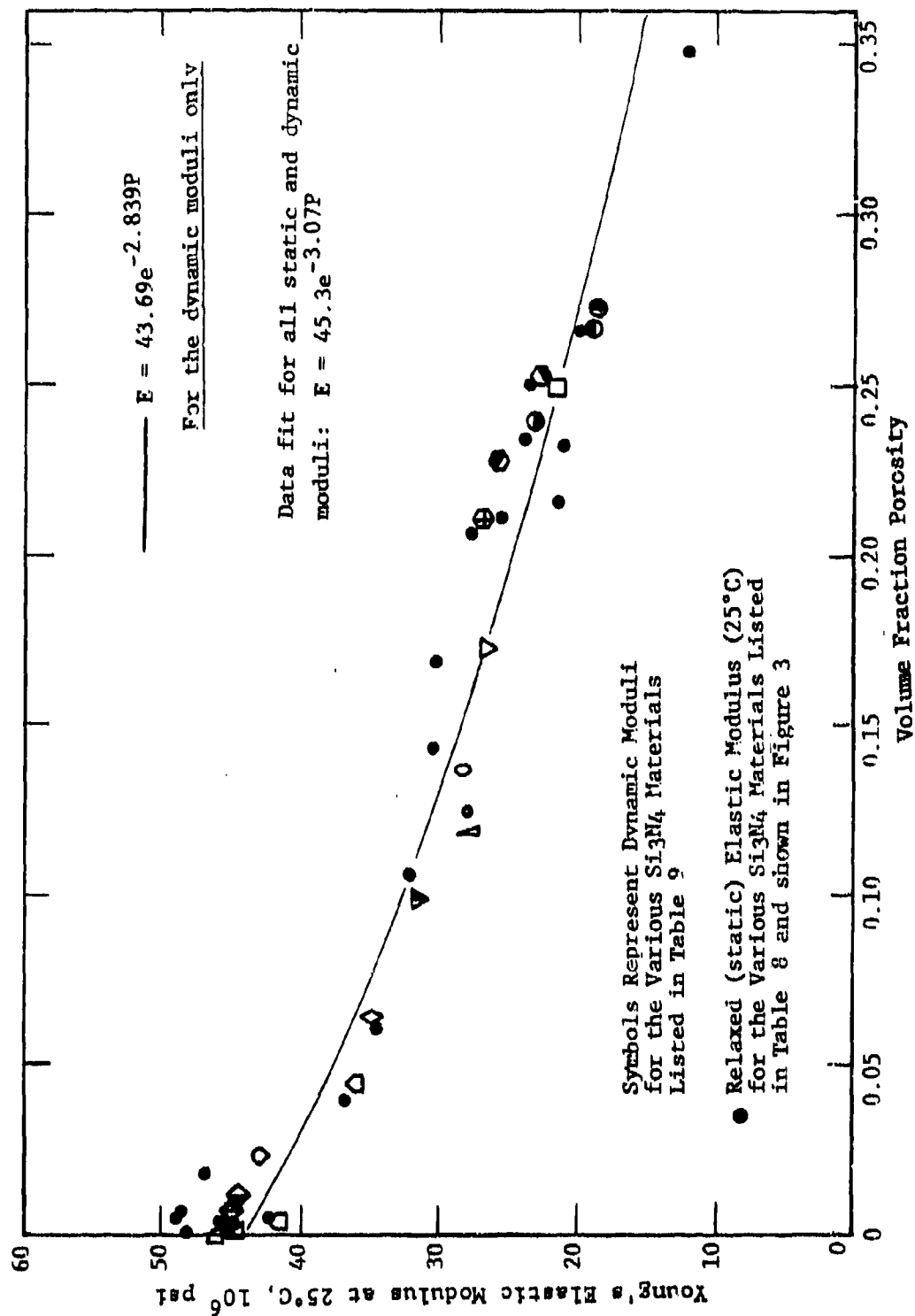
Figure 4. Comparison of Relaxed and Dynamic Elastic Moduli for Various Si_3N_4 Materials

E = 43.69e$^{-2.839P}$

For the dynamic moduli only

Data fit for all static and dynamic
moduli: E = 45.3e$^{-3.07P}$

Symbols Represent Dynamic Moduli
for the Various Si_3N_4 Materials
Listed in Table 9

● Relaxed (static) Elastic Modulus (25°C)
for the Various Si_3N_4 Materials Listed
in Table 8 and shown in Figure 3

Volume Fraction Porosity

Young's Elastic Modulus at 25°C, 10^6 psi

28

The data fit for all Si_3N_4 static and dynamic moduli has the exponential form

$$E = 45.3 \ e^{-3.07P} \qquad (2)$$

The room-temperature 4-point flexure strength of all SiC materials evaluated to date is compiled in Table 10. The static and dynamic moduli of the SiC materials is tabulated in Table 11 and plotted as a function of porosity in Fig. 5. Regression analysis of the current static and dynamic (combined) SiC data gives

$$E = 63.7 \ e^{-3.15P} \qquad (3)$$

5.3 Properties at Elevated Temperature

Throughout this program it is important to remember that comparisons are made between materials that span a wide range of processing maturity (i.e., commercially available to developmental/experimental) and intended use. This is especially important when considering high-temperature behavior where properties are directly related to the impurity phases present.

The strength-temperature dependence of various silicon-base non-oxide ceramics was determined by 4-point flexure testing in air at 25°C and (generally) 1000°, 1250°, and 1500°C. The machine crosshead speed was 0.02 ipm, and the sample size was usually 1/8 x 1/4 x 2-1/4-inch nominal dimensions (edges chamfered). Density, surface finish, machining history, and approximate date of manufacture were given in Table 2. The sample population for any given test condition was generally from five to ten. Tabular data for each sample tested are contained in the various semi-annual reports issued on this contract.

5.3.1 Hot-Pressed Si_3N_4

The strength vs. temperature behavior of seven hot-pressed Si_3N_4 materials is shown in Figs. 6 and 7. The strength of Norton NC-132 decreases rapidly above ~1200°C due to the presence

TABLE 10

SUMMARY OF ROOM-TEMPERATURE STRENGTH AND POROSITY DATA
FOR VARIOUS SiC MATERIALS

MATERIAL	BULK DENSITY (gm/cc)	THEORETICAL DENSITY[a]	VOLUME FRACTION POROSITY[b]	ROOM TEMPERATURE 4-POINT 3FND STRENGTH (ksi)
Norton NC-435 Siliconized SiC, Batch 1	2.936	3.0396	.0341	50.5
Norton NC-435 Siliconized SiC, Batch 3	2.997	3.0396	.0140	66.0
Norton NC-435 Siliconized SiC, Batch 4	2.962	3.0396	.0255	55.2
General Electric Sintered β-SiC	3.032	3.217	.0575	63.8
Carborundum Sintered α-SiC	3.159	3.217	.0180	44.2
UKAEA/BNF REFEL Si/SiC, Diamond Ground	3.101	3.1283	.0087	44.9
UKAEA/BNF REFEL Si/SiC, As-Processed	3.090	3.1283	.0122	33.6
Ceradyne Ceralloy 146A, HP-SiC + 2% Al_2O_3	3.224	3.2293	.0016	60.1
Ceradyne Ceralloy 146I, HP-SiC + 2% B_4C	3.211	3.1993	0	45.6

[a] Theoretical Density computed from nominal chemical composition assuming ρ_{SiC} = 3.217, ρ_{SI} = 2.33, ρ_{B_4C} = 2.52, $\rho_{Al_2O_3}$ = 3.97 gm/cc.

The effective theoretical density for NC-435 and Refel siliconized SiC was computed by the relation $\rho = v_1\rho_1 + v_2\rho_2$, assuming 20 vol% and 10 vol% silicon phase, respectively.

The effective theoretical density of all other materials was computed from their nominal chemical composition using the relation $\frac{1}{\rho} = \frac{x_1}{\rho_1} + \frac{x_2}{\rho_2}$, where x_1 and x_2 refer to the wt% of each phase present

[b] $P = 1 - \rho_{BULK}/\rho_{THED}$

30

TABLE 11

SUMMARY OF ROOM-TEMPERATURE RELAXED AND DYNAMIC ELASTIC MODULUS DATA FOR VARIOUS SiC MATERIALS

SYMBOL IN FIGURE 5		Material	Bulk Density[a] (Sonic) (gm/cc)	Theoretical Density[b]	Volume Fraction Porosity[b]	Young's Modulus (Sonic)[d] 10^6 psi	Static Youngs Modulus (With Corresponding Density)[c] 10^6 psi
Static Modulus	Dynamic Modulus						
●	○	Norton NC-435 Siliconized SiC, Batch 1	2.953	3.217	.0821	49.1	53.9 (2.936)
■	□	Norton NC-435 Siliconized SiC, Batch 3	2.973	3.217	.0758	49.6	49.5 (2.997)
◆	◇	Norton NC-435 Siliconized SiC, Batch 4	2.991	3.217	.0703	50.6	48.8 (2.962)
▲	△	General Electric Sintered β-SiC	3.031	3.217	.0578	54.6	54.8 (3.032)
▲	△	Carborundum Sintered α-SiC	3.159	3.217	.0180	62.1	58.2 (3.159)
◗	◖	UKAEA/BNF REFEL Si/SiC, Diamond Ground	3.086	3.217	.0407	56.2	57.5 (3.101)
◖	◗	UKAEA/BNF REFEL Si/SiC, As-Processed	3.049	3.217	.0522	49.1	52.5 (3.090)
●	◇	Ceradyne Ceralloy 146A, HP-SiC + 2% Al_2O_3	3.255	3.229	0	63.5	67.2 (3.224)
◀	◁	Ceradyne Ceralloy 146I, HP-SiC + 2% B_4C	3.229	3.217	0	62.6	65.3 (3.211)

a   Average values for dynamic modulus samples.

b   Theoretical density computed from nominal chemical composition only for Ceradyne 146A. All other materials: Theoretical density assumed to be $\rho TH = 3.217$ gm/cc.

c   Determined with strain gage transducers during 4-point flexure strength test (0.02 ipm crosshead deflection).

d   Dynamic elastic modulus determined by flexural resonant frequency method

31
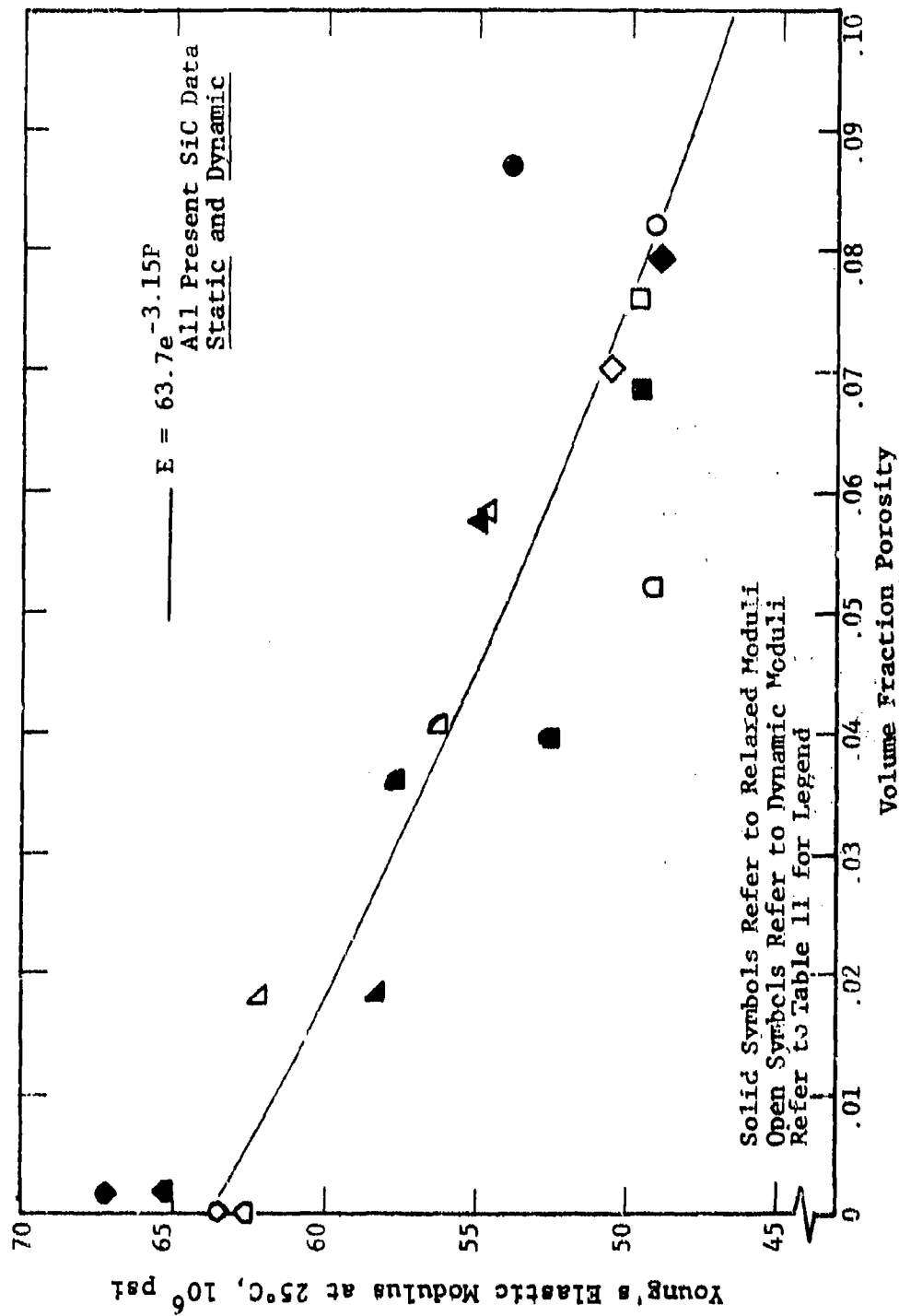
Figure 5. Comparison of Relaxed and Dynamic Elastic Moduli for Various SiC Materials

32
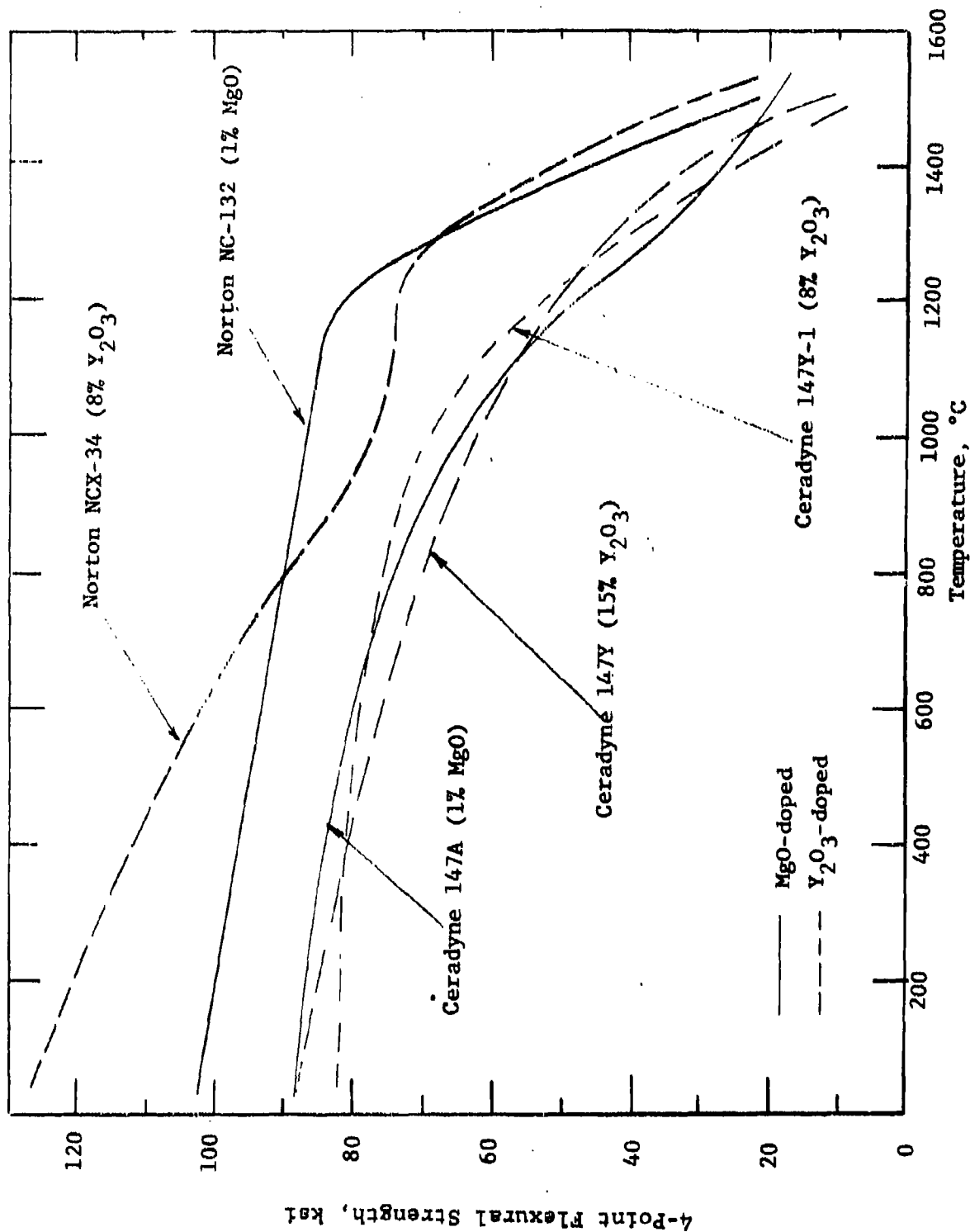
Figure 6. Flexural Strength of MgO- and Y_2O_3-Doped HP-Si_3N_4 Materials

33
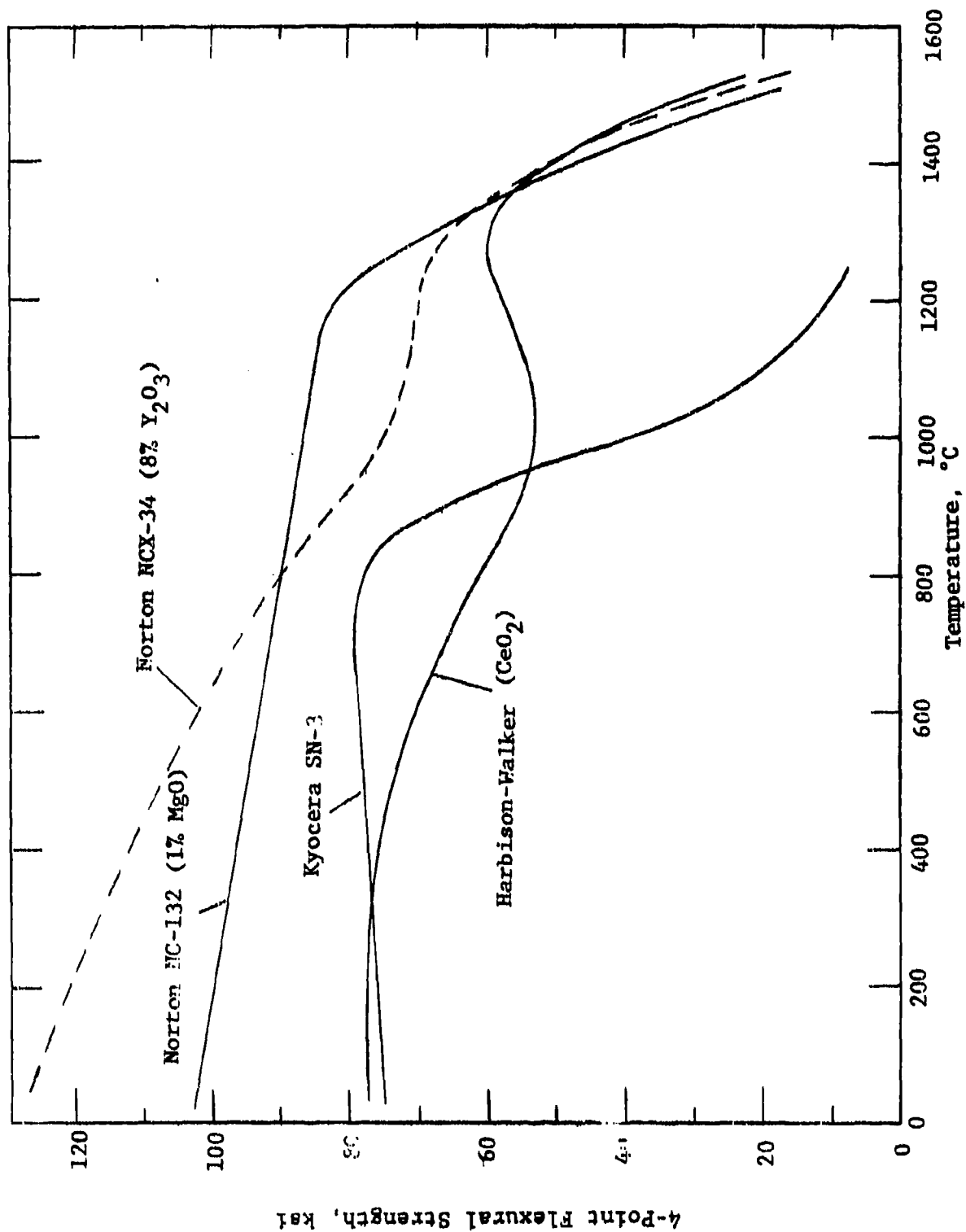
Figure 7. Flexural Strength of Hot-Pressed Silicon Nitride Materials

34

of a viscous grain boundary phase that results from the use of MgO as a densification aid. Evidence of subcritical crack growth was detected on the fracture surfaces at 1350°C and above. At 1500°C the slow crack growth (SCG) propagated through about 40% of the sample cross section. The presence of a thick glassy oxide coating obscured the details of the fracture features for NC-132.

Norton has developed NCX-34 with 8% Y_2O_3 additive in an attempt to form more refractory grain boundary phases than are present in NC-132, thereby extending the useful properties out to higher temperatures. Figure 6 illustrates that this was not accomplished with the particular batch of NCX-34 tested on this program. The strength of NCX-34 above 1200°C is virtually the same as for NC-132. No evidence of SCG was detected on the fracture surfaces at 1250°C. Slow crack growth was in evidence at 1500°C, extending over 20-50% of the test bar cross-section. However, no direct comparison can be made with NC-132 regarding the temperature where SCG is first detected on the fracture surface, since NCX-34 was not tested at 1350°C. At 1500°C the features of the fracture surfaces of NCX-34 indicate an intergranular fracture mode. The fracture features were not obscured by oxidation as they were for MgO-doped NC-132 tested at 1500°C. At first it was thought that the strength dip at 1000°C for NCX-34 might somehow be related to the presence of an oxidation-induced phase instability that has been observed in Y_2O_3-doped HP-Si_3N_4 at 1000°C (refer to Section VII). Subsequent fracture surface analysis (optical, as described above) indicated a larger predominance of inclusions identified as fracture origins in the samples tested at 1000°C compared to those samples fractured at 25°, 1250°, and 1500°C. Either these fracture-initiating inclusions in NCX-34 are re-lated to the intermediate temperature phase instability, or the particular sample population fractured at 1000°C simply contained larger pre-existing process-related critical flaws. SEM/EDX fracture surface analysis of these samples will be reported on Contract F33615-79-C-5100.

Figure 6 illustrates that the three hot-pressed Si_3N_4 materials from Ceradyne (doped with 1% MgO, 8% Y_2O_3, and 15% Y_2O_3) were of lower strength than the Norton NC-132 and NCX-34 materials. Slow crack growth was in evidence on the fracture surfaces of all three Ceradyne materials at $T \geq 1250°C$. The oxide layer obscured the features of the fracture surface of Ceradyne 147A (1% MgO) tested at 1500°C. However, the oxide layer was not smooth, continuous, and generally glassy as with Norton NC-132 (1% MgO), but rather consisted of many distinct, rough, crystalline, approximately hemispherical scale deposits. These differences were especially evident on the flat tensile or compressive surfaces of the bend bars. It is not known at present whether this is due to different scale composition, a different oxidation mechanism, or simply a rate effect. It does point out, however, the strong influence of impurities on oxidation. Refer to Section VII for details on the subject of oxidation effects. The Y_2O_3-doped HPSN materials from Ceradyne showed evidence of a second phase or non-uniform microstructure. Results of optical microstructural studies on polished and etched sections will be reported on Contract F33615-79-C-5100. The tensile and compressive surfaces of the 15% Y_2O_3-doped material tested at 1000°C showed definite evidence of the oxidation-induced phase instability discussed in Section VII. It is interesting to note in Fig. 6 that even though there was evidence of this instability, which will be shown to cause spontaneous fracture in samples with no external applied stress (in Section VII) that the 15% Y_2O_3-doped material has essentially the same strength-temperature behavior as Ceradyne's 1% MgO-doped HP-Si_3N_4. This would mean that perhaps the other pre-existing processing defects override the apparent instability effect. In general, the Ceradyne materials are not as processing-mature as the Norton HP-Si_3N_4 materials.

Figure 7 illustrates the strength vs. temperature of two additional HP-Si_3N_4 materials. Harbison-Walker is developing a 10% CeO_2-doped material. It is believed that ceria will form more refractory grain boundary phases with Si_3N_4, leading

36

to improved high temperature properties. As shown in Fig. 7 the strength of this developmental material is lower than for NC-132, there is a strength minimum at 1000°C, and the strength above 1300°C is the same as NC-132. There is visual evidence of microstructural non-uniformity and perhaps a second phase in this material. In many ways under the 60X optical microscope it resembles the Ceradyne Y_2O_3-doped materials. This means, perhaps, that ceria also forms unstable phases with Si_3N_4. The microstructural analysis and SEM/EDX surface and fracture surface studies to be reported on Contract F33615-79-C-5100 will investigate this further. At 1500°C the 10% CeO_2-doped material is severely oxidized to the extent that 1500°C is well beyond its maximum use temperature.

The Kyocera SN-3 HP-Si_3N_4 has a room temperature strength of ~80 ksi, which is maintained to about 800°C, after which it rapidly decreases. Degradation of strength at such a low temperature indicates the use of a larger amount of oxide densification aid than, for example, in NC-132, or an oxide additive containing more detrimental impurities, e.g., calcium. Indeed, the spectrographic impurity analysis shown in Table 7 indicates Kyocera SN-3 HPSN to contain comparatively large amounts of Al, Fe, Ca, and Mg. Evidence of subcritical crack growth was observed at 1000°C, and at 1250°C the SCG had progressed across the entire test sample cross section.

The elastic moduli of these HP-Si_3N_4 materials exhibit similar trends with respect to the second phases present. The stress-strain behavior for such materials is linear until the temperature corresponding to the rapid strength decrease, and progressively non-linear as the temperature is increased further. This is illustrated in Fig. 8. Since the behavior of these hot-pressed materials are controlled by the viscoelastic nature of the grain boundary phase and corresponding time dependent slow crack growth, strong strain rate dependence of these properties also exists.

37
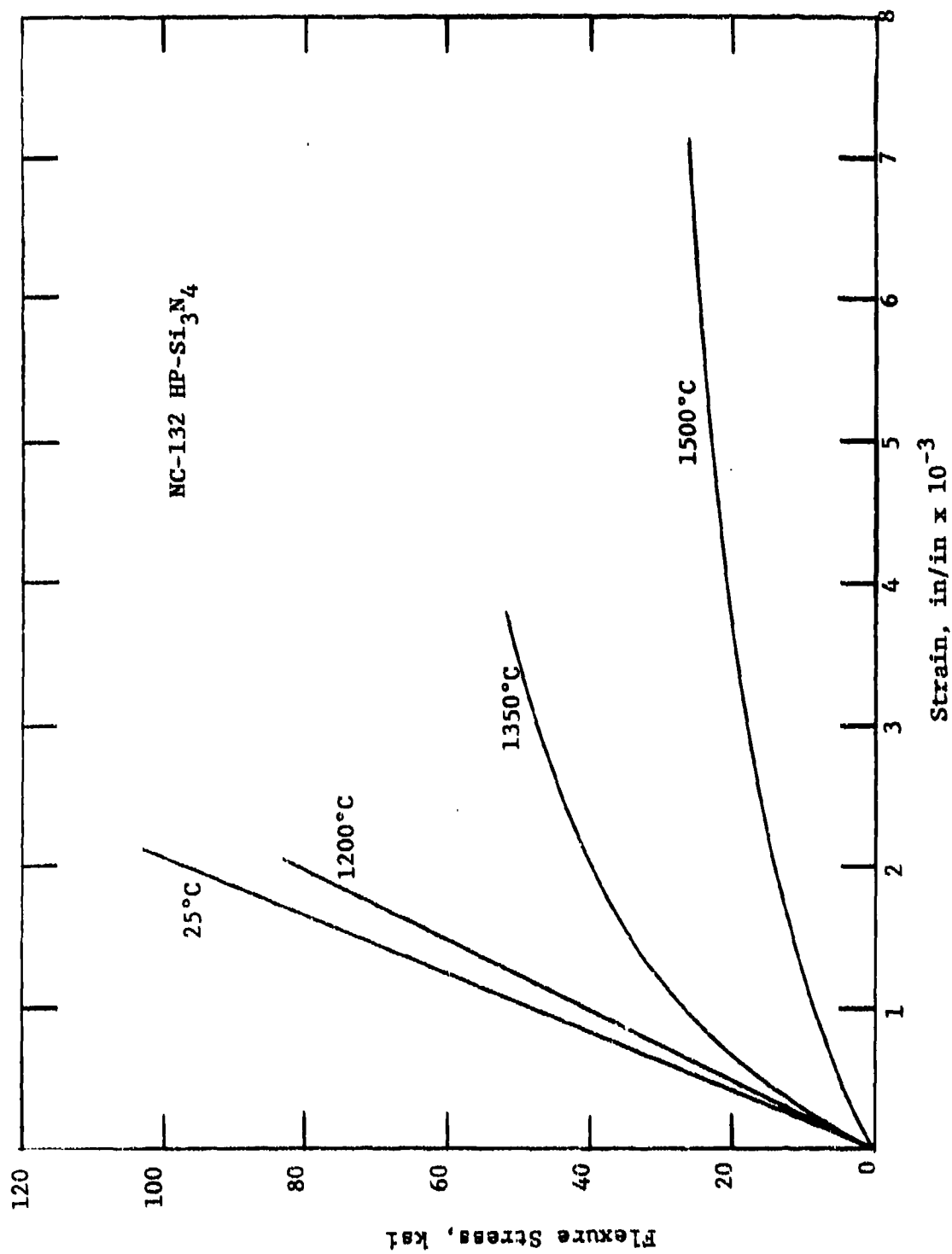
Figure 8. Representative Flexural Stress-Strain Behavior of NC-132, HP-Si$_3$N$_4$

5.3.2 Reaction-Sintered Si_3N_4

Figure 9 illustrates the strength-temperature behavior of various RS-Si_3N_4 materials. Some versions are doped with iron to enhance sintering. At elevated temperatures the lower temperature properties are generally maintained due to the high purity of these materials (especially with respect to the lack of oxide phases). The strength-controlling flaws are generally pores and pore agglomerates in RS-Si_3N_4. However, iron-rich inclusions are also common. Most RSSNs show significant strength increases with temperature, but some are relatively temperature-invariant. A strength peak at ~1200°C has often been observed. This is generally thought to be the result of oxidation-induced porosity modification, crack-tip blunting, etc. When no strength increase is observed at high temperature, it is generally believed that surface pores are sealed off preventing internal oxidation, or that the critical-size pores are too large to be appreciably affected by oxidation.

No evidence of subcritical crack growth was observed on any of the RS-Si_3N_4 fracture surfaces at test temperatures including 1500°C. Linear stress-strain behavior was observed at all test temperatures, as shown in Fig. 10. One exception to this was the RSSN from Indussa/Nippon Denko, which exhibited distinctly non-linear stress-strain at 1500°C. Norton NC-350 has flexure strength of almost 50 ksi at 1500°C. At 1500°C this is the strongest and most oxidation-resistant silicon nitride material investigated on this program. This is attributed to its high purity and uniform fine grain micro-structure. The results of spectrographic analysis shown in Table 7 confirm that NC-350 is the highest purity RSSN evaluated.

The reaction sintered materials from Ford (injection molded) and AiResearch (slip cast and injection molded) are also quite good materials, exhibiting a 1500°C fracture strength of ~40 ksi. Note the strength peak at ~1250°C for the Ford and AiResearch materials (Fig. 9). Testing was conducted at 1000°, 1250°, and 1500°C for these materials. No such peak
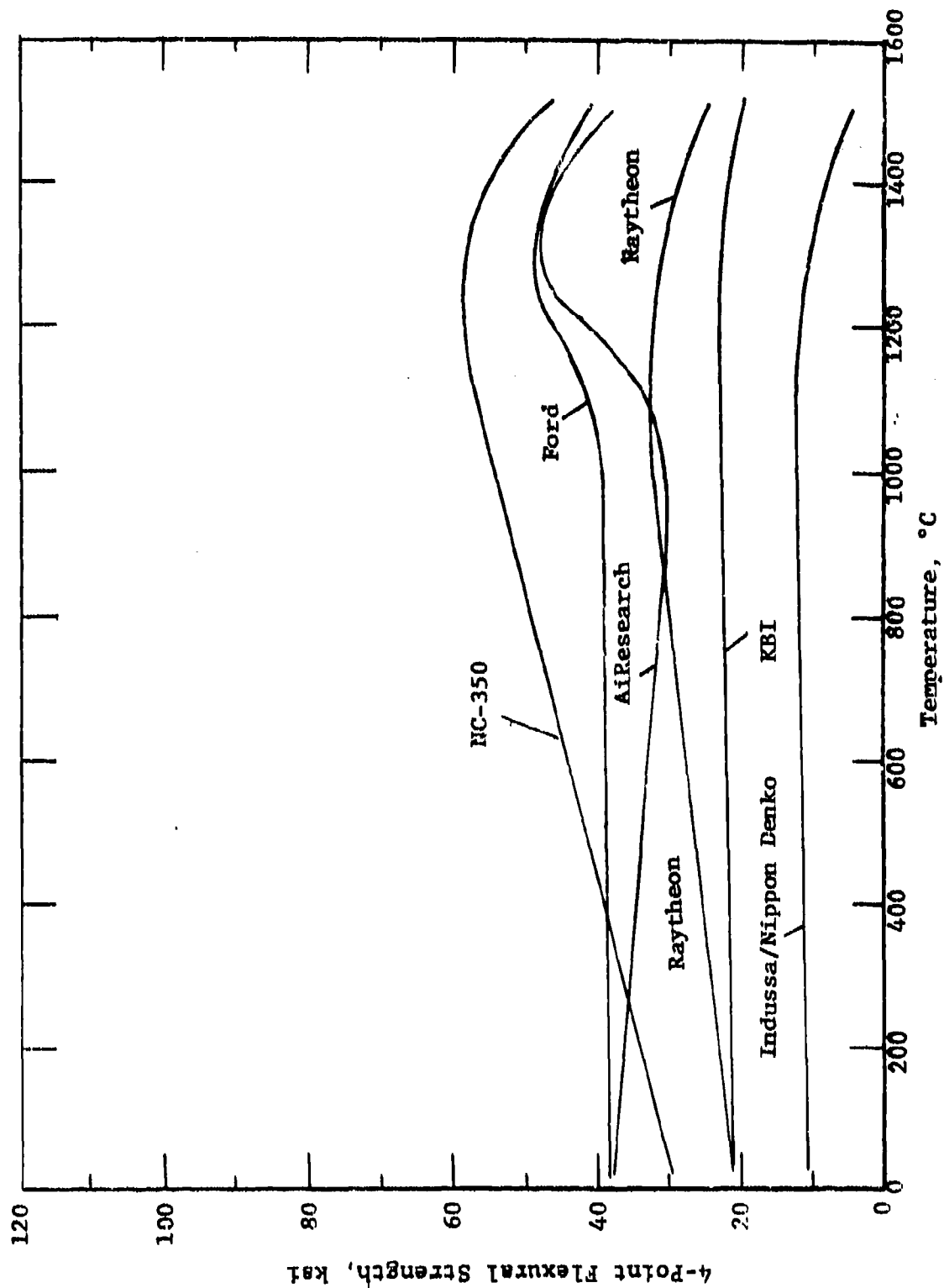
Figure 9. Flexural Strength of Reaction Sintered Si_3N_4 Materials
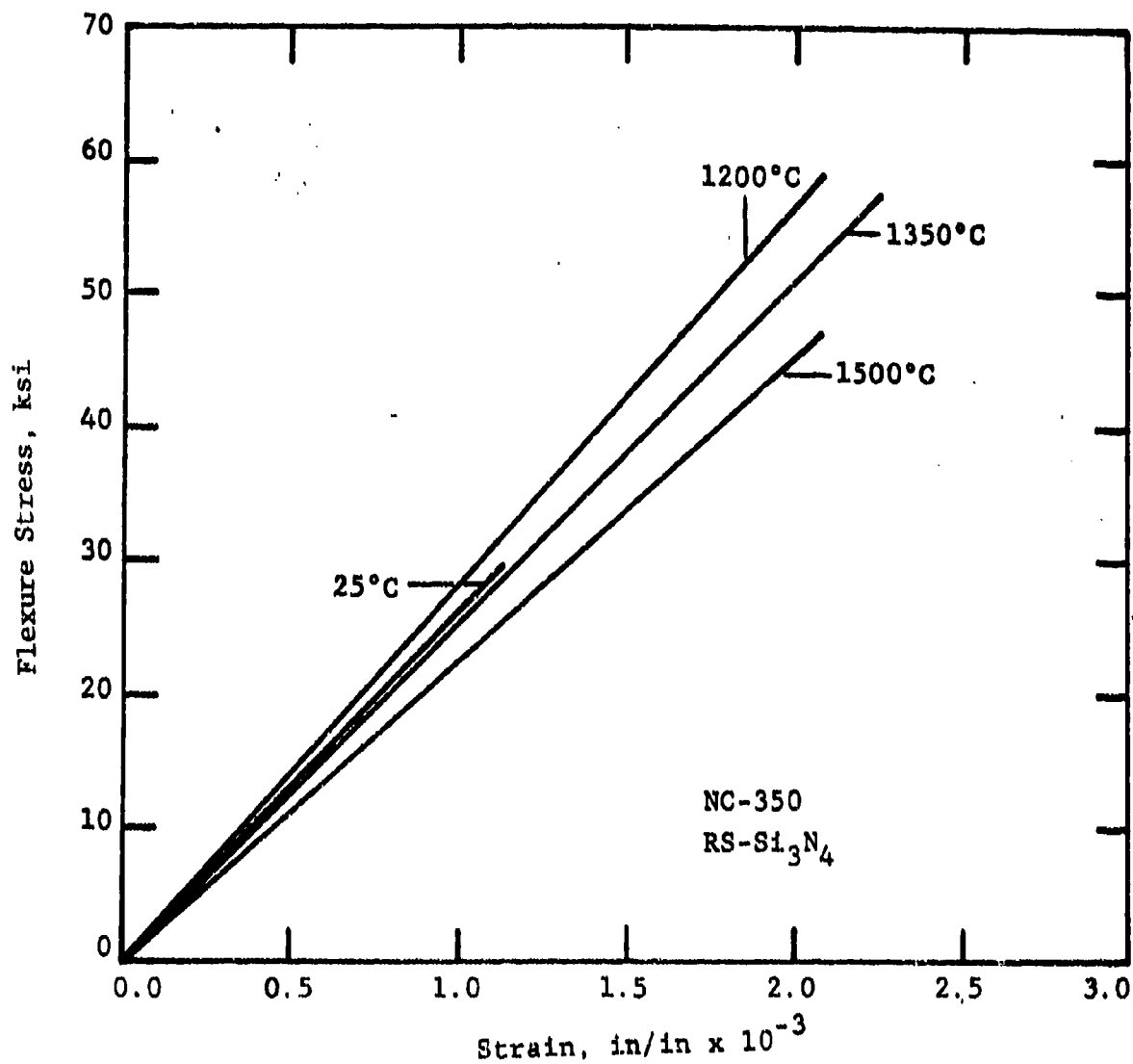
Figure 10. Representative Flexural Stress-Strain Behavior of NC-350, Reaction Sintered Si_3N_4

41

in strength is shown for NC-350. It should not be inferred that such a peak does not exist for NC-350, however, since current tests on NC-350 were not conducted below 1200°C. The Ford and AiResearch materials exhibited fairly good surface stability under the 1500°C/~15 min. exposure time of the flexure test. AiResearch injection molded material (RBN-122) appeared to have more inclusions than the slip-cast material (RBN-101). Ford (IM) RS-Si_3N_4 flexure tested at 1500°C exhibited rust-colored inclusions, presumably iron-oxide. The spectrographic analysis presented in Table 7 shows that the Ford and AiResearch materials contained about two to three times as much iron impurity as did Norton NC-350 (i.e., ~1% Fe vs. 0.4% Fe for NC-350).

The isopressed RSSN from Raytheon was of comparatively low strength (σ ~25 ksi at 1500°C). Samples tested at 1500°C exhibited a thick glassy oxide scale, with pitting at inclusion locations. The lower oxidation resistance observed for the Raytheon material is consistent with its higher impurity content with respect to the other materials. Table 7 illustrates that the Raytheon material has substantial Al impurity (~1%) as well as high Fe content (1.3%). This level of aluminum (perhaps aluminum oxide) contamination is significantly higher than in the other materials. This material was originally developed for radome applications. Therefore, long-time oxidation resistance was not of major concern when this material was developed. Such is not the case in the development of potential gas turbine ceramics.

The KBI RS-Si_3N_4 exhibited low and relatively constant strength from 25°C to 1500°C. Presumably the frequent ~50 μm pore agglomerates observed in this material are too large to be affected by oxidation. As mentioned above, this material was not well sintered and contained much unreacted silicon material. This phase would occasionally exude from the sample surfaces upon exposure at 1500°C (which is consistent with the 1410°C melting point of silicon). However, the KBI material generally exhibited good oxidation resistance and surface stability. The

spectrographic impurity analysis results shown in Table 7 illustrate that this can be attributed to the high purity of KBI RS-Si_3N_4. Impurity levels are similar to those for Norton NC-350 RS-Si_3N_4, which exhibited excellent resistance to oxidation attack.

The Indussa/Nippon Denko RS-Si_3N_4 had a flexure strength of only ~10 ksi from 25° to 1500°C. Fracture features were diffuse and nondescript. Very large pores and pore agglomerates are readily observed with the unaided eye (density = 2.1 gm/cc). Two types of large inclusions, one rust-colored and the other dark, were also very evident. Spectrographic impurity analysis indicated relatively low iron impurity (similar to NC-350 and KBI RSSNs), but high Al and Ca impurities.

5.3.3 Sintered Si_3N_4

Conventionally sintered Si_3N_4 materials from Kyocera and GTE Labs. were evaluated. The strength-temperature behavior is illustrated in Fig. 11, with a representative curve for NC-350 reaction-sintered Si_3N_4 shown for comparison. The room temperature strength of the pressureless sintered materials is higher than for reaction-sintered Si_3N_4 due to their higher density resulting from the use of oxide sintering aids. However, the disadvantage of the use of oxide sintering aids is seen at high temperatures where the strength degrades due to the existence of oxide grain-boundary phases. Conversely, the extremely pure reaction-sintered material is often substantially stronger at elevated temperature than it is at room temperature, and is stronger than sintered Si_3N_4 at the highest test temperatures. However, sintered Si_3N_4 materials are a relatively recent development, and much promise is held for them.

As shown in Fig. 11, the sintered Si_3N_4 (SSN) materials from Kyocera exhibit strength that falls off at low temperature, about 800°C, similar to the Kyocera hot-pressed material discussed above. The two Kyocera SSNs are apparently sintered with Al_2O_3 and MgO, since spectrographic impurity analysis (Fig. 7) indicates

43
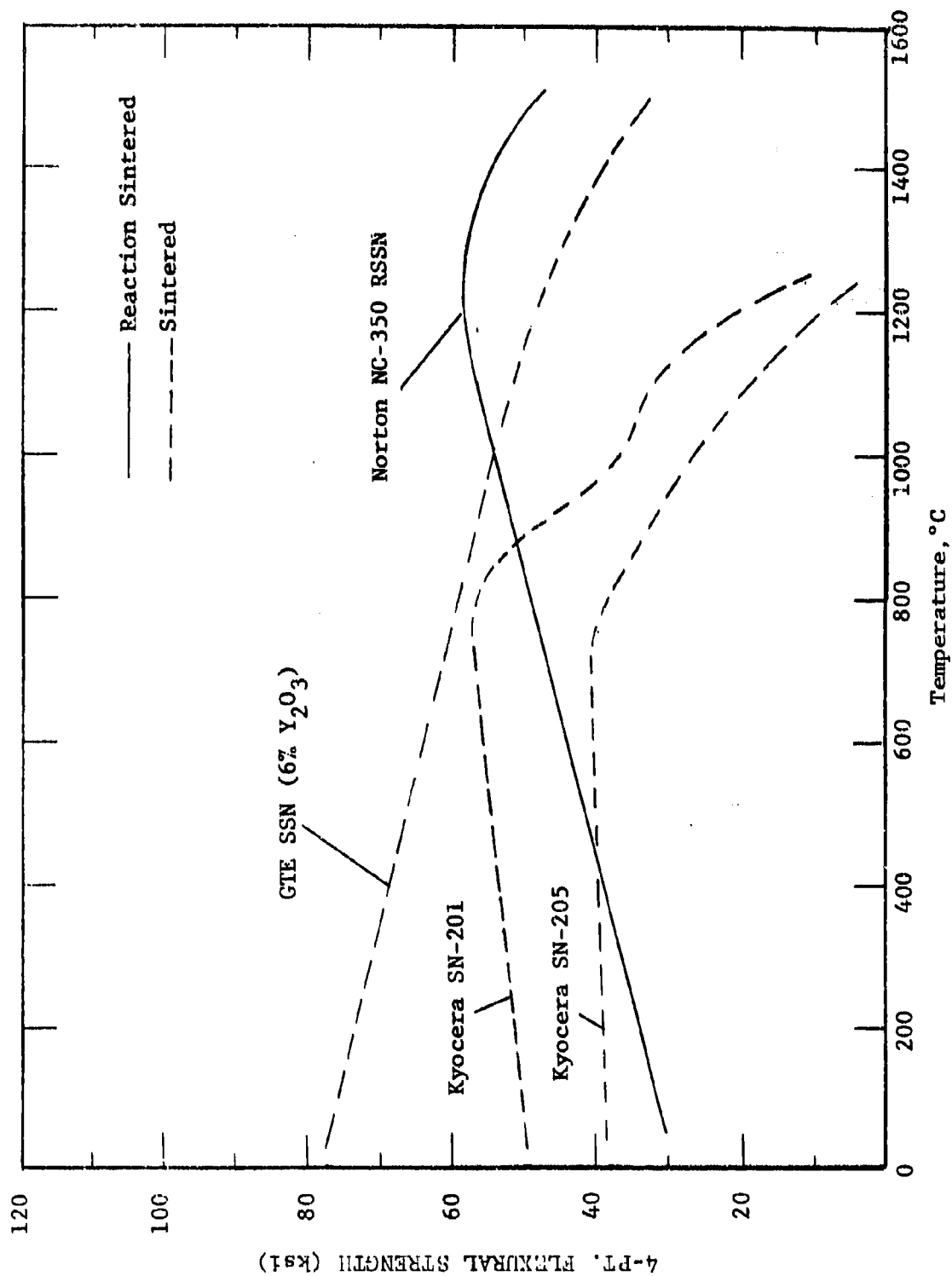
Figure 11. Flexural Strength of Reaction-Sintered and Sintered Silicon Nitride Materials

44

aluminum, iron, calcium, and magnesium impurities that total ~10%.

The GTE sintered Si_3N_4 is a very promising material that has been reported to have excellent high temperature properties.[2] It is sintered with 6% Y_2O_3 additive, for the same reason that Y_2O_3 is being considered as an additive for HP-Si_3N_4 (i.e., Y_2O_3 may result in more refractory impurity phases located in grain boundary regions than does MgO). Figure 11 illustrates that the Y_2O_3-doped GTE material has respectable room temperature strength for a developmental material (80 ksi), and its elevated temperature strength does not decrease as abruptly as is often observed in HP-Si_3N_4. Fig. 12 illustrates that the elastic modulus of GTE SSN is closer to that for HPSN than for RSSN. This is due to the near theoretical density of the GTE material. Perhaps the best indication of the potential of Y_2O_3-doped SSN is seen in its elastic modulus at elevated temperature. As shown in Fig. 12, the modulus of GTE SSN is maintained out to ~1350°C before it begins to decrease. This is apparently the result of the use of Y_2O_3. Figure 12 implies that the effective use temperature of Y_2O_3-doped SSN is ~150°C higher than for MgO-doped hot-pressed material. This is the first indication seen on this program of the potential advantage of using Y_2O_3 as a processing additive to improve elevated temperature properties (over MgO additives). As discussed in Sections VII and IX, Norton NCX-34 HP-Si_3N_4 (8% Y_2O_3) has exhibited superior creep and oxidation resistance compared to MgO-doped NC-132, which gives further indication of the advantage of Y_2O_3 additives.

5.3.4 SiC Materials

Three forms of SiC materials were evaluated: hot pressed, siliconized, and sintered. The strength-temperature behavior of these materials obtained on this program is shown in Fig. 13. Fracture surface analysis indicating failure origins and general fracture surface appearance will be reported on Contract F33615-79-C-5100. In this report the general strength-temperature behavior is discussed.
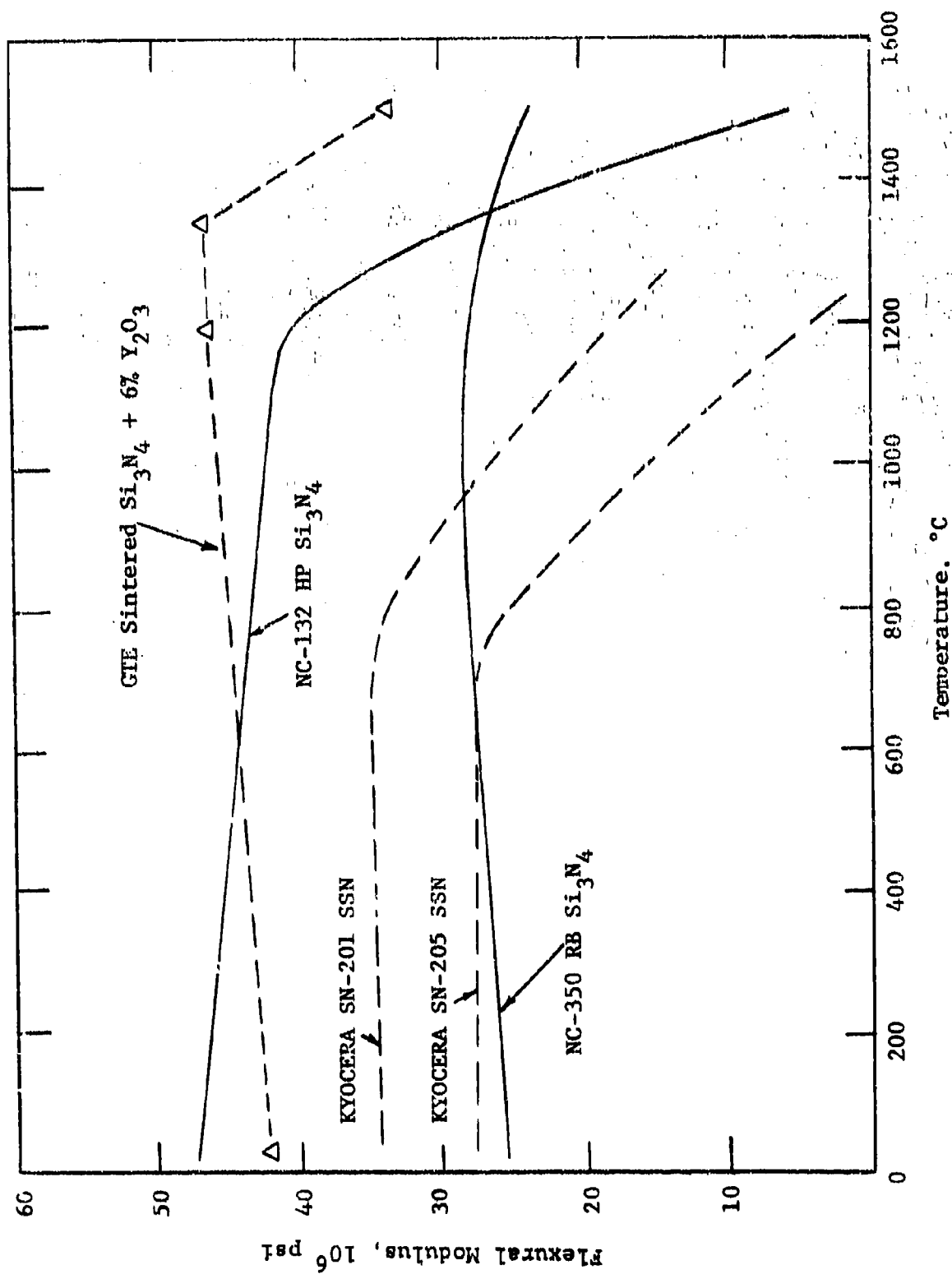
Figure 12. Flexural Elastic (Secant) Modulus of Various Si_3N_4 Materials
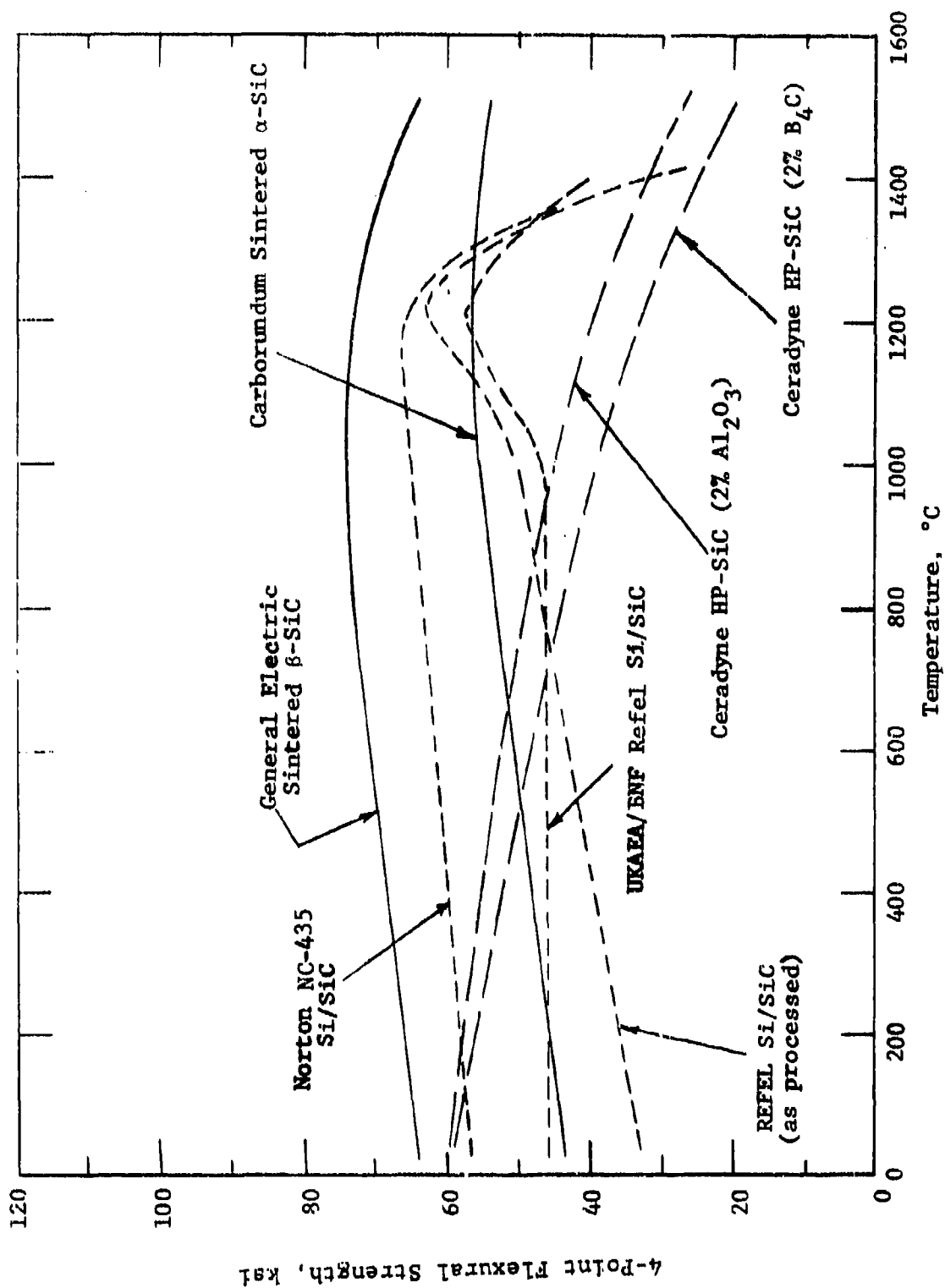
Figure 13. Flexural Strength of Silicon Carbide Materials

47

Silicon carbide materials have room temperature strength intermediate to reaction-sintered Si_3N_4 and hot-pressed Si_3N_4. The two hot-pressed SiC materials from Ceradyne exhibit more pronounced strength reduction at elevated temperature than do the sintered SiC materials. Sintered SiC from Carborundum (α-SiC) and General Electric (β-SiC) maintain strength out to 1500°C due to the lack of significant oxide grain boundary phases. They exhibit linear stress-strain behavior at 1500°C as shown in Fig. 14. In hot-pressed SiC using Al_2O_3 as a densification aid, the grain boundary phases that are responsible for the strength reduction and non-linear stress-strain behavior at 1500°C (Figs. 13 and 15) are presumably alumina-rich (perhaps an aluminosilicate phase). It is not known what the composition of the grain boundary phase would be for the HP-SiC with B_4C additive, but non-linear stress-strain behavior was also observed at elevated temperature. Rubin[3] indicates that the strength of B_4C-doped HP-SiC would be expected to be lower than the Al_2O_3-doped material, due to larger grain size. Alumina additions inhibit grain growth in SiC, whereas B_4C promotes grain growth during hot-pressing.

Siliconized forms of SiC contain ~5-20% free silicon, infiltrated into the originally porous SiC structure to densify the body. Their strength is shown in Fig. 13 to peak at ~1200°C, and then decrease rapidly, as the melting point of silicon is approached (1410°C). The stress-strain curve for Norton NC-435 (Fig. 16) illustrates non-linear behavior at T≥1200°C.

All forms of SiC have high elastic modulus. This is shown for the two Ceradyne hot-pressed materials in Fig. 17.
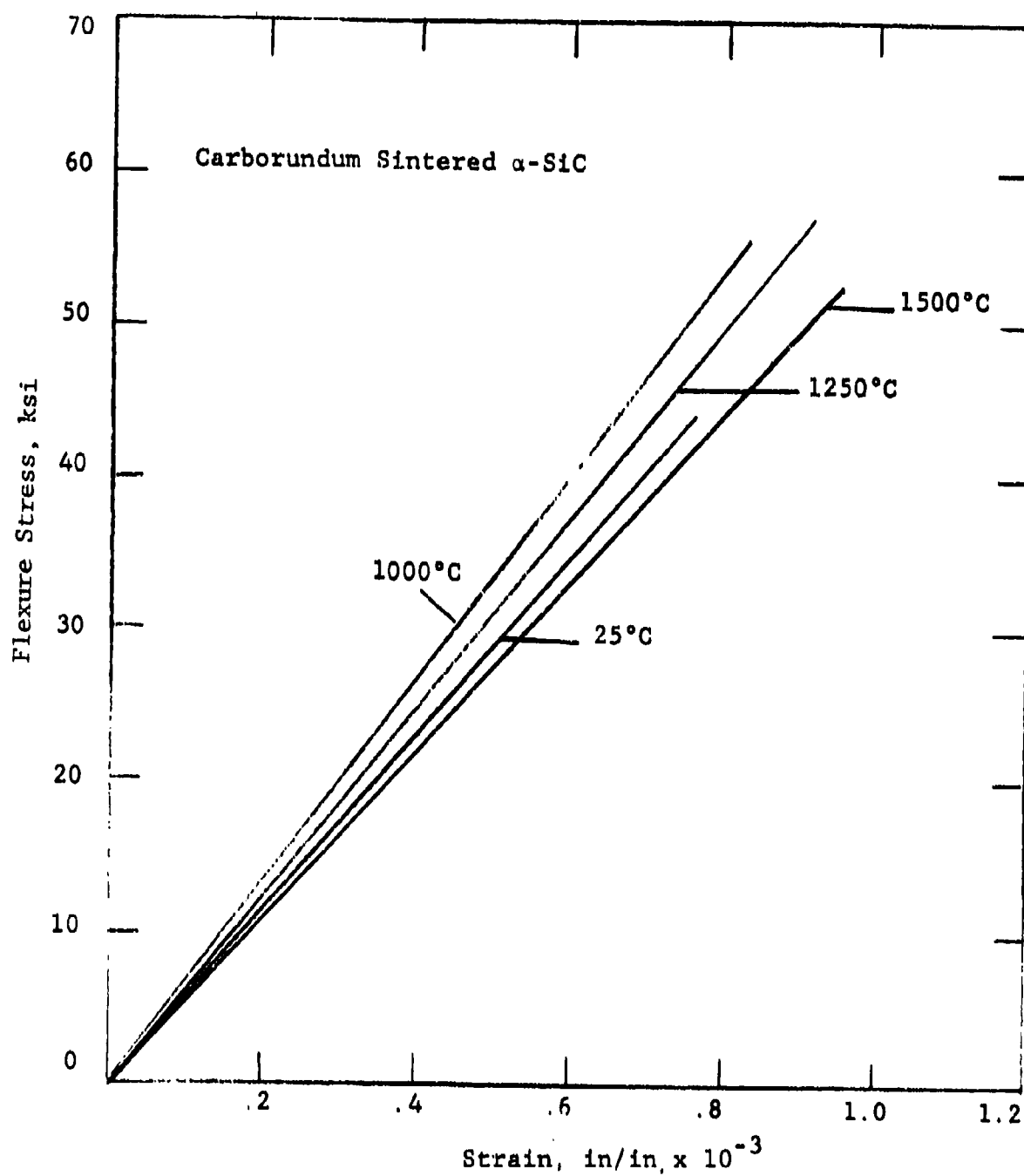
Figure 14. Representative Flexural Stress-Strain Behavior of Carborundum Sintered α-SiC Material
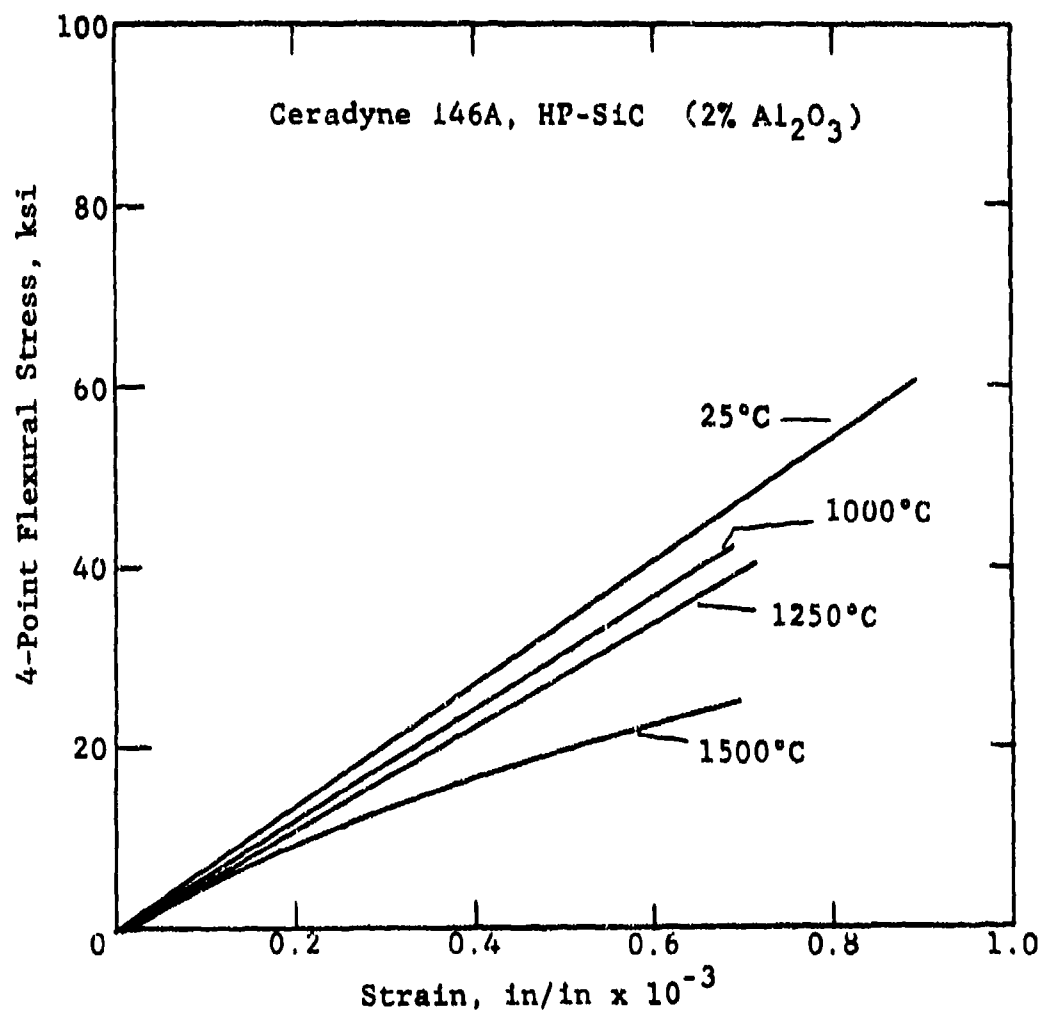
Figure 15.   Flexural Stress-Strain Behavior of
Ceradyne 146A, HP-SiC (2% Al_2O_3)

50
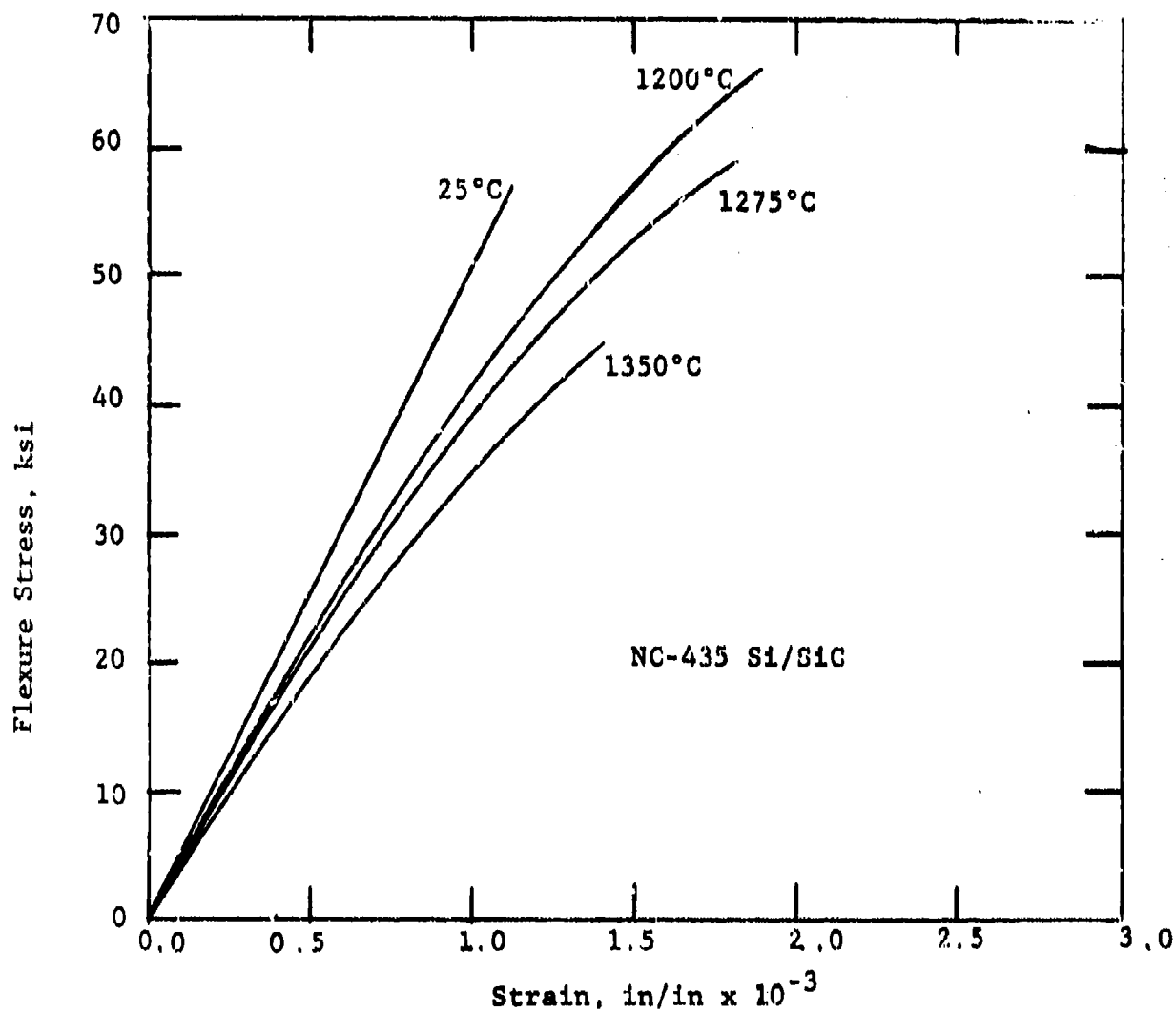
Figure 16. Representative Flexural Stress-Strain Behavior
of NC-435, Si/SiC
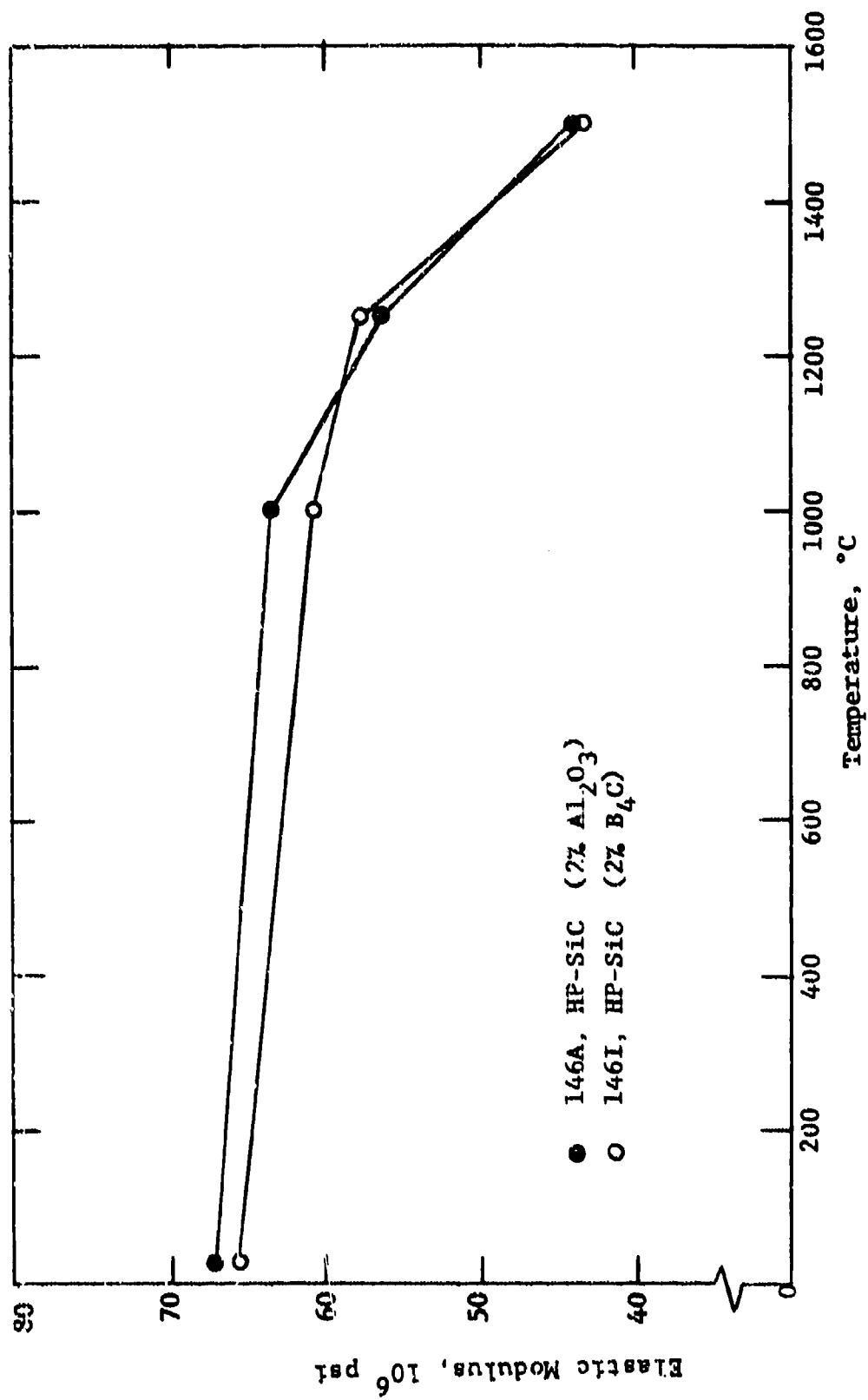
Figure 17. Elastic Modulus of HP-SiC Materials

● 146A, HP-SiC (2% Al_2O_3)

O 146I, HP-SiC (2% B_4C)

Temperature, °C

Elastic Modulus, 10^6 psi

STRENGTH DEGRADATION BY SUBCRITICAL CRACK GROWTH

Silicon-base ceramics exhibit time-dependent strength at elevated temperatures. This is an especially important design consideration for long-time applications. A primary cause of this strength degradation is subcritical crack growth (SCG).[*] For the condition of subcritical crack growth, pre-existing flaws grow under the applied stress, so that the critical stress intensity at the crack tip is reached (thus leading to rapid fracture) at a lower macroscopic stress level than if the cracks were stable and unable to grow. The exact mechanism of SCG is relatively unknown at present, but is related to material microstructure. For example, in hot-pressed Si_3N_4 doped with MgO, significant glassy grain-boundary phases exist. This intergranular phase deforms quite readily at elevated temperature, leading to grain-boundary sliding. This promotes slow crack growth leading to lowered strength. The pre-existing flaws in $HP-Si_3N_4$ are often thought to be voids existing at intergranular triple points. Their extension is the mechanism to accommodate the grain-boundary sliding. In the extremely pure sintered SiC materials, rates of SCG are much lower. In such materials current speculation is that slow crack growth is an atomistic-level process occurring at the crack tip, e.g., stress corrosion by an oxidation mechanism. Subcritical crack growth or static fatigue is very sensitive to environment. For instance, Srinivasan et al.[4] report no detectable SCG in sintered α-SiC tested in argon at 1500°C. However, in air at 1500°C there was evidence of significant SCG, the mechanism being atmospheric attack of intergranular regions leading to grain separation. McHenry and Tressler[5] also indicate the mechanism of SCG in NC-203 HP-SiC to be stress-corrosion by oxidation.

---

[*]Corrosion, erosion, and oxidation effects can also lead to strength degradation at long times in agressive environments. This subject is treated in Section VII of this report.

Subcritical crack growth is described by the relation $v = AK^n$, where v is the crack velocity, A is a material constant, and K is the stress intensity at the crack tip. The extent of SCG and thus strength degradation is characterized by the exponent n in this relation. Large n indicates very little SCG and time-invariant strength. Many techniques are used to obtain crack growth data at high crack velocities (i.e., short times): e.g., double torsion load relaxation, direct observation of crack growth, etc. However, indirect methods are thought to be more accurate for low crack velocities (i.e., at long times). The use of two such indirect methods, differential strain rate flexure tests and flexural stress rupture tests, is discussed below.

Trantina, Johnson, and Prochazka[6,7] have shown that the $v = AK^n$ relation can be integrated over the total time-to-failure for the condition of constant stress to give

$$\sigma^n \tau = k \tag{4}$$

where σ is the applied stress, τ is the time to failure, and k is a constant, being a function of the critical stress intensity factor (KI_c) and the fast fracture strength (σ_o). In a similar manner, $v = AK^n$ can be integrated over the total time-to-failure under constant stress rate conditions to give

$$\sigma^n \tau = k(n+1) \tag{5}$$

These two strength vs. time-to-failure relations are illustrated schematically in Fig. 18. The strength-time curves for both conditions have the same slope (-1/n) and are separated on the time scale by a factor log(n+1). The n is the factor that characterizes the extent of slow crack growth (the pre-exponential factor A in the relation $v = AK^n$ does also). A material with very little SCG will have a high n value, and a relatively time-invariant stress. The constant stress rate curve shown in Fig. 18 can be readily generated by conducting a series of flexure strength tests at various machine crosshead speeds.
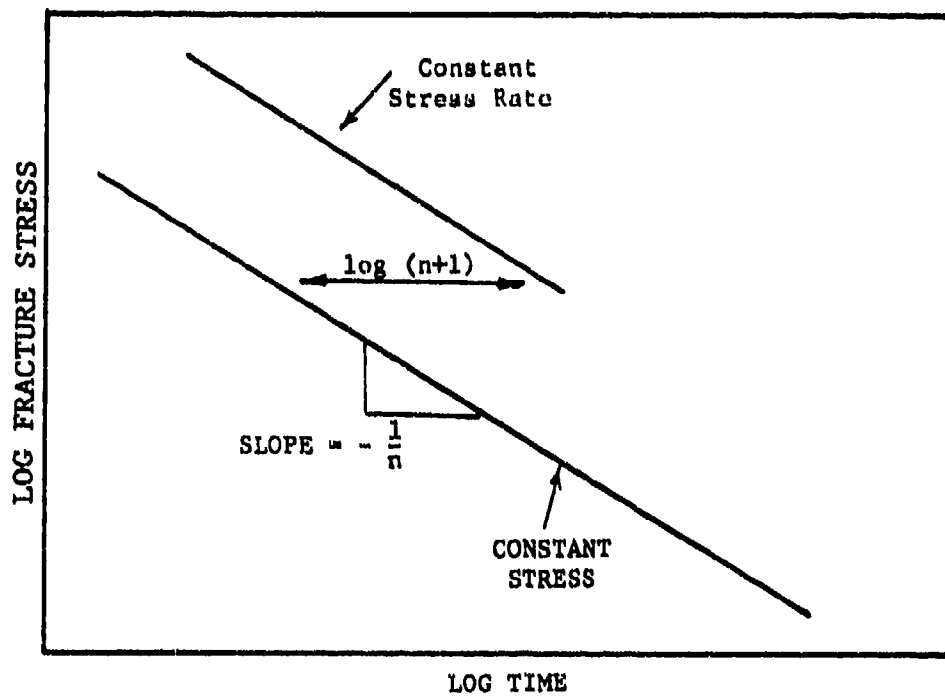
Figure 18.   Constant Stress and Constant Stress Rate Data
            Used to Predict Long-Time Strength Degradation
            Due to Subcritical Crack Growth

Speeds in these tests are chosen such that the strength relation will span times-to-failure from seconds to a few hours. These tests are often referred to as differential strain rate tests. The constant stress curve shown in Fig. 18 can be obtained from long-time stress rupture tests. Thus, the use of the relatively short-term differential strain rate tests permits prediction of strength degradation due to slow crack growth at much lower stresses and much longer times. Such techniques will aid greatly in life prediction. The differential strain rate tests provide a convenient way of generating screening data regarding the extent of SCG in the wide variety of Si_3N_4 and SiC materials of interest in this program.

Strength vs. time-to-failure data were obtained for General Electric sintered SiC and Norton NC-203 HP-SiC (2% Al_2O_3).* In addition, data were obtained on a few samples of three other materials of current interest: Norton NC-132 HP-Si_3N_4 (1% MgO), NCX-34 HP-Si_3N_4 (8% Y_2O_3), and NC-350 RS-Si_3N_4.

The constant stress rate (differential strain rate) data obtained at 1500°C in air atmosphere on GE sintered SiC and Norton NC-203 HP-SiC are plotted in Fig. 19. Strain rates (testing machine crosshead speeds) were adjusted to give times-to-failure out to about 3 hours. Both SiC materials exhibited strength degradation with time. Linear least-squares regression analyses resulted in the GE sintered SiC being described by the exponent n = 29, and the NC-203 HP-SiC being described by n = 22.5. The greater strength degradation in the hot-pressed material is caused by greater subcritical crack growth, which is probably related to the existence of aluminosilicate intergranular phases. McHenry and Tressler[5] indicate the mechanism of SCG in NC-203 to be stress corrosion by oxidation.
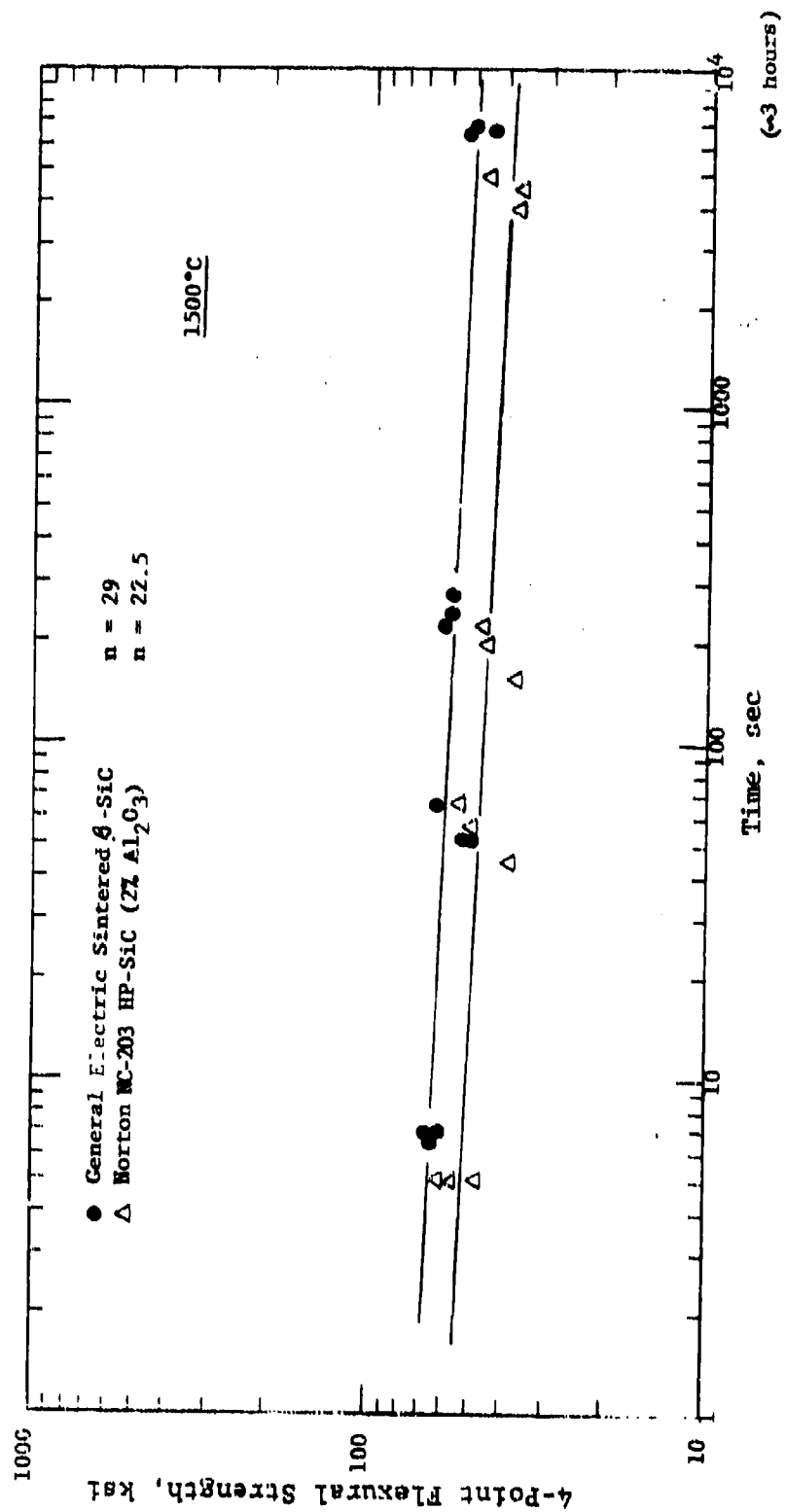
Figure 19.   Differential Strain Rate Strength Test Results (Constant Stress Rate Tests)

Figure 20 presents current strength degradation data
on the two SiC materials and the three Si_3N_4 materials as
compared to literature data. All current data were obtained
in 4-point flexure. The exponent n value of 29 for the sintered
SiC and 22.5 for the hot-pressed SiC obtained in this work are
the same as found in the literature[7,8] for these two SiC
materials. However, Trantina and Johnson[9] did not find
substantial SCG in sintered β-SiC until the temperature was
raised to 1600°C, based on 3-point bend differential strain
rate tests. Current data on sintered SiC indicate the same
degree of SCG at 1500°C (i.e., same n), based on 4-point
differential strain rate tests.

The double-torsion data of Evans and Wiederhorn[10]
included in Fig. 20 extend to long times and indicate the
comparatively larger predominance of SCG at elevated
temperature for hot-pressed Si_3N_4 than for either form of SiC.
This is presumably related to a much more compliant grain
boundary phase. Note that not only is the exponent much lower
for HP-Si_3N_4, but that the tests were conducted at a much
lower temperature.

Current data for NC-350 RS-Si_3N_4 at 1500°C, and NC-132
(1% MgO) and NCX-34 (8% Y_2O_3) HP-Si_3N_4 at 1400°C are shown in
Fig. 20 by curve numbers 2, 4, and 5, respectively. The n
values obtained for NC-132 and NCX-34 (i.e., n = 16 and n = 12)
are in qualitative agreement with the results of Evans and
Wiederhorn on HS-130, which is the predecessor of NC-132.
Current data are consistent with the flexure strength data
presented in Section V, where it was shown that the presently
tested batch of NCX-34 (Y_2O_3) did not exhibit the desired
improvement in high temperature properties over NC-132 (MgO).

The data for NC-350 RS-Si_3N_4 at 1500°C shown in Fig. 20
indicate an almost time-invariant strength (n ~ 100). This is
also consistent with the fast fracture flexure test results,
wherein the strength was high at 1500°C and no evidence of SCG
was detected on the fracture surfaces. No evidence of SCG

58

Fracture Stress, ksi

100
90
80
70
60
50
40
30
20
10

10^{-1} 10^0 10^1 10^2 10^3 10^4 10^5 10^6

Time to Failure, minutes

Curve No.	Material/Temperature
1	G.E. Sint. SiC, 1500°C, n = 29
2	NC-350 RSSN, 1500°C, n = 97
3	NC-203 HP-SiC, 1500°C, n = 23
4	NC -132 HPSN (MgO), 1400°C, n = 16
5	NCX-34 HPSN (Y₂O₃), 1400°C, n = 12

GE HP and Sint. SiC, 1600°C (Trantina and Johnson(⁹)), n = 30
HS-130 HPSN (MgO), 1400°C (Evans and Wiederhorn(10)), n = 10
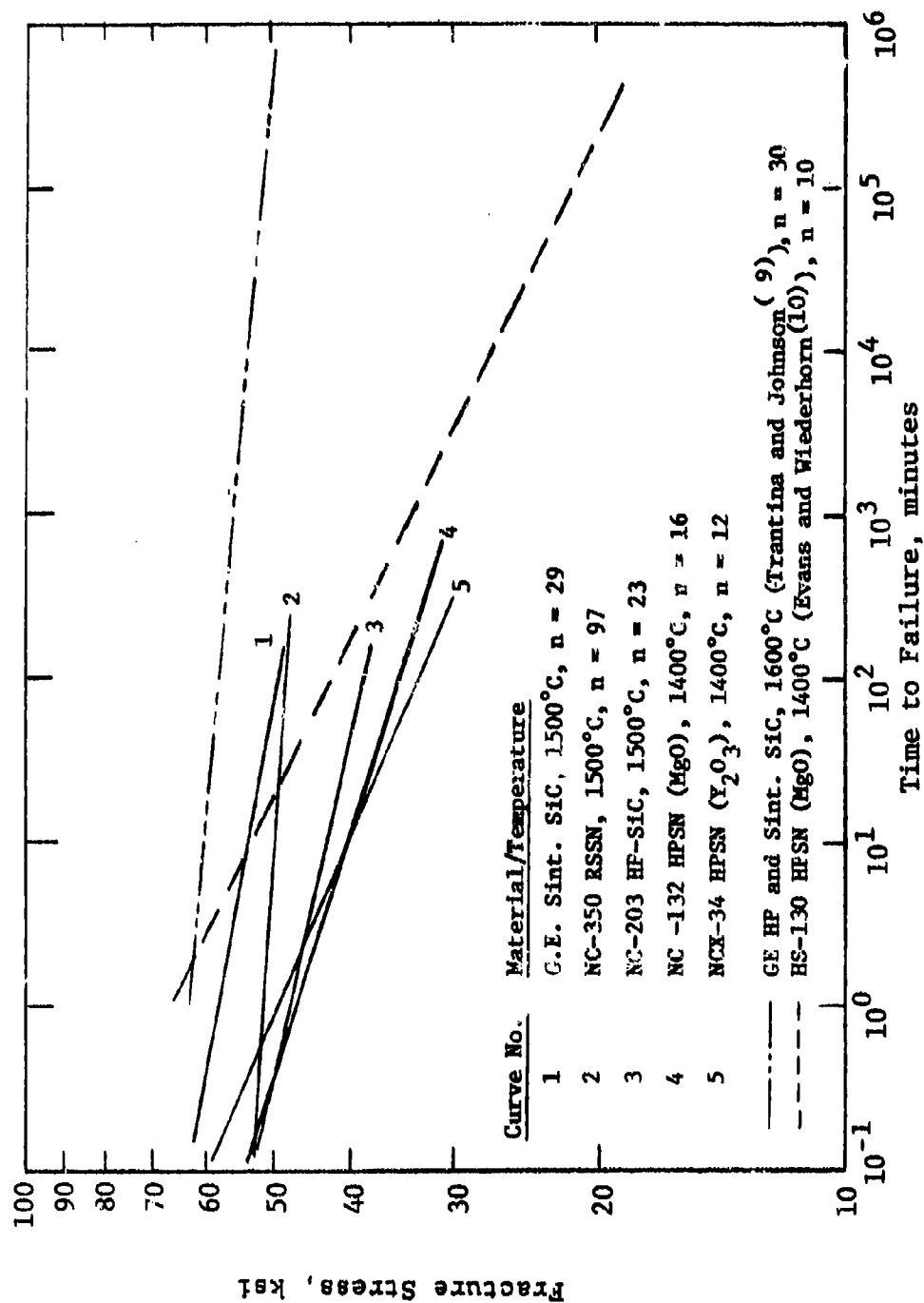
Figure 20. Strength Degradation by Subcritical Crack Growth
(Differential Strain-Rate Flexure Tests)

59

was noted on the fracture surfaces of the differential strain rate test samples, either. However, a few spherical-shaped silicon droplets were observed at several locations on the fracture surfaces, as well as the tensile and compressive surfaces of the sample.

Therefore, based on this study the materials tested would be ranked for resistance to strength degradation by subcritical crack growth in the following order: (1) $RS-Si_3N_4$, (2) sintered SiC, (3) HP-SiC, and (4) $HP-Si_3N_4$, regardless of whether it is MgO- or Y_2O_3-doped.

SECTION VII

ENVIRONMENTAL EFFECTS - LONG-TIME OXIDATION EXPOSURE

Comparatively little is currently known about the long-term strength of silicon-base ceramics subjected to aggressive environments. Oxidation and corrosion effects can cause strength degradation by altering the strength-controlling flaw distribution existing in the virgin material. That is, the oxidized or corroded areas on and below the surface can become the fracture sources. Also, long-term oxidative exposure can result in other types of microstructural effects such as phase instability, destabilization, or dissociation. Short-term oxidation of RS-Si_3N_4 can also have the beneficial effect of increasing strength by crack tip blunting or porosity modification as discussed above. The silicon nitride literature[11] contains various references to the long term exposure of HP-Si_3N_4 leading to degradation of strength by the formation of pits in the matrix material (i.e., Si_3N_4 below the oxide layer) which serve as fracture origins.

Oxidation behavior, i.e., rate and scale morphology, is known to be strongly dependent on the specific impurities present in the Si_3N_4 or SiC body. Accordingly, various materials available in this program were subjected to long-term exposure in static air for times of 100, 1000, and 2000 hours at temperatures from 1000° to 1500°C to assess micro-structural/surface stability. Test temperatures and exposure times were selected for each material type as follows:

MgO-doped HP-Si_3N_4	:	1200°C/100, 1000 hr.
Y_2O_3-doped HP-Si_3N_4	:	1000°C/100, 1000 hr.
RS-Si_3N_4	:	1400°C/100, 1000 hr.
HP-SiC, sintered SiC	:	1400°C/100, 1000 hr.
Siliconized SiC	:	1200°C/100, 1000 hr.
Sintered SiC	:	1500°C/2000 hr.

Post-exposure evaluation involves weight change, residual
25°C bend strength (with fracture source identification),
and examination of the surface oxide scale with an optical
stereo-microscope and SEM. Evaluation of the nature of the
oxide scale by optical microscopy is reported herein. The
residual strength, weight change, and SEM evaluation will be
reported on Contract F33615-79-C-5100, where many additional
silicon base materials will be evaluated. In the current
program only selected materials were subjected to the long-
term high temperature static air exposure. On the follow-on
program it is intended to similarly expose all of the
materials available. This means that some exposure samples
will consist of small pieces of perhaps room temperature
tested bend bars for materials for which long term exposure
was not accomplished on the current program. On such samples
post-exposure evaluation will therefore consist of weight
change and surface examination only.

The nature of the scales formed on the oxidized samples
thus far studied is consistent with what is known about their
microstructure and purity. The literature contains several
useful works on this subject. [12-20] The specific scale
morphology observed is directly related to how the impurities
modify the protective SiO_2 scale initially formed on Si_3N_4
and SiC.

Figure 21 illustrates the surface of Refel Si/SiC exposed
for 1000 hr at 1200°C.* The oxide scale is smooth and dull
in appearance, with only a very slight evidence of fine white
crystallized particles. An occasional pit in the oxide

*Each material was exposed at a temperature consistent with
its overall capabilities. Even though we are comparing
materials oxidized at different temperatures, the nature of
the scale deposit can still be meaningfully related to the
material microstructure and purity in a general sense.

12X

Figure 21. Surface of UKAEA/British Nuclear Fuels Refel
SiC (Siliconized, diamond-ground) Sample
After 1000 hr, 1200°C Static Air Exposure

63

surface was seen. This Si/SiC is extremely pure. Spectrographic analysis (Table 7) indicates that the only detectable element present other than Si is Fe. This high purity results in very little modification of the initial SiO_2 protective oxide layer formed upon exposure.

Figure 22 shows the surface of Carborundum sintered α-SiC exposed at 1400°C for 1000 hr. A smooth dull scale has formed, and there also is the presence of small crystalline particles and occasional pitting of the oxide layer. However, the splotchy decorated appearance shown in Fig. 22 is an indication of the effect of one of the impurities present. Spectrographic analysis (Table 7) indicates that, along with Fe (which apparently did not cause this decoration since it was present in the Si/SiC also), there exists Al, B, and W impurities. Apparently the impurities segregate in grain boundary regions and diffuse to the surface to interact with the initial SiO_2 scale during exposure.

Figure 23 illustrates the nature of the surface of G.E. sintered β-SiC that was also exposed for 1000 hr at 1400°C. It is seen that the white crystallized particles are much more pronounced on this material, and that large areas of a thick glassy coating are evident. The large circular glassy areas resemble the circular splotchy decorations that were present on a finer scale in Carborundum sintered α-SiC shown in Fig. 22. Thus it might be inferred that the same impurity species were responsible. Spectrographic analysis indicates about the same levels of Al and B impurity for these two sintered SiC. The General Electric material has, however, much greater tungsten impurity, as well as Co present. The G.E. material is not as pure as the Carborundum SiC, and this is reflected in the stability of the protective SiO_2 scales formed. Figs. 24 and 25 illustrate the appearance of the G.E. material after 2000 hr at 1500°C. The significance of these photographs is the pronounced difference in morphology of the crystalline scales. Apparently the impurity that causes this modification of the SiO_2 scale is rather non-uniformly distributed in the G.E. sintered SiC material.

64

12X

Figure 22. Surface of Carborundum Sintered ∝-SiC Sample
After 1000 hr, 1400°C Static Air Exposure

5.3X

12X

Figure 23.   Surface of General Electric Boron-Doped
             Sintered β-SiC Sample After 1000 hr, 1400°C
             Static Air Exposure

12X

Figure 24.   Surface of General Electric Boron-Doped
Sintered β-SiC Sample After 2000 hr, 1500°C
Static Air Exposure

12X

Figure 25.   Surface of General Electric Boron-Doped
             Sintered β-SiC Sample After 2000 hr, 1500°C
             Static Air Exposure

The oxide scale on the Al_2O_3-doped HP-SiC materials
from Ceradyne (1400°C/1000 hr.) and Norton (NC-203, 1500°C/
2000 hr.) are shown in Figs. 26 and 27, respectively. The
scale consisted of a very smooth shiny coating with evidence
of many very small uniformly distributed crystallites. This
behavior is typical of HP-SiC with Al_2O_3 additive. The Al_2O_3
(i.e., Al cations) and perhaps other impurity elements (Fe)
diffuse along grain boundaries to the SiC-SiO_2 interface,
where they lower the devitrification temperature of the silica
glass by reducing its viscosity (i.e., removing one of the
primary kinetic barriers to the nucleation and growth process).
The shiny nature of the oxide surface indicates that it may
have been liquid at the exposure temperature. Thus the
presence of primarily Al_2O_3 impurity greatly increases the
oxidation rate of SiC. The crystalline phase in the scale is
presumably mullite.

The appearance of the other type of hot-pressed SiC
studied, that with B_4C added to enhance densification, is
shown in Fig. 28. This material is Ceradyne HP-SiC (2% B_4C),
which was exposed at 1400°C for 1000 hr. The dull surface
with many rough crystalline scale deposits is much different
than the smooth glossy surface oxide observed for the Al_2O_3
doped HP-SiC. This behavior is apparently the result of the
boron impurity. Note that the appearance for HP-SiC (B_4C)
shown in Fig. 28, is very similar to the surface of the G.E.
sintered β-SiC shown in Fig. 25. The G.E. material is also
boron-doped. Boron presumably diffuses along grain boundaries
and interacts with SiO_2 at the SiC-SiO_2 interface to produce
this highly crystalline scale.

The silicon nitride materials also exhibit oxide scale
stability that is primarily controlled by impurities. Norton
NC-350 RS-Si_3N_4 was discussed above to the purest Si_3N_4
studied on this program (refer to spectrographic analysis,
Table 7). Figure 29 illustrates the practically non-existent
scale (for optical microscopy) on NC-350 that was exposed for

69

12X

Figure 26. Surface of Ceradyne Ceralloy 146A, HP-SiC
(2% Al_2O_3) Sample After 1000 hr, 1400°C
Static Air Exposure

70

12X

Figure 27. Surface of Norton NC-203, HP-SiC (2% Al_2O_3)
Sample After 2000 hr, 1500°C Static Air
Exposure

71
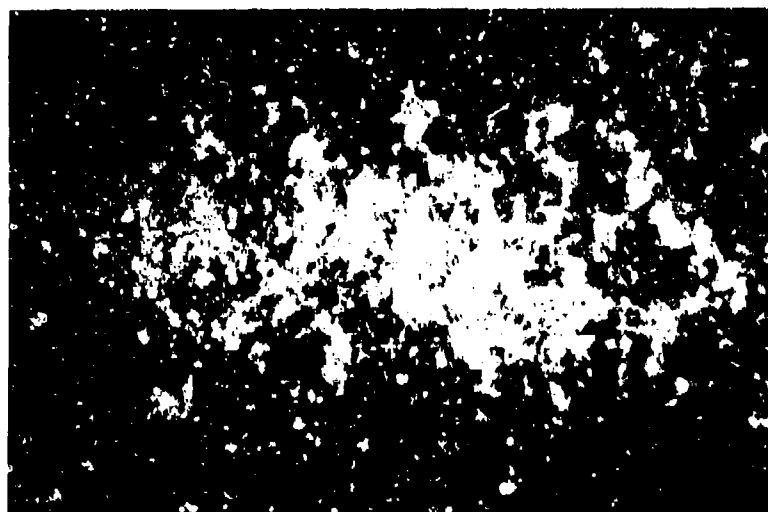
12X

Figure 28. Surface of Ceradyne Ceralloy 146I, HP-SiC (2% B_4C) Sample After 1000 hr, 1400°C Static Air Exposure

12X

Figure 29. Surface of Norton NC-350 RS-Si₃N₄ Sample
After 1000 hr, 1400°C Static Air Exposure

1000 hr at 1400°C. Figure 30 illustrates the Ford (IM)
RS-Si$_3$N$_4$ that was similarly exposed. The surface appeared
very stable similar to NC-350, except for a few reddish
oxide spots, presumably due to the comparatively high Fe
impurity in this material (it is iron-doped as previously
discussed). Figures 31 and 32 show the surfaces of AiResearch
injection molded and slip cast RS-Si$_3$N$_4$ materials, after
1400°C/1000 hr exposure. The injection molded version
(Airceram RBN-122) exhibits an oxide scale that is less
modified by the impurities present than is the surface of
slip cast Airceram RBN-101. These surface stability results
are consistent with the other properties measured on this
program, i.e., that NC-350 is the purest RS-Si$_3$N$_4$ with the
best properties. Regarding oxidation resistance of the re-
action sintered Si$_3$N$_4$ materials, Singhal[12] points out that
it is strongly influenced by porosity, pore size, and pore
size distribution. Having significant open porosity, RS-Si$_3$N$_4$
materials show the interesting effect of lower total oxidation
at higher temperatures (>1200°C) than at lower temperatures
(1000-1100°C). At low temperatures most of the oxidation is
internal through the network of surface-connected porosity.
Above typically 1200°C the open porosity at the surface is
rapidly sealed off by the continuous surface SiO$_2$ layer, thus
preventing internal oxidation. Since impurity diffusion is
not the rate controlling step for oxidation in RS-Si$_3$N$_4$, then
perhaps the process is controlled by the inward diffusion of
oxygen through the SiO$_2$ layer, or the rate of N$_2$ gas evolution
at the Si$_3$N$_4$-SiO$_2$ interface.

Hot-pressed Si$_3$N$_4$ materials have large amounts of impurity
phase and thus exhibit the opposite extreme of surface stability
when compared to the pure RS-Si$_3$N$_4$ materials. Figure 33 presents
the surface of Ceradyne HP-Si$_3$N$_4$ (1% MgO) that has undergone
1200°C/1000 hr exposure. The Mg and other impurities such
as Ca diffuse up through the grain boundary to the initial SiO$_2$
scale. The resulting oxide scale on HP-Si$_3$N$_4$ (MgO) is typically
crystalline enstatite MgSiO$_3$. The impurities that segregate
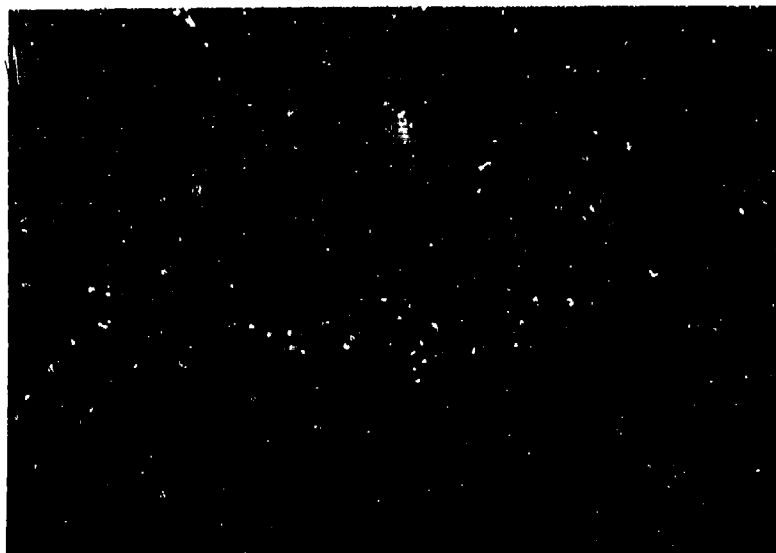
12X

Figure 30. Surface of Ford Injection Molded RS-Si$_3$N$_4$
Sample After 1000 hr, 1400°C Static Air
Exposure

75
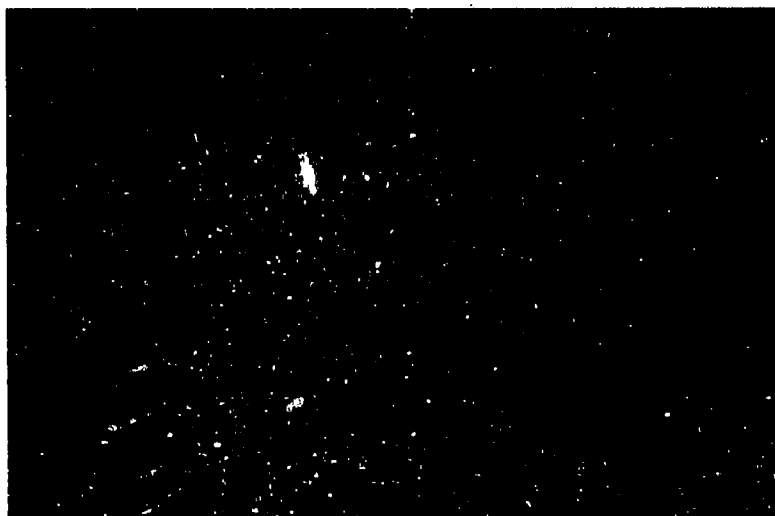
12X

Figure 31. Surface of AiResearch Injection Molded
RS-Si$_3$N$_4$ (Airceram RBN-122) Sample After
1000 hr, 1400°C Static Air Exposure

76

12X

Figure 32.   Surface   of AiResearch Slip-Cast RS-Si$_3$N$_4$ (Airceram RBN-101) Sample After 1000 hr, 1400°C Static Air Exposure
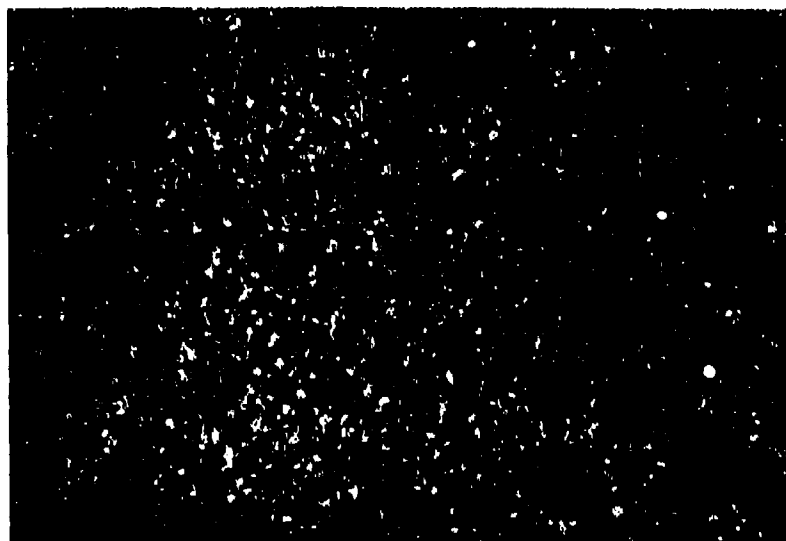
12X

Figure 33.   Surface of Ceradyne Ceralloy 147A HP-Si_3N_4 (1% MgO) Sample After 1000 hr, 1200°C Static Air Exposure

in the grain-boundary glass phase of the unexposed Si_3N_4 also diffuse to the surface oxide, where they either form mixed silicates or dissolve into the amorphous phase of the surface oxide.[12] Thus, oxidation in MgO-doped HP-Si_3N_4 is controlled by Mg ions diffusing from the grain boundary up through the SiO_2 layer to produce enstatite scale products. This scale is further modified by any Ca, Fe, Al, K, etc., impurities present.

The Y_2O_3-doped HP-Si_3N_4 materials exhibit extremely interesting behavior. Figure 34 illustrates the appearance of Norton NCX-34 HP-Si_3N_4 (8% Y_2O_3) exposed for 1000 hr at 1000°C. In general, the oxidization resistance and surface scale integrity was excellent for NCX-34 as well as the Ceradyne Y_2O_3-doped HP-Si_3N_4 materials. Very dull, smooth, thin, stable layers are formed. There is no outstanding evidence of impurity-related modification of the SiO_2 scale in Y_2O_3-doped HP-Si_3N_4.* However, there is another phenomenon that occurs during 1000°C exposure, as illustrated for NCX-34 (8% Y_2O_3) and Ceradyne materials containing 8% and 15% Y_2O_3 in Figs. 34 to 38. The 8% Y_2O_3-doped materials from Ceradyne (Ceralloy 147Y-1) and Norton (NCX-34) begin to show the development of some form of phase instability after 100 and 1000 hr exposure at 1000°C. This particularly evident in the Ceradyne 8% Y_2O_3-doped material shown in Figs. 35 and 36. This effect is extremely catastrophic for higher Y_2O_3-contents. Figures 37 and 38 illustrate the Ceradyne 15% Y_2O_3-doped HP-Si_3N_4 samples that were exposed for 100 and 1000 hr at 1000°C. Note the severe cracking, distortion, and disintegration of the samples shown. Similar effects in Y_2O_3-doped HP-Si_3N_4 have been reported in the literature by Lange et al.[21,23] and Wills et al.[22] Current belief is that at intermediate temperatures (e.g., 1000°C) an unstable yttrium-silicon oxynitride phase is formed by an oxidation mechanism. Singhal[12] indicates that the problem relates to one or more silicon-yttrium oxynitride

---

*The same conclusion was reached upon examination of the fracture surfaces and tensile/compressive surfaces of NCX-34 bend bars, where NCX-34 and NC-132 received identical 1500°C exposure.

79
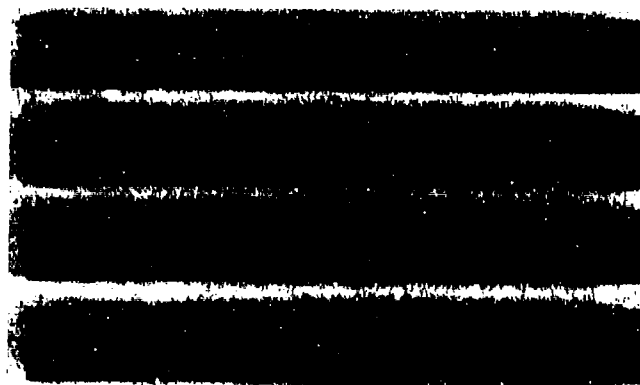
1.5X

12X

Figure 34. Surfaces of Norton NCX-34 HP-Si₃N₄ (8% Y₂O₃) Samples After 1000 hr, 1000°C Static Air Exposure

1.5X

5.3X

Figure 35. Surfaces of Ceradyne Ceralloy 147Y-1 HP-Si$_3$N$_4$ (8% Y$_2$O$_3$) Samples After 100 hr, 1000°C Static Air Exposure (Edge Surface)

1.5X

12X
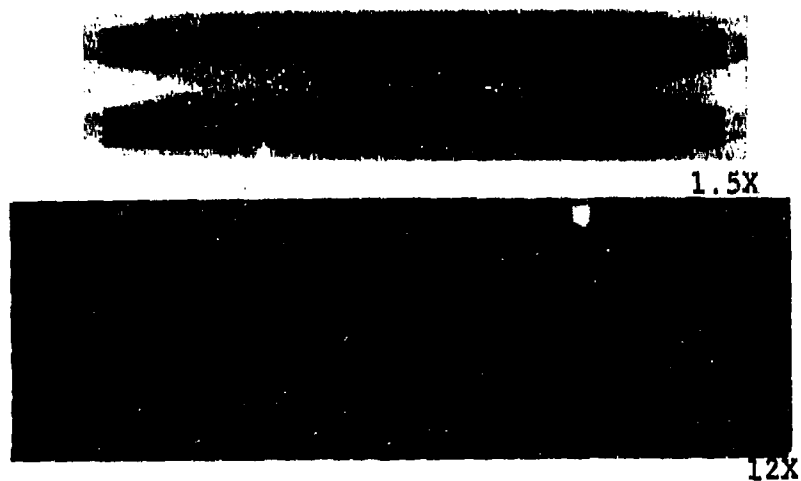
Figure 36. Surfaces of Ceradyne Ceralloy 147Y-1 HP-Si$_3$N$_4$
(8% Y$_2$O$_3$) Samples After 1000 hr, 1000°C Static
Air Exposure

1.5X

5.3X
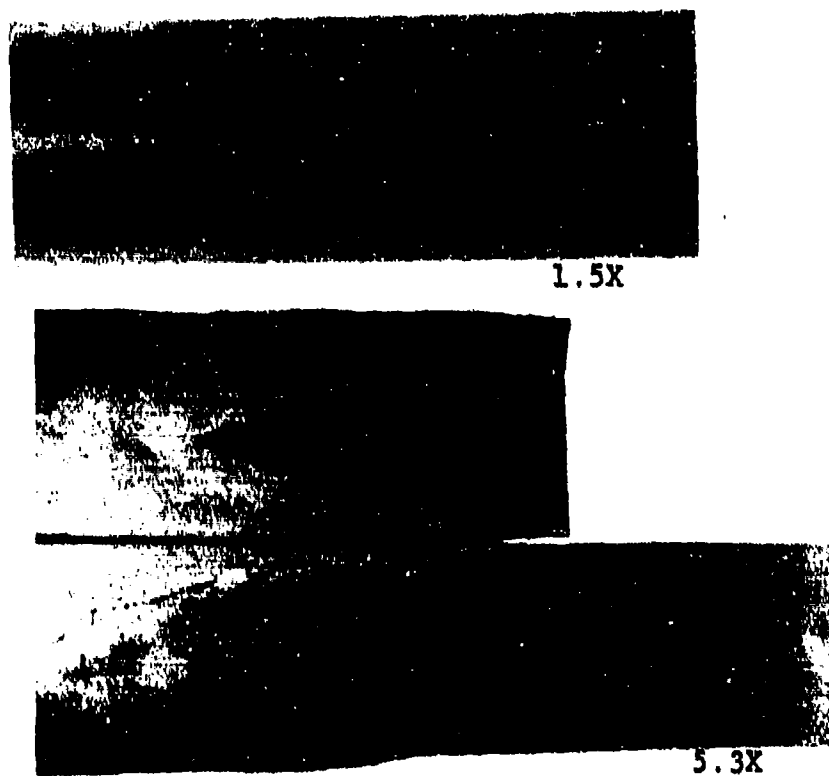
Figure 37. Surfaces of Ceradyne Ceralloy 147Y HP-Si$_3$N$_4$
            (15% Y$_2$O$_3$) Samples After 100 hr, 1000°C
            Static Air Exposure

1.5X

5.3X

Figure 38.   Surfaces of Ceradyne Ceralloy 147Y HP-Si$_3$N$_4$
(15% Y$_2$O$_3$) Samples After 1000 hr, 1000°C
Static Air Exposure

phases that exhibit accelerated oxidation caused by non-protective oxide scales. The volume increase that results eventually causes catastrophic failure in the $HP\text{-}Si_3N_4$ system containing these phases. This degradation has been reported to be less severe at higher temperature (i.e., 1300-1400°C) where it is speculated that increased oxidation rates seal off the surface preventing oxidation of the internal unstable phase. Figure 39 illustrates samples of Ceradyne 15% Y_2O_3-doped HPSN that were creep tested at 1350°C for 70-100 hr. The degradation of the samples appears less severe for 1350°C exposure than for the 1000°C exposure (Fig. 37). The origin of the diamond-shaped markings on the samples shown in Fig. 39 is unknown (it is also apparent in Figs. 37 and 38), but it is certainly related to the $Y_2O_3 \cdot Si_3N_4$ phase instability. It is significant to note in Fig. 38 that two similarly exposed samples are shown, one having experienced relatively little degradation. This would indicate that this effect may be strongly related to the non-uniform distribution of Y_2O_3 within the material.

Current research in Y_2O_3-doped $HP\text{-}Si_3N_4$ materials involves methods of eliminating such phase instabilities, while still retaining the improved properties at elevated temperatures when compared to MgO-doped $HP\text{-}Si_3N_4$ that have previously been reported.[24] Norton has approached this by reducing the Y_2O_3 content. NCX-34 resulted from this work at Norton with 8% Y_2O_3 addition and the claim that the intermediate temperature phase instability had been eliminated.[25] Our current results suggest that the instability still exists in some batches of NCX-34. AMMRC has reported the elimination of the intermediate temperature degradation by heat treatment of the processed material in a nitriding environment.[26]

1.5X

Figure 39. Surface of Ceradyne Ceralloy 147Y HP-Si$_3$N$_4$
(15% Y$_2$O$_3$) Samples After Creep Testing
70-100 hr/1350°C in Air

SECTION VIII

FRACTURE TOUGHNESS

The potential use of ceramics in gas turbines and other structural applications requires careful consideration of the brittle nature of these materials. Their fracture toughness or resistance to crack propagation is much lower than that of metals, and when failure occurs it does so in a rapid and catastrophic manner. The conditions controlling fracture may be considered in terms of fracture initiation or crack propagation. Fracture may occur if the applied stress is increased or intensified locally around a flaw such that it exceeds the theoretical strength of the material. Alternatively, cracks will propagate as long as the rate of strain energy release is greater or equal to the energy needed for forming new crack surface. The parameters that are most often used to characterize the fracture toughness of ceramics are K_{IC}, the critical stress intensity factor, and γ the fracture surface energy.

Under some conditions of stress and environment, cracks may also grow slowly in ceramics until they reach a critical size and failure occurs. Because of this phenomenon of subcritical crack growth, the relation between stress intensity and the rate of crack advance (K_I vs. da/dt or v) and the level of stress intensity (K_o) below which no crack propagation occurs are also important parameters for designing with brittle materials.

Several experimental techniques have been developed to measure these parameters, but each has advantages and limitations such that no particular method has found universal favor at this time. These include the single-edge notched beam (SENB), the compact tension (CT), the double cantilever beam (DCB), the tapered cantilever beam (TCB), the constant moment (CM), the double torsion (DT), the controlled flaw (CF) and the natural flaw (NF) methods. It is desirable that the test simulate as closely as possible the stress state at the tip

of naturally occurring flaws in ceramics, permit testing in a variety of hostile or high temperature environments, and have a simple and inexpensive sample geometry.

The exact nature of the stress at a crack tip or flaw, and the geometry of the crack front before and during crack propagation continue to be the most nebulous and ambiguous features of fracture toughness testing. The double torsion sample has a curved crack front that is receiving increased critical attention as being invalid for slow crack growth studies because it may not be a constant K_I test geometry as originally thought. Additionally, the double torsion crack front is also quite large compared to actual flaws in ceramics, thus reducing or eliminating microstructural inhomogeneity-related effects from DT test data. In the natural and controlled flaw techniques, the flaw size, shape, and location must be determined by post-test fractographic examination. Both NF and CF techniques result in significant data scatter and sample-to-sample variability. The CF technique has various experimental variables and uncertainties; namely, indenter load and type (i.e., Knoop or Vickers), method of eliminating or correcting for possible residual stress effects, uncertainty in the measured flaw size, magnitude of the stress intensity magnification factor, use of plasticity correction factors, etc. Also, there is a tendency for CF samples to fracture at sites other than the induced flaw for tests conducted at elevated temperature in air. This is due to the influence of oxidation altering the crack tip sufficiently to permit activation of intrinsic critical flaws instead of the artifically induced one. Improved experimental techniques may eventually overcome this problem through preloading, "popping-in" the induced flaw, changing the indenter load and/ or geometry, etc. Regarding residual stresses, it appears that surface grinding may eventually prove to be a better method than annealing or applying a constant correction factor.

The concept of applying a constant correction factor of $\sim 30\%$ was suggested by Lawn.[27] Recently, however, several investigators have questioned whether the residual stress effect is that significant, if existent at all.

Fracture toughness, i.e., the critical stress intensity factor, has been measured on this program by double torsion (DT), controlled flaw (CF), and indentation dimension (ID) techniques. CF data are generally equivalent to or slightly lower than DT data, presumably reflecting the increased fracture resistance to propagate a longer DT crack front. Both techniques result in significant data scatter and sample-to-sample variability. The CF technique has various experimental variables and uncertainties as described above. The indentation dimension (ID) technique has not resulted in good agreement with CF and DT data. To summarize the techniques, the DT method is preferred based on our results. The CF technique involves an analytical basis that is not highly developed, indented flaws heal when testing in air at elevated temperature, and is always dependent on the sometimes subjective measurement of flaw dimensions. The ID technique apparently does not have a highly developed theoretical/analytical base, and needs further work for the wide range of material microstructures studied in this program.

Figure 40 is an attempt to put all of the fracture toughness data generated on this program into overall perspective. A K_{I_c}-T plane is shown, on which is plotted regions of fracture toughness data for each material measured. The numbers and letters plotted refer to the first letter of the IITRI sample identification code which indicates material manufacturer and type (see Table 2). Multiple entries in Fig. 40 indicate average values obtained by different techniques. However, no ID data are plotted in Fig. 40.
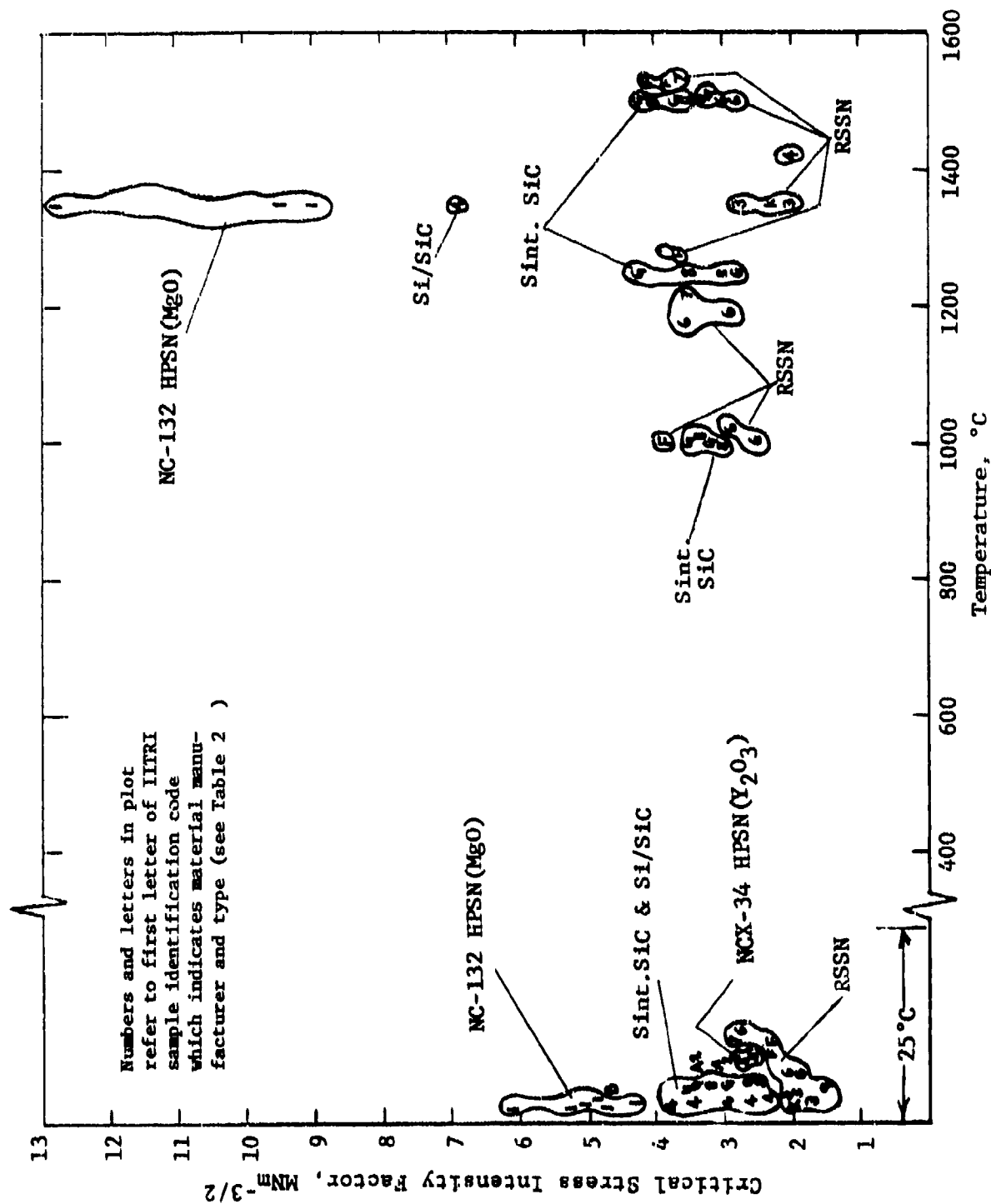
Figure 40. Fracture Toughness of Various Silicon-Base Materials

Even though there is significant technique related data scatter, the different material types fall into several distinct regions of K_{Ic} behavior as illustrated in Fig. 41. For instance, NC-132 HP-Si_3N_4 (1% MgO) exhibits the highest fracture toughness, presumably due to its high density, uniformity of microstructure, and absence of significant process-related defects. The large increase in fracture toughness with temperature for NC-132 is due to its glassy silicate grain boundary phase. This large increase in K_{Ic} should not be considered good, since it is accompanied by very significant strength and modulus reduction as well. Norton NCX-34 Y_2O_3-doped HPSN has lower fracture toughness at room temperature than MgO-doped NC-132. Kyocera SN-3 HPSN also has lower K_{Ic} than NC-132.

The various forms of SiC tested, i.e., sintered and siliconized, indicate fracture toughness lower than HP-Si_3N_4, presumably related to higher elastic modulus. All SiC materials are fairly tightly grouped in Fig. 41 with little scatter. All forms of SiC, especially Si/SiC, exhibit increase in fracture toughness with temperature. For the sintered materials this is most probably due to an oxidation effect at the crack tip. For the siliconized material it is possibly related to the incipient melting of the silicon-rich phase.

The lowest fracture toughness is exhibited by the RS-Si_3N_4 materials, related to their low strength/high porosity. Two distinct regions exist, one for the Ford injection molded and AiResearch slip-cast materials (higher K_{Ic}), and the other for Norton NC-350 and KBI materials (lower K_{Ic}). The Ford and AiResearch materials have high density (2.8 gm/cc) and good strength. It is mildly surprising that NC-350 has lower fracture toughness, since despite its slightly lower density (2.5 gm/cc) it has excellent high

91
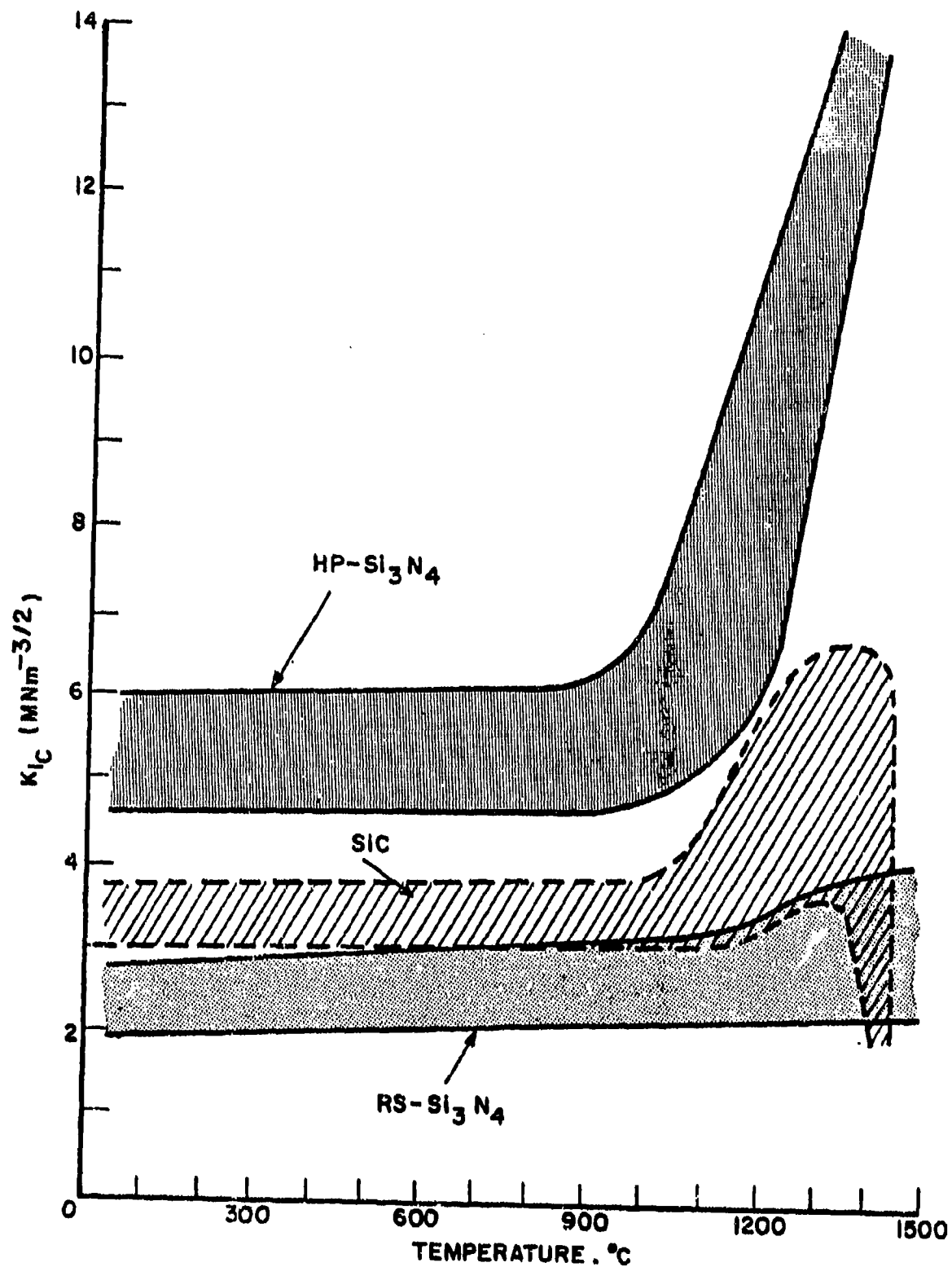
Figure 41.   Fracture Toughness: Critical Stress Intensity Factor

92

temperature strength (but slightly lower room-temperature strength). It is also noted that Kyocera SN-201 sintered Si_3N_4 has good room temperature fracture toughness.

To summarize, RS-Si_3N_4 materials have K_{I_c} ranging from $\sim$1.5-2.8 MNm$^{-3/2}$ at room temperature, and $\sim$2-4.2 MNm$^{-3/2}$ at elevated temperature. Silicon carbides exhibit K_{I_c} values ranging from $\sim$2.4-3.8 MNm$^{-3/2}$ at 25°C, and $\sim$3-4.3 MNm$^{-3/2}$ at high temperature. Hot-pressed Si_3N_4 exhibits a room temperature fracture toughness in the range $\sim$4.3-6.2 MNm$^{-3/2}$. These data bands are illustrated in Fig. 41.

Regarding measurement technique, data for silicon-base ceramics obtained from double torsion and controlled flaw techniques all fall in fairly predictable bands. When compared to metals, it does not matter which technique is used to obtain fracture toughness data for ceramics - all classes of silicon-base ceramics are roughly an order of magnitude lower than metals. However, if one is interested in a basic study of the fracture process in ceramics, then test technique can be very important. Based on present data, there is no one ceramic material that has fracture toughness significantly higher than others. There appears to be no manufacturing process for conventional silicon-base ceramics that offers any great clearcut advantage. Thus, to make major improvements in the fracture toughness of advanced heat engine (ceramic) materials, it appears that innovative ceramic materials must be developed; for instance, ceramic-ceramic composites. Efforts in this direction are currently being pursued at various laboratories in this country.

SECTION IX

CREEP RESISTANCE

Creep resistance is of primary concern in the rotating components of a turbine engine. High creep rates can lead to both excessive deformations and uncontrolled stresses.

Creep is a thermally activated process, characterized by a linear or power law stress dependence. After load application there is an instantaneous strain, followed by three regions of creep behavior. Primary creep (transient) is characterized by a creep rate that continually decreases with time. This is followed by secondary (steady-state) creep behavior where the creep rate remains constant with increasing strain and time. Tertiary creep can be observed just prior to fracture in some materials and is characterized by a rapid increase in creep rate. Steady-state secondary creep behavior is of greatest interest in structural applications. The steady-state creep rate, $\dot{\varepsilon}$, is governed by the empirical relation:

$$\dot{\varepsilon} = A\sigma^n e^{-E/kT} \tag{6}$$

Creep deformation mechanisms are deduced in part by analysis of measured creep rates with respect to this relation. Experimental schedules normally cover a range of stress and temperature which permit analytical determination of the stress exponent, n, and activation energy, E. A knowledge of the stress exponent and activation energy permits some mechanistic interpretation, which is important in understanding the measured behavior and eventually improving materials properties. However, this information alone is not sufficient for a comprehensive mechanistic study. Microstructural analysis of crept specimens using light microscopy and scanning, replica, and transmission electron microscopy can reveal features that suggest the rate-controlling mechanisms involved. Such features include grain boundary sliding, wedge-type cracking, porosity on grain boundaries, dislocations, etc.

94

Flexural creep behavior was measured on this program by the stepwise method, generally at one temperature in air atmosphere. Samples were tested at various incremental stress levels, with enough time spent at any given stress to obtain steady-state (secondary) creep. The log $\dot{\epsilon}$ vs. log σ data for all materials evaluated are presented in Fig. 42 (hot-pressed Si_3N_4), Fig. 43 (reaction-sintered Si_3N_4), and Fig. 44 (silicon carbide materials). General data bands for each material type are presented in Fig. 45.

For the HP-Si_3N_4 materials shown in Fig. 42, Ceradyne 147A and Norton NC-132 materials both contain ~1% MgO and exhibit similar creep behavior at 1350°C. Norton NCX-34, containing 8% Y_2O_3 exhibits creep strength similar to NC-132 (1% MgO) at 1500°C, but about an order of magnitude lower creep rates at 1350°C. This is apparently the result of the yttria additive forming a more creep-resistant grain boundary phase than the magnesia dopant. NCX-34 also exhibits a lower stress exponent than MgO-doped Si_3N_4. Thus a different deformation mechanism may be operative for the Y_2O_3-doped materials. Ceradyne's 8% Y_2O_3-doped Si_3N_4 (147Y-1) was tested at 1350°C, and did not exhibit the improved creep resistance of NCX-34. In fact the Ceradyne material is of lower creep strength than NC-132 at 1350°C. Ceradyne 147Y HP-Si_3N_4 (15% Y_2O_3) exhibited extremely low creep rates as shown in Fig. 42. However, as discussed in Section VII and illustrated in Fig. 39, this material decomposed during creep testing, so the apparent high creep strength shown in Fig. 42 has little meaning with regard to the use of this material as a high temperature structural ceramic.

Table 12 illustrates that the MgO-doped hot-pressed Si_3N_4 materials, and the Ceradyne 8% Y_2O_3-doped HPSN exhibited stress exponents 1.5 < n < 1.8. Stress dependency of this order (i.e., 1.6-2.0) has been reported previously for HP-Si_3N_4,[28-31] and has been interpreted as an indication that the deformation is controlled by viscoelastic effects.[32-34] This information

95
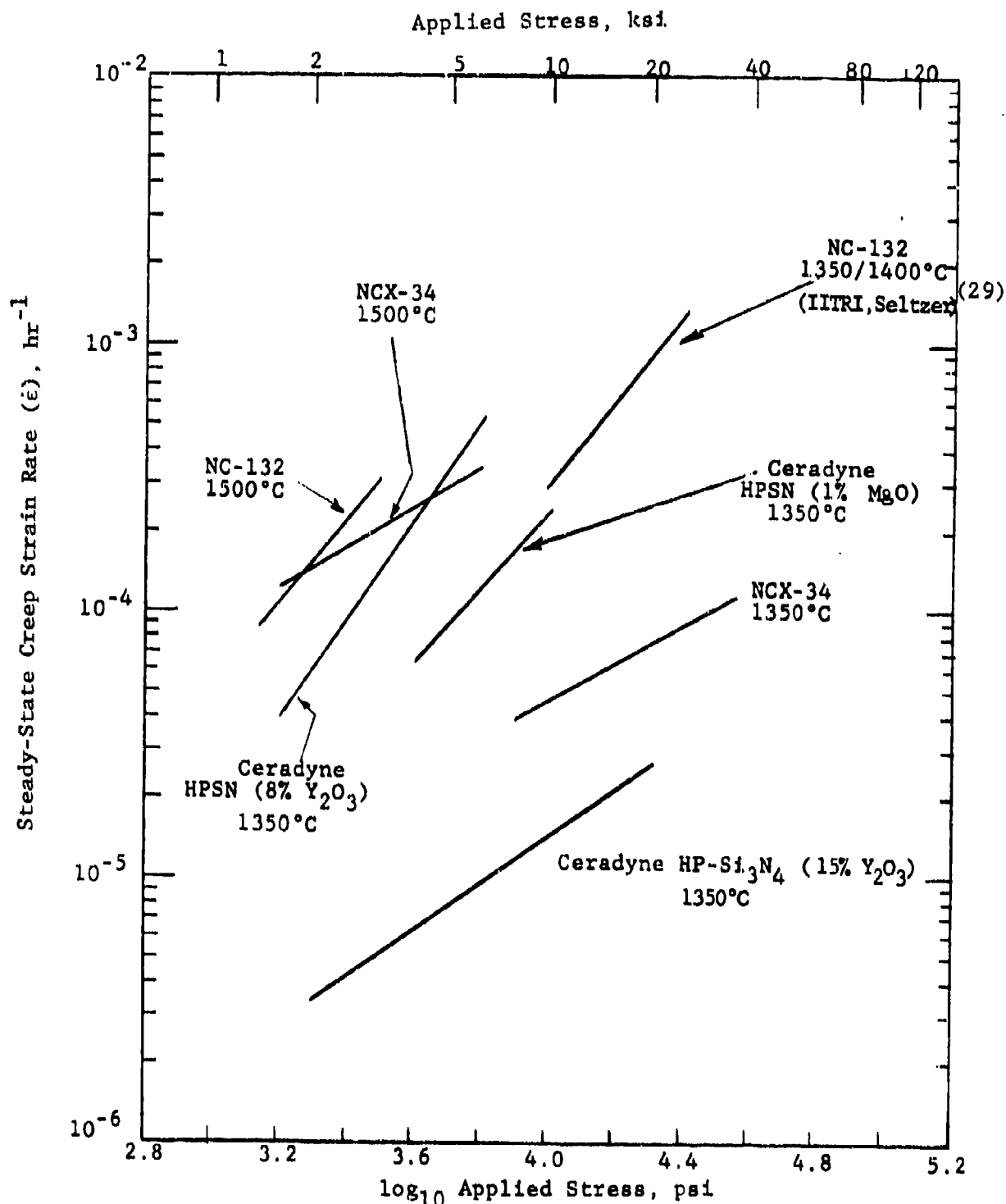
Figure 42. Steady-State Flexural Creep Rate vs. Applied Stress for Various Hot-Pressed Si_3N_4 Materials
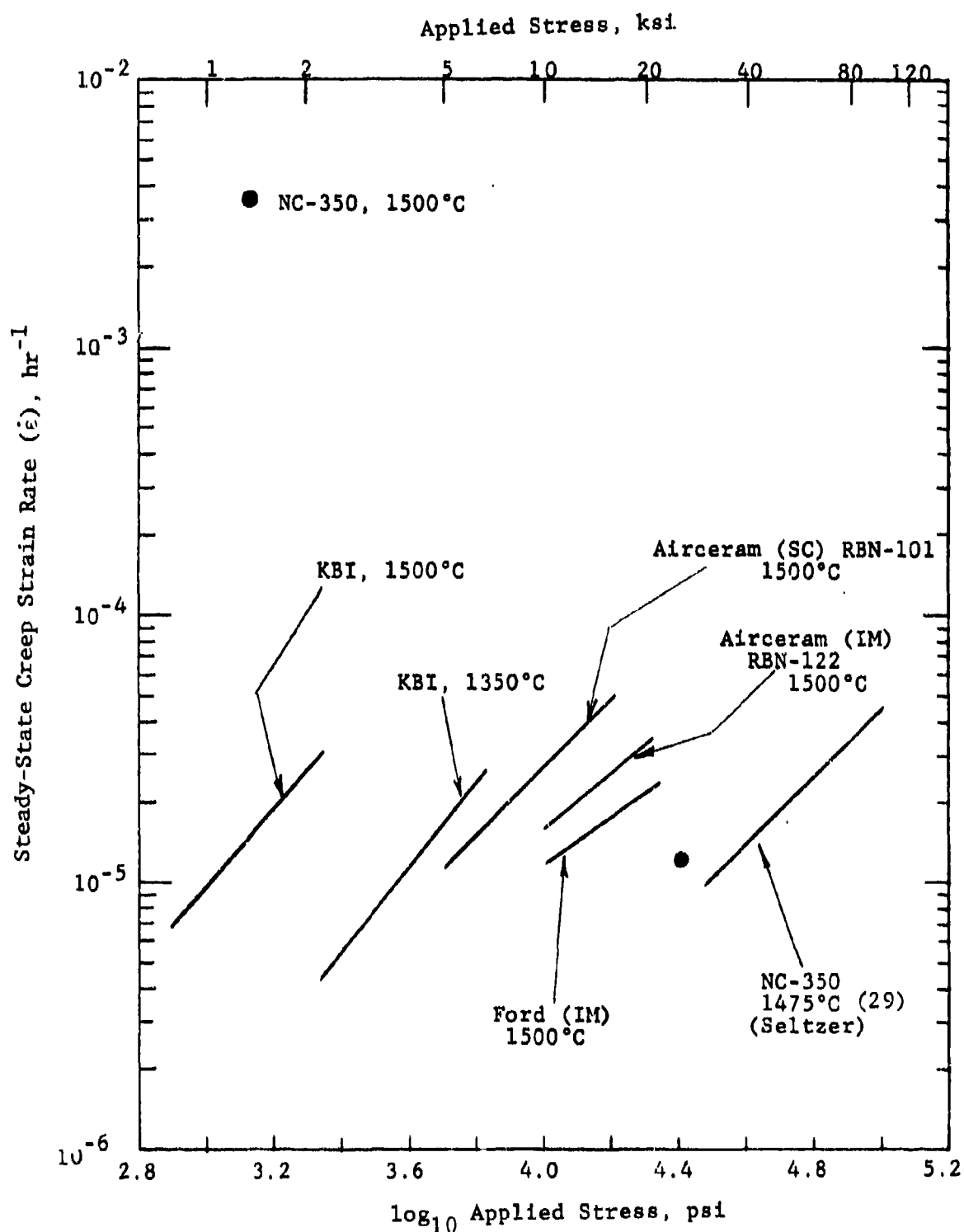
Figure 43. Steady-State Flexural Creep Rate vs. Applied Stress
for Various Reaction-Sintered Si_3N_4 Materials

97
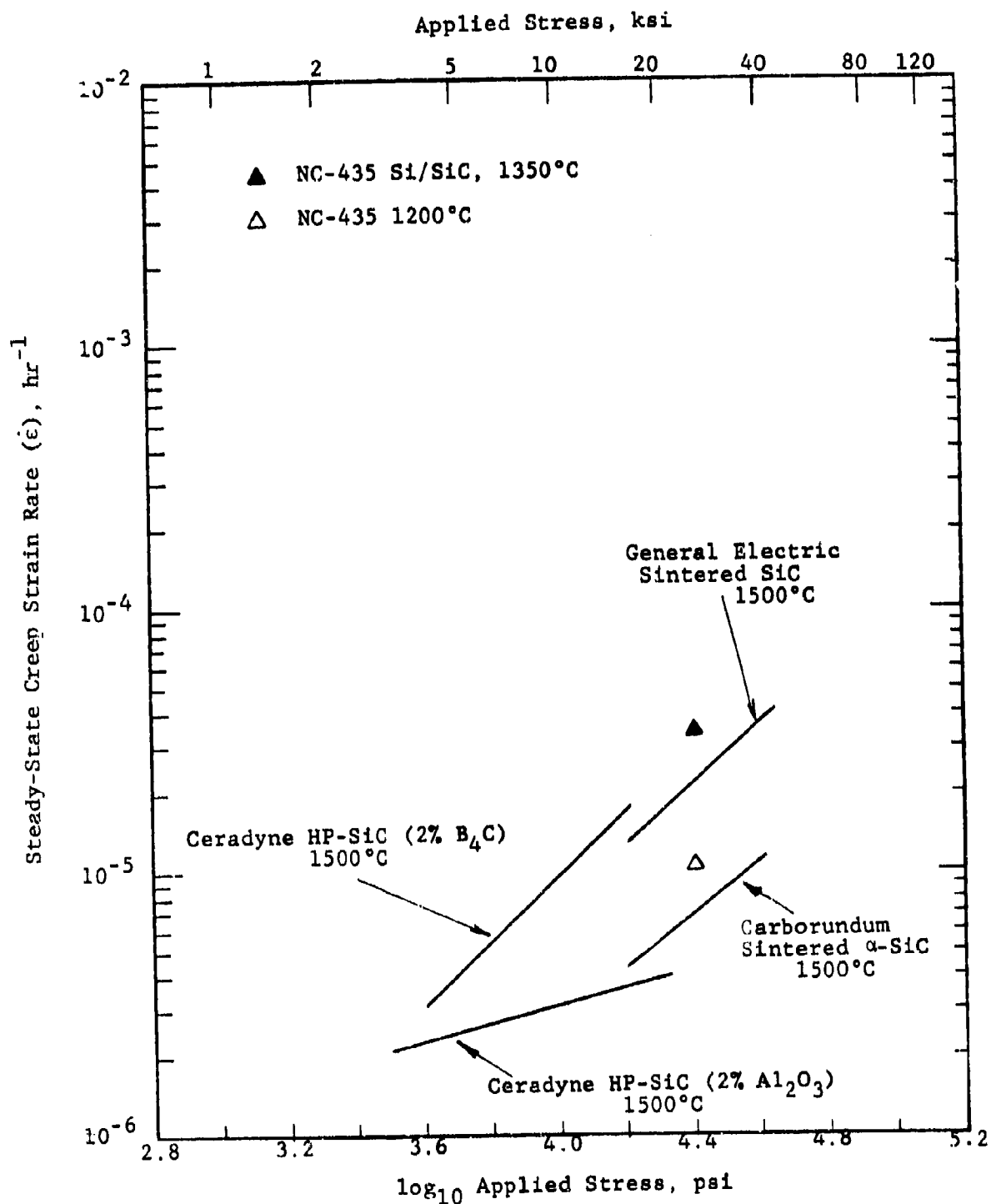
Figure 44. Steady-State Flexural Creep Rate vs. Applied Stress for Various Silicon Carbide Materials
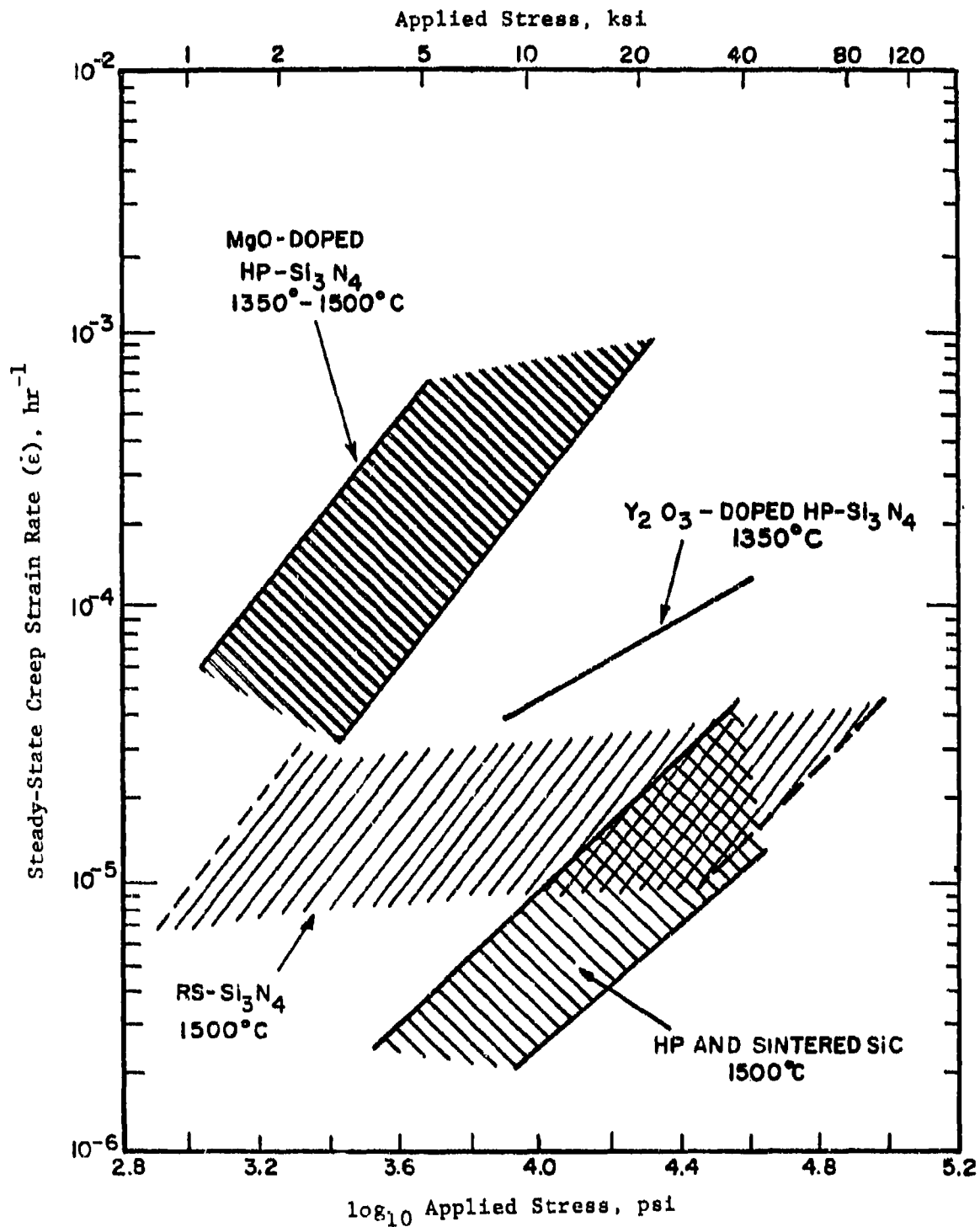
Figure 45.   Flexural Creep Behavior of Various Si_3N_4 and SiC Materials

TABLE 12

DERIVED CREEP STRESS DEPENDENCE AND ACTIVATION ENERGY FOR VARIOUS HP-Si_3N_4 MATERIALS STUDIED

Material	Temp., °C	Stress Exponent, n	Activation Energy, kcal/mole
Norton NC-132 (1% MgO)	1350 1500	1.6	130[a]
Ceradyne Ceralloy 147A (1% MgO)	1350	1.5	--
Norton NCX-34 (8% Y_2O_3)	1350 1500	0.7- 0.8	91
Ceradyne Ceralloy 147Y-1 (8% Y_2O_3)	1350	1.8	--
Ceradyne Ceralloy 147Y (15% Y_2O_3)	1350	0.9	--

[a] Computed from IITRI and Seltzer[28,29] data.

together with activation energy data for HP-Si$_3$N$_4$[28-31] and microscopic analysis of crept specimens,[30,31,35] has led to the belief that deformation in MgO-doped HP-Si$_3$N$_4$ is controlled by grain boundary sliding accommodated by the generation of or extension of triple point voids. Table 12 illustrates that Norton NCX-34 (8% Y$_2$O$_3$) exhibited substantially lower stress exponent and activation energy, and thus perhaps a different deformation mechanism. Langdon, et al.[32] have indicated that linear stress dependence (i.e., n = 1) would be obtained if the deformation process were diffusion controlled. Perhaps diffusion is more predominant than grain boundary sliding in the Y$_2$O$_3$-doped materials (e.g., NCX-34).

Figure 43 illustrates the creep rate vs. applied stress for the reaction-sintered Si$_3$N$_4$ materials. The higher creep strengths (lower creep rates) exhibited by RS-Si$_3$N$_4$ compared to HP-Si$_3$N$_4$ is a result of the relative purity of RBSN and lack of significant oxide grain boundary phases. Table 13 illustrates stress exponents of 1.1 $\pm$ 0.2 for the RBSN materials from Norton, Ford, and AiResearch. This stress dependence is in the range of that obtained for other RBSNs.[28,29,36-38] The higher stress exponent (n = 1.5-1.6) obtained for the KBI material might be explained in terms of higher effective applied stress due to increased porosity, or to the fact that this material has been judged not as well sintered as the others (refer to Section V). The effect of porosity on creep is discussed by Langdon.[39]

Ud Din and Nicholson,[37] and Grathwohl and Thümmler[38] have stress dependence, activation energy, and microstructural evidence that indicates the same deformation mechanism for RBSN as for HPSN, i.e., grain boundary sliding accommodated by microcracking and boundary separation. However, Birch and Wilshire,[40] Birch et al.[41] and Lange[42] contend that the rate-controlling process in silicon nitride is not the

101

TABLE 13

DERIVED CREEP STRESS DEPENDENCE AND ACTIVATION ENERGY FOR VARIOUS RS-Si$_3$N$_4$ MATERIALS STUDIED

Material	Temp., °C	Stress Exponent, n	Activation Energy, kcal/mole
Norton NC-350	1500	1.3[a]	~90[b]
KBI	1350 1500	1.5- 1.6	74
Ford (IM)	1500	0.9	--
AiResearch (IM) Airceram RBN-122	1500	1.1	--
AiResearch (SC) Airceram RBN-101	1500	1.3	--

[a] Data of Seltzer.[28,29]

[b] Computed from IITRI and Seltzer data.

grain boundary sliding itself, but rather the microcrack formation necessary to accommodate the relative crystal movement. Our current data show indirect evidence that the creep deformation process is controlled by the fracture characteristics of these materials. The data for the RSSN (Fig. 43) illustrate that the stress levels for each material necessary to maintain a given steady-state creep rate (say, $1 \times 10^{-5} hr^{-1}$) are directly proportional to the 1500°C bend strengths for each material obtained previously (shown in Fig. 9). Thus, present data lend credence to the concepts of microcrack-controlled deformation offered by Birch, Wilshire, and Lange.

The results for SiC materials are shown in Fig. 44 and Table 14. Siliconized NC-435 was tested at 1350°C, while sintered and hot-pressed SiC materials were tested at 1500°C. The siliconized material is shown to be less creep resistant than hot-pressed or sintered SiC. The very low creep rates obtained for the hot-pressed and sintered SiC materials is a consequence of their high strength and lack of major impurity phases. Table 14 shows that stress exponents are close to unity, and activation energies are higher than for Si_3N_4. No explanation is currently available for the apparently very low stress exponent for Ceradyne Ceralloy 146A HP-SiC (2% Al_2O_3). A carbon-vacancy diffusion mechanism has been proposed to control the deformation in silicon carbide.[43-45]

In summary, most HP-Si_3N_4 studied to date (e.g., MgO-doped) exhibit high creep rates and have a stress dependence characterized by $1.5 < n < 1.8$. The exception to this is Norton NCX-34 HP-Si_3N_4, which is doped with 8% Y_2O_3 as a densification aid. NCX-34 has a lower creep rate at 1350°C than NC-132, a lower stress exponent (n~0.9), and apparently lower activation energy, perhaps indicating a different deformation mechanism. The RS-Si_3N_4 materials studied to date all have very good creep strengths due to the lack of significant oxide impurity phases. Stress exponents are lower than for

103

TABLE 14

DERIVED CREEP STRESS DEPENDENCE AND ACTIVATION ENERGY FOR VARIOUS SiC MATERIALS STUDIED

Material	Temp., °C	Stress Exponent, n	Activation Energy, kcal/mole
General Electric Sintered SiC	1500	1.1-1.2	210-250[a]
Carborundum Sintered SiC	1500	1.1	--
Norton NC-435 Si/SiC	1200 1350	0.9[b]	235[c]
Ceradyne Ceralloy 146A HP-SiC (2% Al_2O_3)	1500	0.3	--
Ceradyne Ceralloy 146I HP-SiC (2% B_4C)	1500	1.5	--

[a]General Electric data.[46]

[b]Data of Seltzer.[28,29]

[c] Computed from IITRI and Seltzer data.

104

HPSN, being typically $1.1 \pm .2$. Porosity and the fracture properties determine the useful stress levels for RS-Si_3N_4. For all forms of SiC studied, especially hot-pressed and sintered, creep rates are very low and a linear stress dependence is observed.

SECTION X

THERMAL EXPANSION

One of the reasons that Si_3N_4 and SiC are prime candidates for use in advanced gas turbine applications is their low expansion coefficient (especially Si_3N_4) and high strength, which makes them less susceptible than many other ceramics to thermal shock damage. Thermal expansion is perhaps the least variable property we have measured on these materials. It is mainly a function of the solid phase and thus not strongly affected by porosity and impurities.

Thermal expansion testing was conducted in air in an automatic recording pushrod dilatometer. Results are tabulated in Tables 15 and 16 and plotted in Figs. 46 and 47.

Definite trends exist in the thermal expansion data for the various Si_3N_4 materials. The KBI and NC-350 RSSN's that exhibit low thermal expansion are apparently not doped with a significant amount of iron to promote sintering (refer to spectographic impurity analyses as summarized in Table 7). The $RS-Si_3N_4$ materials from Ford, AiResearch, and Raytheon exhibited noticeably higher thermal expansion, and all contained ~1-2% iron additive.

Thermal expansion of the hot-pressed Si_3N_4 materials was also a function of additive. NC-132 (1% MgO) has thermal expansion very similar to the iron-doped $RS-Si_3N_4$ materials. No explanation is currently available for the lower thermal expansion obtained for the Ceradyne MgO-doped $HP-Si_3N_4$. The Y_2O_3-doped materials all have higher thermal expansion than MgO-doped materials, and the expansion increases with Y_2O_3 content. Thermal expansion in Y_2O_3-containing Si_3N_4 must be related to the particular $Y_2O_3 \cdot Si_3N_4$ phases formed. Thermal expansion is highest for the material that exhibited the most visual evidence of instability in long-term exposure tests (i.e. Ceradyne 15% Y_2O_3-doped HPSN), and lowest for NCX-34, which showed only slight

106

TABLE 15

THERMAL EXPANSION OF Si_3N_4 MATERIALS

Material	Percent Linear Expansion at 1000°C	Mean Coefficient of Thermal Expansion, 20°-1000°C, $10^{-6}/°C$
Hot-Pressed Si_3N_4		
Norton NC-132 (1% MgO)	.295	3.01
Ceradyne 147A (1% MgO)	.250	2.55
Norton NCX-34 (8% Y_2O_3)	.315	3.21
Ceradyne 147Y-1 (8% Y_2O_3)	.322	3.29
Ceradyne 147Y (15% Y_2O_3)	.385	3.93
Reaction-Sintered Si_3N_4		
Norton NC-350	.274	2.80
Kawecki-Berylco	.280	2.86
Ford (IM)	.300	3.06
AiResearch (SC) RBN-101	.297	3.03
AiResearch (IM) RBN-122	.296	3.02
Raytheon	.289	2.95

TABLE 16

THERMAL EXPANSION OF SiC MATERIALS

Material	Percent Linear Expansion at 1000°C	Mean Coefficient of Thermal Expansion, 20°-1000°C, $10^{-6}/°C$
Hot-Pressed SiC		
Ceradyne 146A (2% Al_2O_3)	.449	4.58
Ceradyne 146I (2% B_4C)	.438	4.47
Sintered SiC		
Carborundum α-SiC	.438	4.47
General Electric β-SiC	.432	4.41
Siliconized SiC		
Norton NC-435	.427	4.36
UKAEA/BNF Refel	.424	4.33
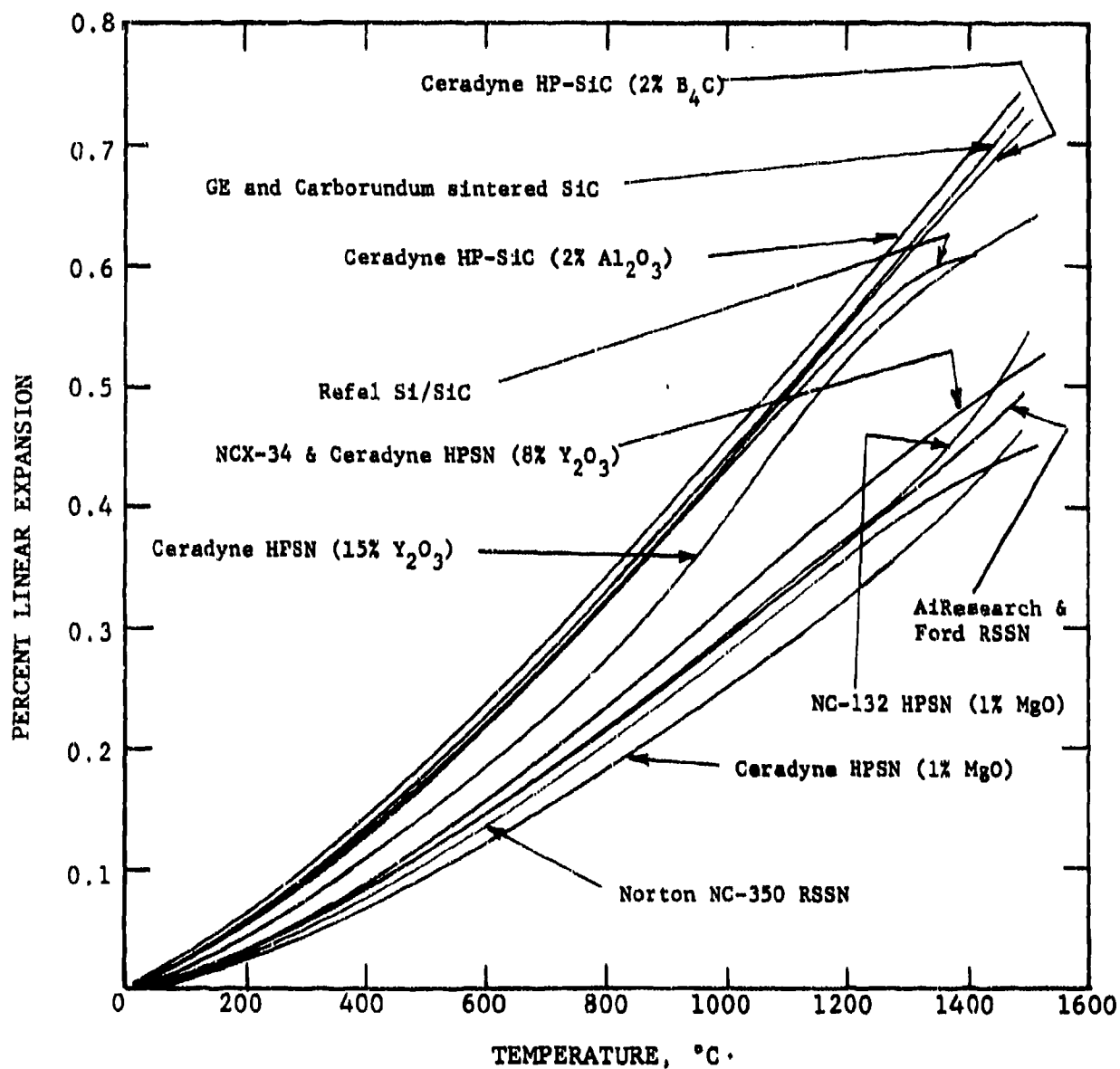
Figure 46. Thermal Expansion of Various Si_3N_4 and SiC Materials
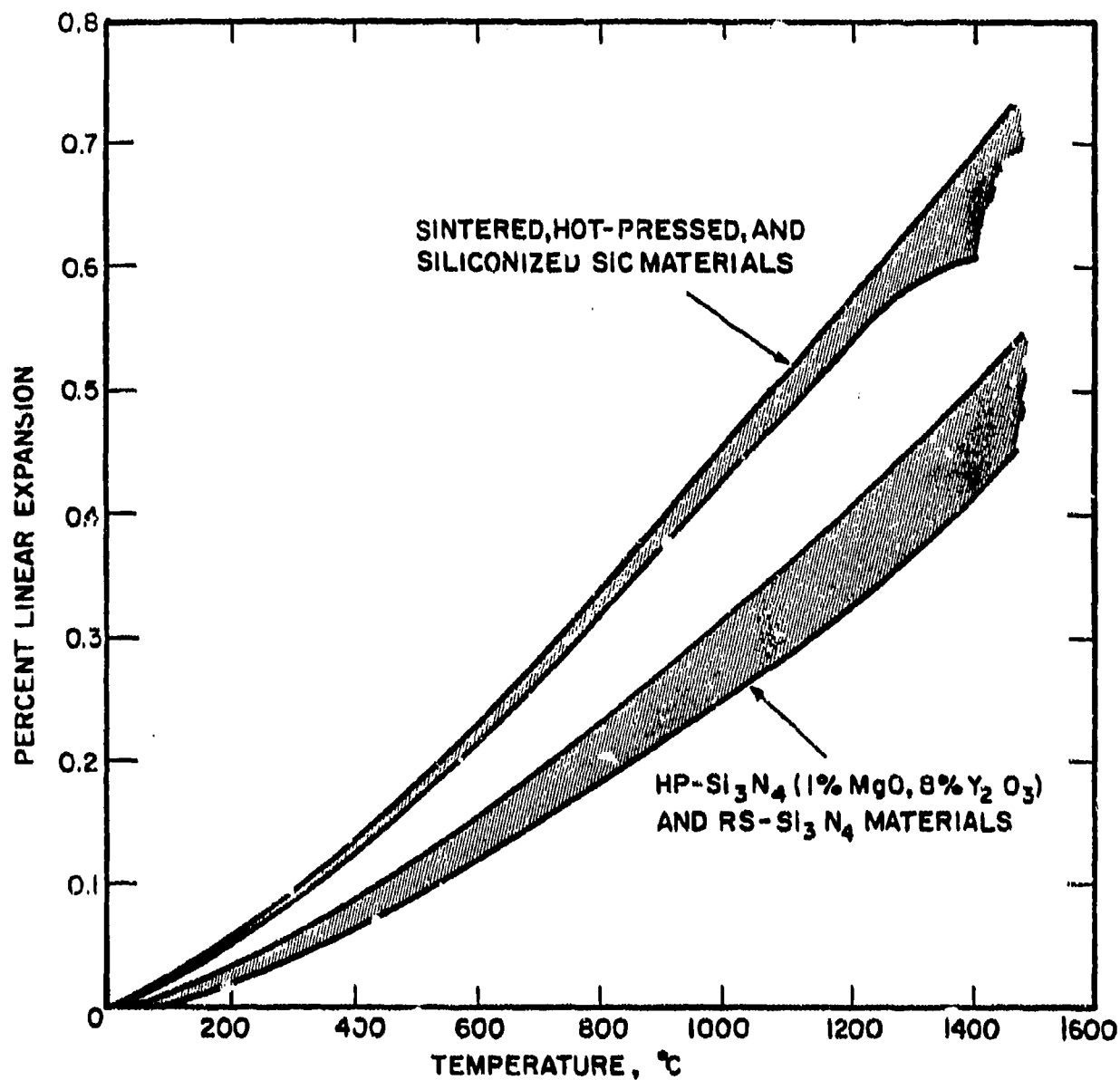
Figure 47. Thermal Expansion Data Bands for Si_3N_4 and SiC Materials

evidence of instability. The phase instability is thought to be related to a volume increase in a particular $Y_2O_3 \cdot Si_3N_4$ phase that experiences accelerated oxidation. Thus it could be inferred that the thermal expansion increase with increase in Y_2O_3 content is due to the oxidation-related instability. However, Fig. 46 illustrates that the thermal expansion of the 15% Y_2O_3-doped material is anomalously higher than the other Si_3N_4 materials even at low temperatures, where oxidation of any such unstable phase would not occur.

The silicon carbide materials evaluated were fairly predictable with regard to thermal expansion, which was significantly higher than for Si_3N_4, as expected. The Al_2O_3-doped HP-SiC had the highest expansion, most probably a result of the alumina-rich oxide grain boundary phase. The two sintered SiC materials and the B_4C-doped hot-pressed material do not have any such high expansion oxide phases. Thus they have slightly lower thermal expansion. The siliconized SiC materials have the lowest thermal expansion. This can be explained as the contribution of the lower expansion Si phase ($\sim 2.3 \times 10^{-6}/^\circ C$ [47]), which is present in an amount ~ 8-20 v/o in the siliconized SiC structure.

In summary, MgO-doped hot-pressed Si_3N_4 materials generally have slightly higher thermal expansion than reaction sintered materials due to the presence of glassy magnesium silicate grain-boundary impurity phases. The highest thermal expansion is obtained in Y_2O_3-doped HP-Si_3N_4. If as much as 15% Y_2O_3 dopant is used, expansion behavior approaches that of the SiC materials due to a phase instability promoted by accelerated oxidation. SiC materials show a fairly tight thermal expansion data band, much higher than Si_3N_4. Among the SiC materials, siliconized forms offer the lowest expansion, while oxide-doped hot-pressed forms exhibit the highest thermal expansion.

SECTION XI

THERMAL DIFFUSIVITY

Along with thermal expansion, the other thermal properties
that determine thermal stress are the thermal conductivity
and thermal diffusivity. Thermal diffusivity is a derived
property, being defined as the ratio of the thermal conductivity
to the density-specific heat product. These thermophysical
properties determine temperature distribution within a component
and thus the thermal strain field. Specific heat is a volu-
metric property, not as variable with respect to impurities and
microstructure as thermal conductivity and thermal diffusivity.

Thermal diffusivity was measured by the laser flash
method at 25°C, and at selected temperatures from ~800°C-1500°C.
Data generation at 25°C is important for predicting thermal
transients during turbine light-off. The elevated temperature
data covers the possible range of service conditions expected.
Literature data are being used to indicate behavioral trends in
the intermediate region 25 < T < 800°C. Under Contract F33615-
79-C-5100, data will be obtained for selected materials in this
region where the thermal diffusivity changes most rapidly with
temperature.

Figure 48 presents the thermal diffusivity-temperature
behavior for Norton NCX-34 HP-Si_3N_4 (8% Y_2O_3) compared to
Norton NC-132 HP-Si_3N_4 (1% MgO). The Y_2O_3-doped material has
slightly higher thermal diffusivity at 25°C, in agreement with
Gazza.[48] This apparently is the result of the yttrium-silicon
oxynitride grain-boundary phase present in NCX-34 having a
higher thermal conductivity than the magnesium silicate
boundary phase resulting from MgO addition in NC-132. At
present it is not known whether this is the result of differences
in composition or degree of crystallinity of the two boundary
phases. The Y_2O_3 additive is expected to result in a crystalline
$Y_2O_3 \cdot Si_3N_4$ grain boundary phase. Thus, higher conductivity
would be expected compared to the glassy grain boundary phase
in MgO-doped HP-Si_3N_4. At elevated temperature, however, the
thermal diffusivity of NCX-34 and NC-132 are virtually identical
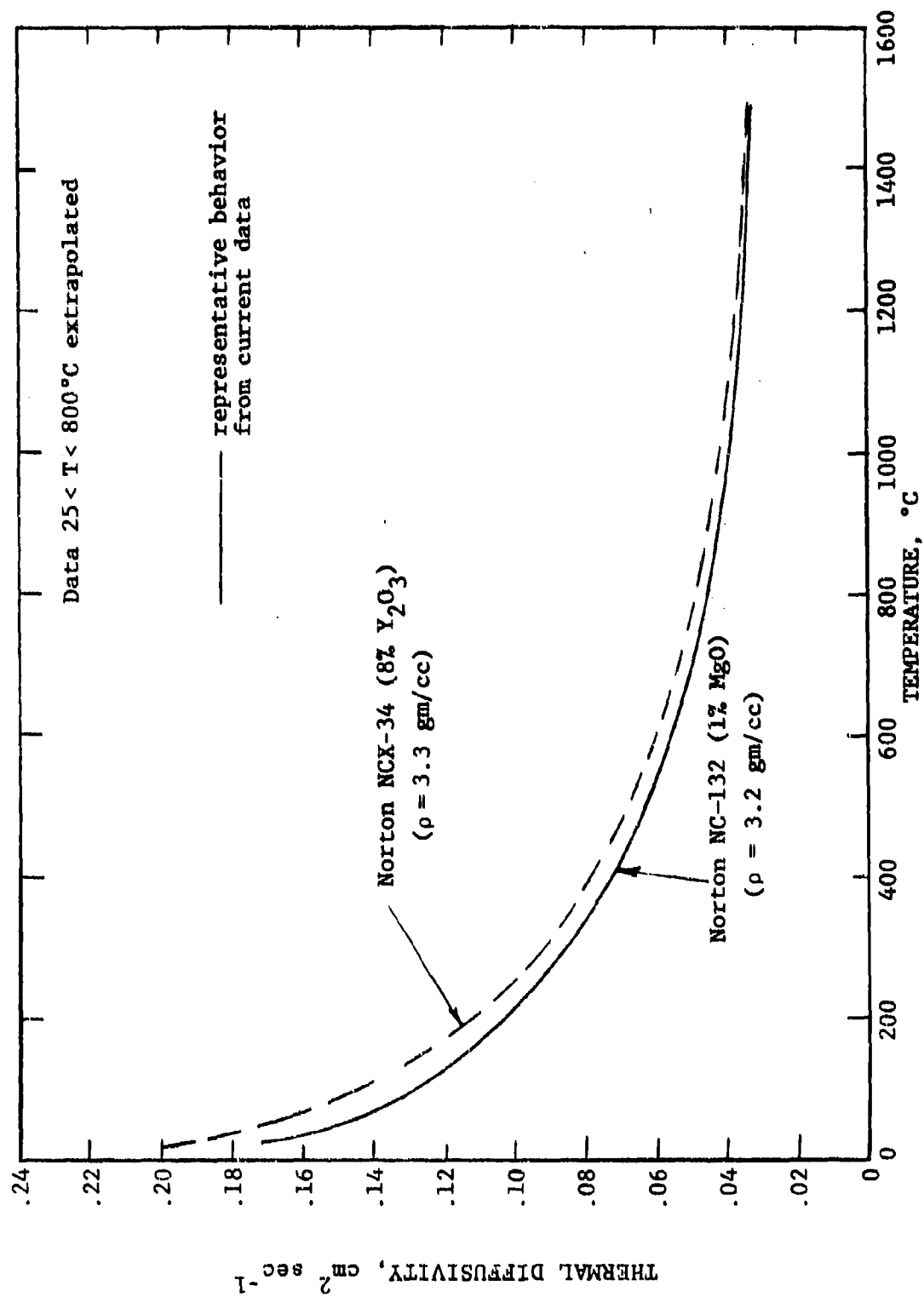as shown in Fig. 48.

112

Figure 48. Thermal Diffusivity of Hot-Pressed Si_3N_4 Materials

113

The thermal diffusivity data obtained for reaction sintered Si_3N_4 materials are shown in Fig. 49. More variability between materials is seen at room temperature than at elevated temperatures. There is a strong porosity and impurity dependence that was investigated in more detail. The room-temperature thermal diffusivity vs. theoretical density for all Si_3N_4 materials is shown in Fig. 50. Two distinct relationships are observed; one for the KBI RS-Si_3N_4 and the other for all other RSSN's and HPSN's. The KBI RS-Si_3N_4 has ~20% porosity, yet has thermal diffusivity equal to or greater than the near theoretically dense NC-132 HP-Si_3N_4. This is thought to be due to the presence of substantial unreacted silicon metal in the structure. Silicon metal has very high thermal diffusivity near room temperature.[51] As discussed in Section V, much unreacted silicon was in evidence on the fracture surface of KBI RSSN bend bars. In fact, at 1500°C the Si-phase would exude from the Si_3N_4 body in some samples. This presence of unreacted silicon would explain the anomalous thermal diffusivity obtained for the KBI material. For the other RS-Si_3N_4 materials, Fig. 50 illustrates that the density dependence accurately extrapolates to the zero-porosity values obtained for the hot-pressed materials.

Various models have been proposed for the porosity dependence of thermal conductivity of ceramic materials.[52-57] Fig. 51 presents the fractional (room-temperature) thermal conductivity vs. porosity for the RS-Si_3N_4 materials (except the Kawecki-Berylco material). The thermal conductivity of zero-porosity material, λ_o, was obtained using thermal diffusivity data for fully dense hot-pressed material (NC-132), and specific heat data from the literature.[58] Current RSSN data bests fits a conductivity-porosity model [$\lambda/\lambda_o = (1-P)/(1+18P^2)$] similar to that proposed by Aivazov and Domashnev,[59] and discussed by Rhee.[60] It is significant to note that the Loeb-Francl-Kingery,[52,53] Russell,[54] and Moore[56] models all underestimate the effect of porosity in Si_3N_4.

Representative of Present Materials
(data 25 < T < 800°C extrapolated)

——— NC-350, ρ = 2.6, Wills [49]

George,[50] RS-Si$_3$N$_4$: 0.9β/0.1α,0.05% Si, ρ = 2.8

KBI RS-Si$_3$N$_4$ (ρ = 2.5-2.7)

AiResearch Airceram (SC) RBN-101 (ρ = 2.85)

Ford (IM) RS-Si$_3$N$_4$ (ρ =2.7)

Norton NC-350 ($\bar{\rho}$ = 2.3)

Raytheon (IP)
(ρ = 2.3-2.4)

TEMPERATURE, °C

THERMAL DIFFUSIVITY, cm^2 sec^{-1}
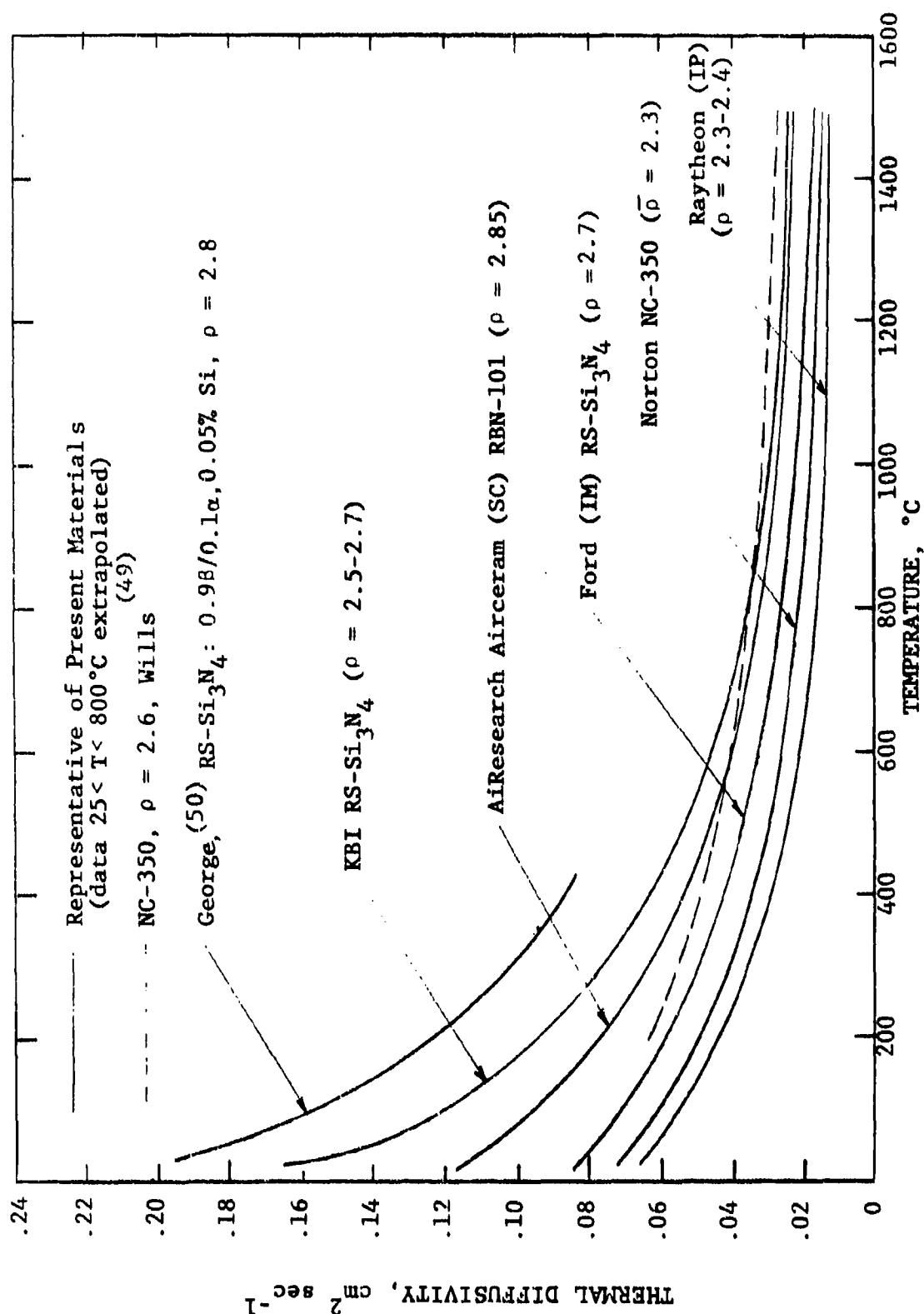
Figure 49. Thermal Diffusivity of Reaction-Sintered Si$_3$N$_4$ Materials

115

VOLUME FRACTION POROSITY
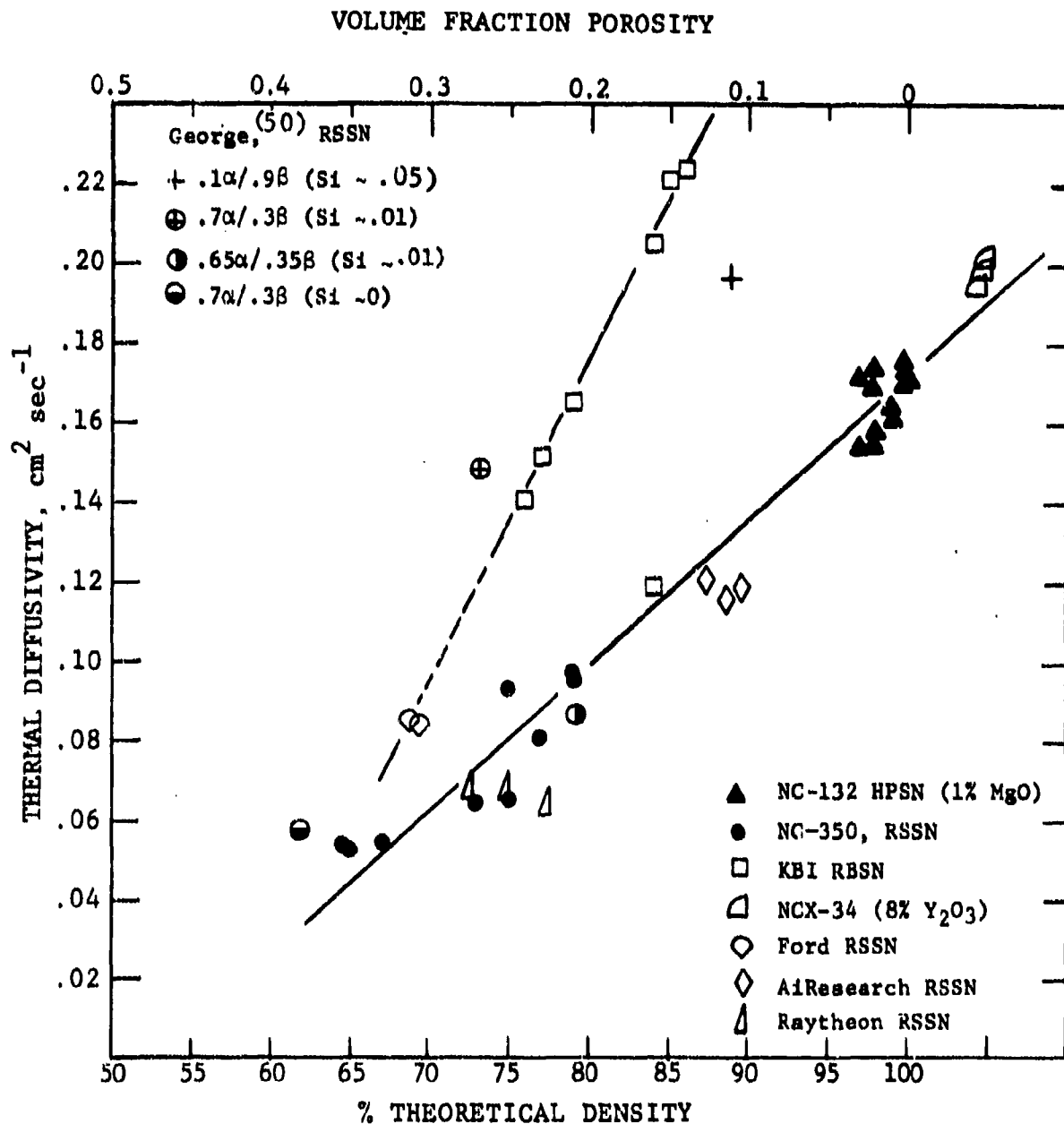
Figure 50. Correlation of Thermal Diffusivity (25°C) with Density for Si_3N_4 Materials

George,[50] RSSN
+ .1α/.9β (Si ~ .05)
⊕ .7α/.3β (Si ~.01)
◐ .65α/.35β (Si ~.01)
⬤ .7α/.3β (Si ~0)

▲ NC-132 HPSN (1% MgO)
● NC-350, RSSN
□ KBI RBSN
◁ NCX-34 (8% Y_2O_3)
◇ Ford RSSN
◇ AiResearch RSSN
◁ Raytheon RSSN

THERMAL DIFFUSIVITY, $cm^2 sec^{-1}$

% THEORETICAL DENSITY

116

Figure 51. Correlation of Room-Temperature Thermal Conductivity of Various RS-Si$_3$N$_4$ Materials with Porosity

117

The thermal diffusivity of SiC is shown in Fig. 52. The much higher values for SiC when compared to Si_3N_4 are apparently the result of the addition of a significant electronic conduction mechanism to the lattice (phonon) conduction in SiC, whereas Si_3N_4 thermal conduction is predominantly by phonon transport alone. The overall heat flow mechanisms in Si_3N_4 and SiC with respect to microstructure, purity, phase content, temperature, and composition are not well understood. Figure 52 presents the thermal diffusivity data for Refel and NC-435 Si/SiC, and Carborundum and General Electric sintered SiC. Near room temperature the temperature dependence is extremely strong for silicon carbide, the α-T curve being extremely steep. From 800° to 1500°C the thermal diffusivity levels off and all materials have about the same thermal diffusivity. An expanded scale of data in this temperature range is shown in Fig. 53. Much scatter exists near room temperature. Data for Refel SiC are very close to literature values.[61] However, current data for General Electric and Carborundum sintered SiC materials are much higher than data published by the respective vendors.[63,66] At present it is not known whether this is the result of differences in purity (e.g., silicon content), microstructure (e.g., grain size), crystal structure, temperature, etc.

In summary, Fig. 54 presents thermal diffusivity data bands for various types of silicon-base ceramics. Fig. 55 illustrates the shape of the thermal conductivity-temperature relation for a few specific materials. Si_3N_4 materials have relatively low conductivity. Their properties are strongly affected by porosity (decreases conductivity) and free silicon content (increases conductivity), especially at low temperatures. Thermal diffusivity decreases with temperature. Above 800°C the temperature dependence is not too strong, and there is less variability between materials. HP-Si_3N_4 generally has higher conductivity than RS-Si_3N_4 due to higher density.
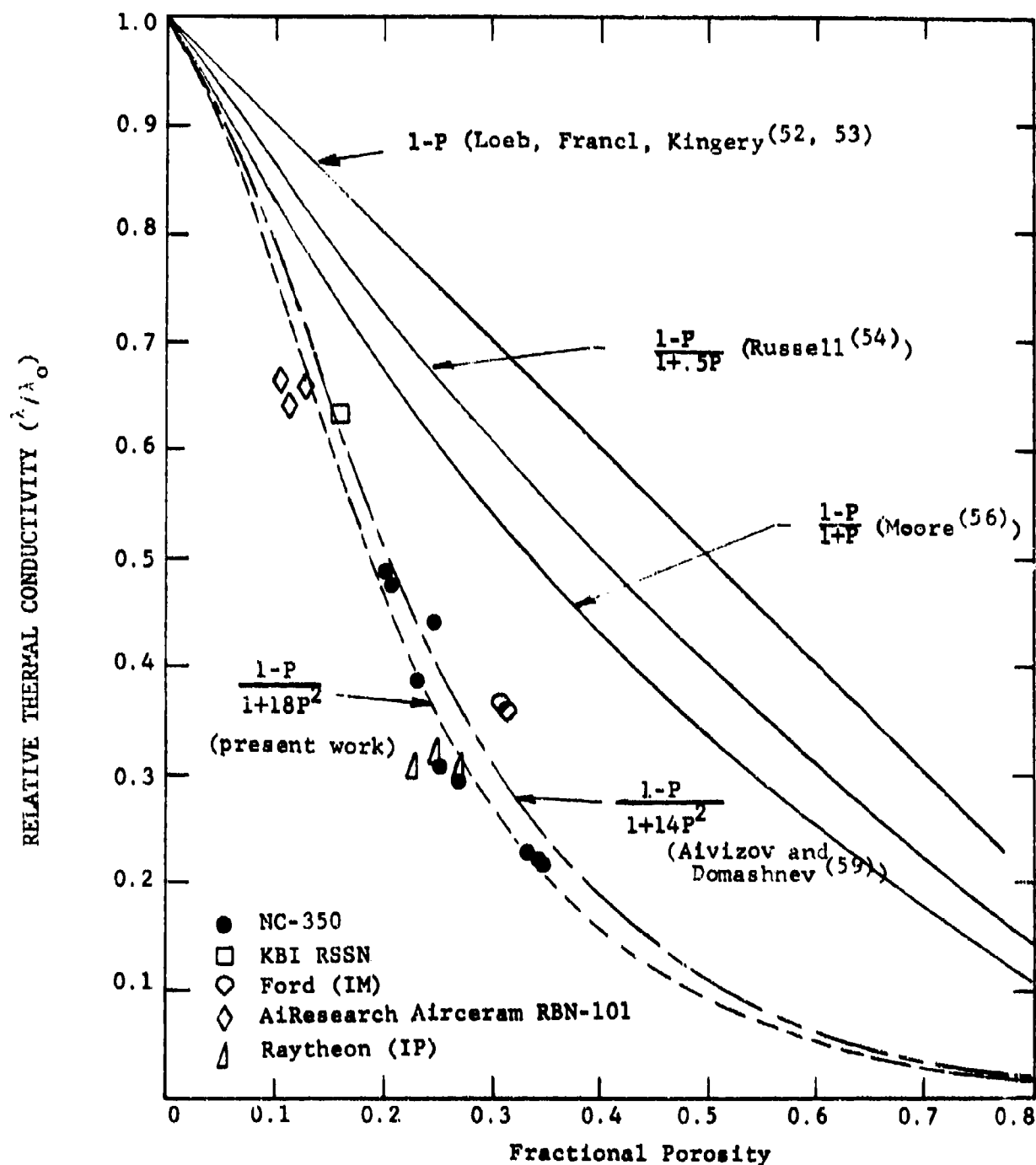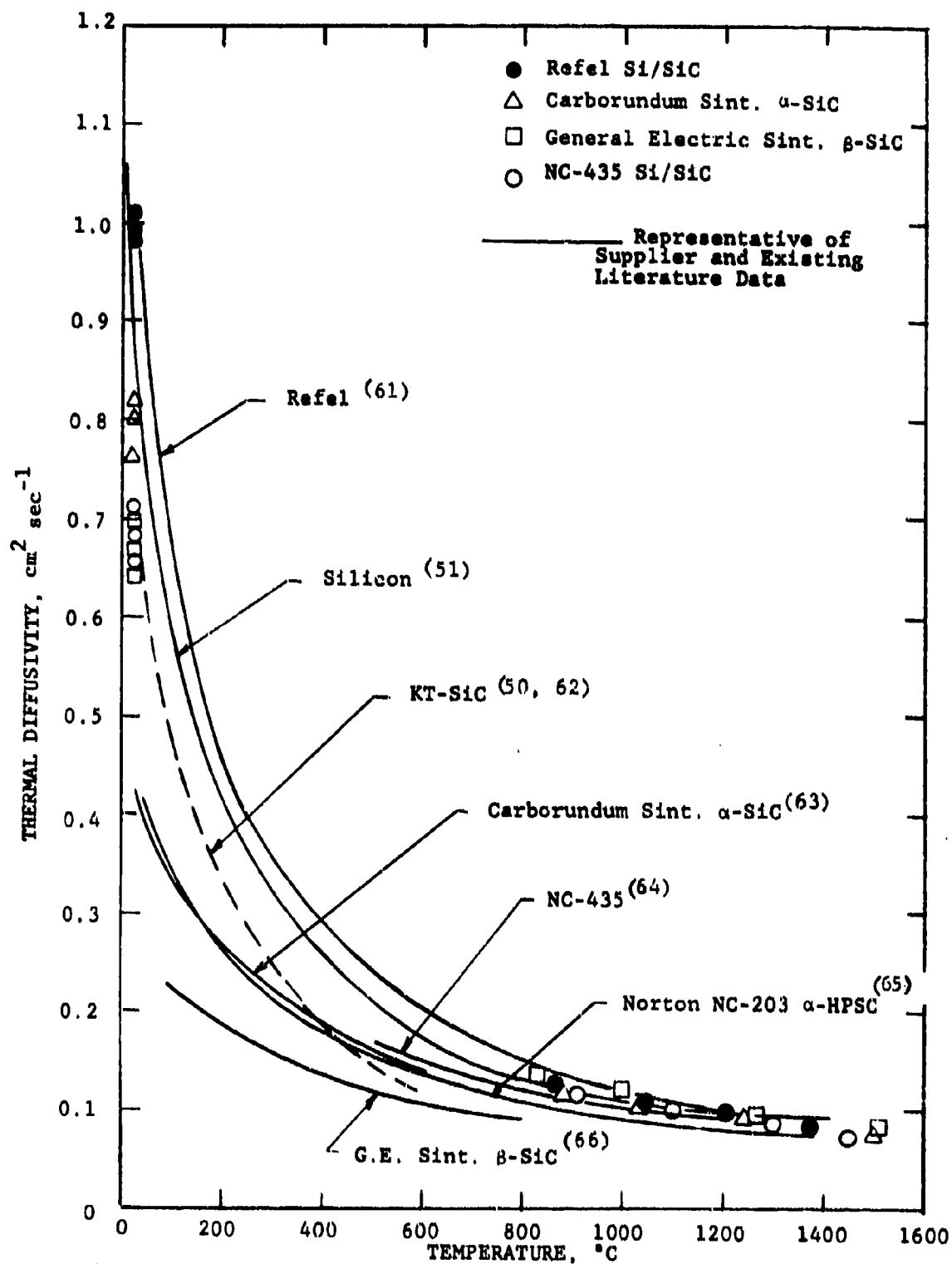
Figure 52. Thermal Diffusivity of Various SiC Materials
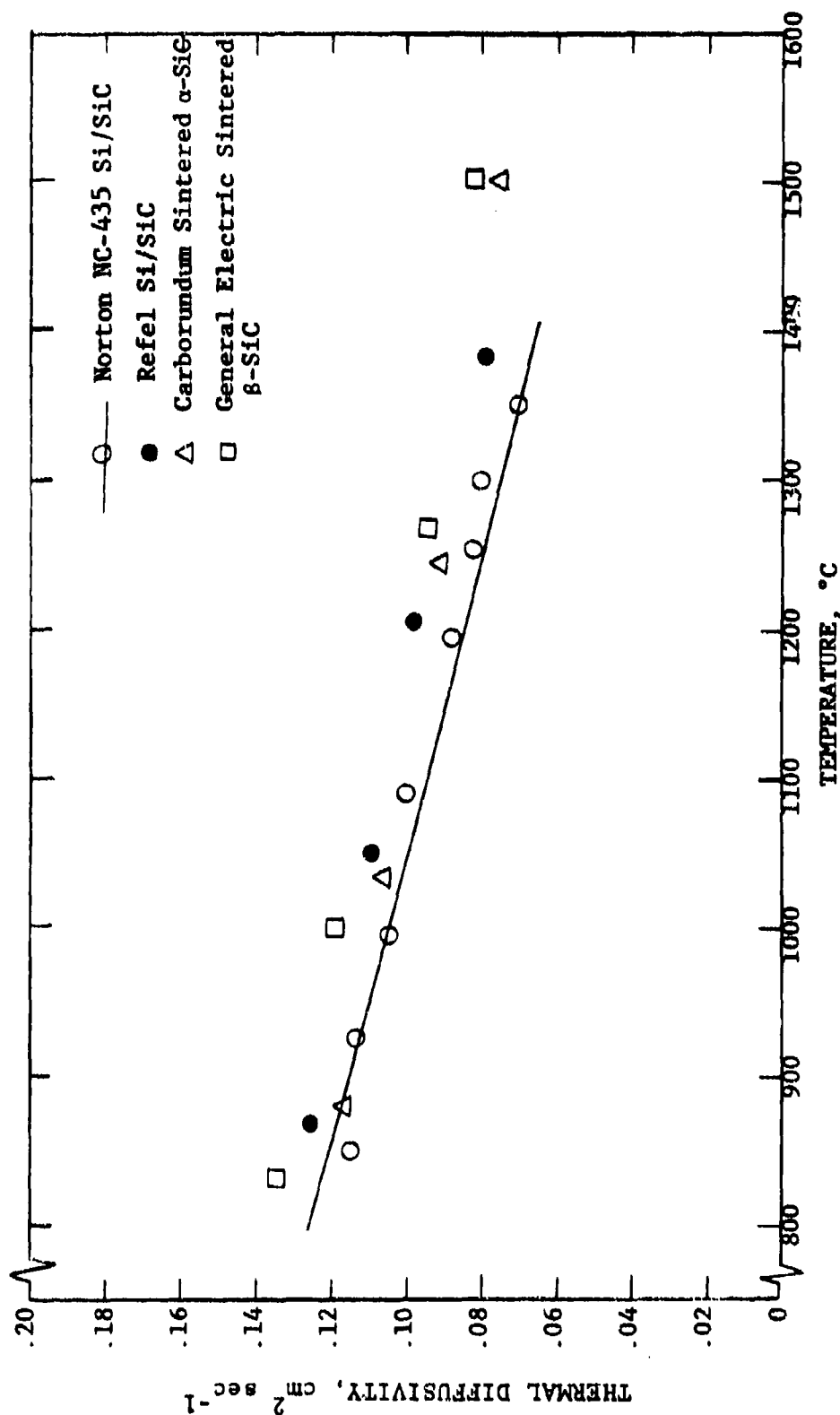
Figure 53. High-Temperature Thermal Diffusivity of SiC Materials

120
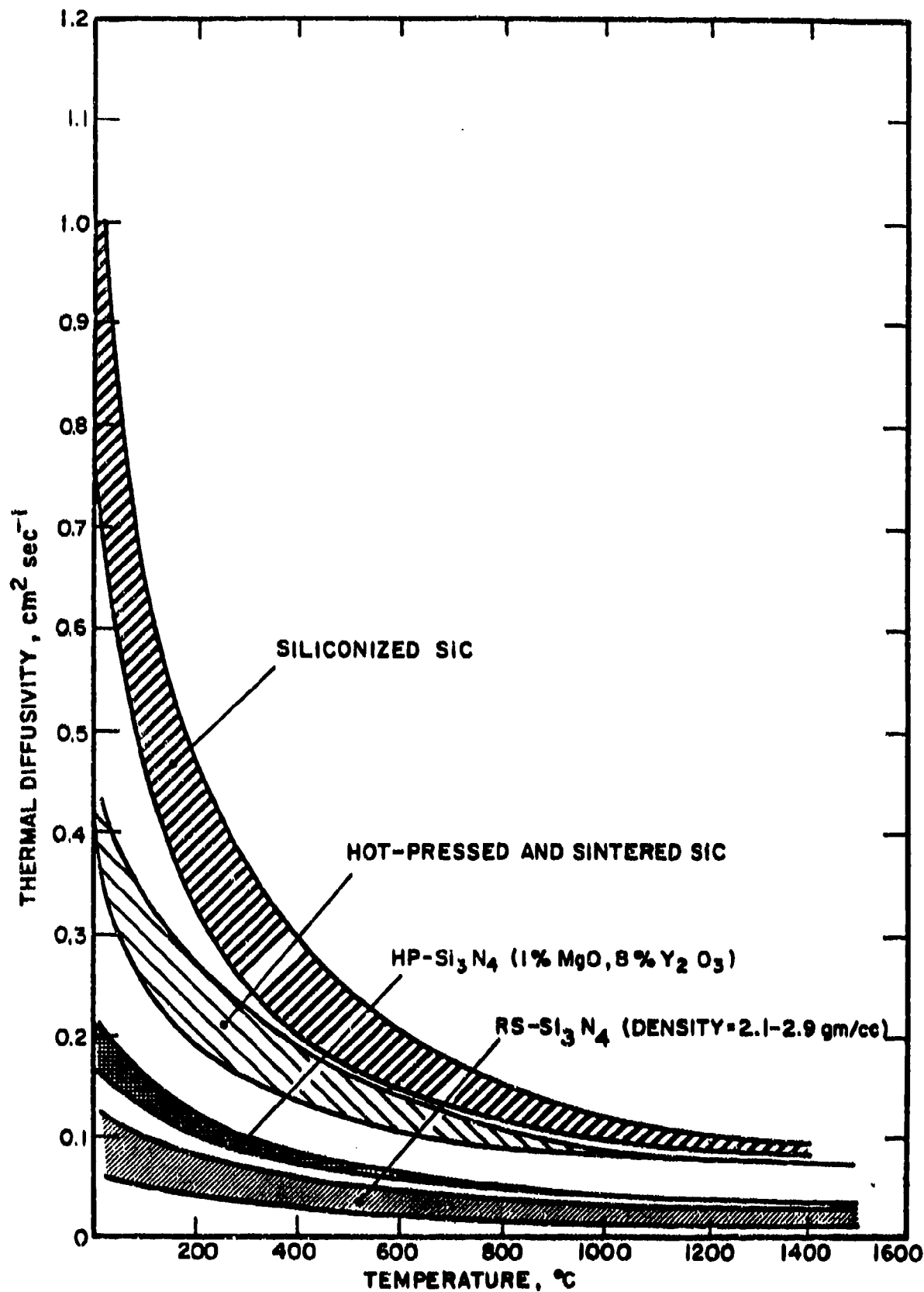
Figure 54. Thermal Diffusivity of Silicon Ceramics

121
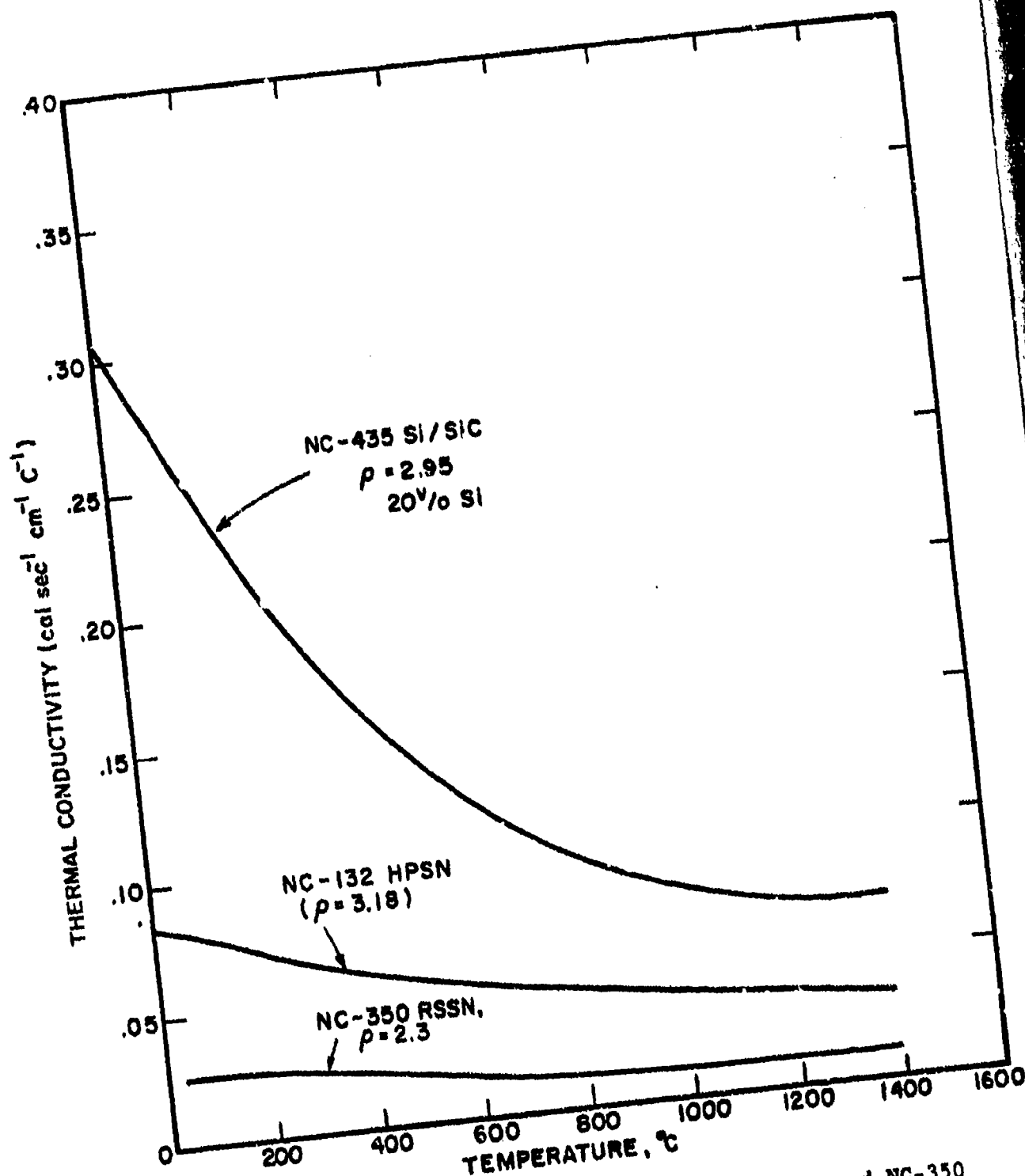
Figure 55. Thermal Conductivity of NC-132, NC-435, and NC-350 Materials

122

However, at low temperature RSSN can have unexpectedly high conductivity if substantial unreacted silicon metal is present in the structure.

Silicon carbide has much higher thermal diffusivity (and therefore thermal conductivity) than Si_3N_4, especially at low temperatures. The temperature dependence is extremely strong near room temperature. Much data variability exists at 25°C where the exact roles of grain size, purity, crystal phase, etc., are not well understood for SiC. At elevated temperature very little scatter exists and the temperature dependence is relatively small.

It is noted that the difference in thermal diffusivity or thermal conductivity between SiC and Si_3N_4 is most apparent at low temperature. Thus, thermal transients in turbine components made from SiC vs. Si_3N_4 would be most critical during light-off rather than during a flame-out. This effect could be offset, however, by the fact that during light-off (severe thermal upshock) component surfaces are in compression, and thus are significantly stronger than the surfaces during the severe downshock of a flame-out, where component surfaces are in tension.

SECTION XII

THERMAL SHOCK RESISTANCE

The ability to withstand the thermal stresses generated during ignition and flameout is an important consideration in evaluating potential ceramic turbine materials. Thermally created stresses may initiate a fracture which can result in a catastrophic failure, or cause existing flaws to grow giving a gradual loss of strength and eventual loss of component integrity (i.e., spalling). However, the evaluation of thermal stress resistance is a complex task since performance is dependent not only on material thermal and mechanical properties, but is also influenced by heat transfer and geometric factors as well (i.e., heat transfer coefficient and component size).

Determination of the true relative thermal stress resistance of a group of materials in this application would require an actual (or closely simulative) turbine environment. This is rarely done in practice for economic reasons. The problem with laboratory thermal shock evaluations is that the conditions of the experimental test are not at all near expected service life conditions. Thus, the designer has a problem in predicting actual thermal stress resistance. Alternatively, if thermal shock investigations are conducted that attempt to be closely simulative of expected in-service conditions, then results are difficult to compare to laboratory experimental results where the temperature and stress distributions are more well known.

Thermal stress resistance is often analytically computed from a material's thermal and mechanical properties using various thermal stress resistance parameters that have been developed for a variety of heat transfer conditions.[67] Some of the commonly used analytical thermal stress resistance parameters are presented in Table 17.

TABLE 17

THERMAL STRESS RESISTANCE PARAMETERS[67]

LITERATURE DESIGNATION	PARAMETER TYPE	PARAMETERS	PHYSICAL INTERPRETATION/ENVIRONMENT	TYPICAL UNITS
R	Resistance to Fracture Initiation	$\dfrac{\sigma_t(1-\mu)}{\alpha E}$	Maximum ΔT allowable for steady heat flow;	$^\circ C$
R'	Resistance to Fracture Initiation	$\dfrac{\sigma_t(1-\mu)k}{\alpha E}$	Maximum heat flux for steady flow;	$cal \; \ldots \; sec^{-1}$
R''	Resistance to Fracture Initiation	$\dfrac{\sigma_t(1-\mu)\alpha_{TH}}{\alpha E}$	Maximum allowable rate of surface heating;	$cm^{-1}{}^\circ C\; sec^{-1}$
R'''	Resistance to Propagation Damage	$\dfrac{E}{\sigma^2(1-\mu)}$	Minimum in elastic energy at fracture available for crack propagation	$(psi)^{-1}$
R''''	Resistance to Propagation Damage	$\dfrac{\gamma E}{\sigma^2(1-\mu)}$	Minimum in extent of crack propagation on initiation of thermal stress fracture	m
R_{st}	Resistance to further crack propagation	$\left[\dfrac{\gamma}{\alpha^2 E}\right]^{1/2}$	Minimum ΔT allowed for propagation long cracks	$^\circ Cm^{-1/2}$

σ_t = Tensile Strength

μ = Poisson's ratio

α = Coefficient of Thermal Expansion

E = Young's Modulus of Elasticity

ρ = Density

C_p = Specific Heat

k = Thermal Conductivity

α_{TH} = Thermal Diffusivity

γ = Fracture Surface Energy

125

Water quench thermal shock tests are often used to compare relative materials performance. This test is not ideal, but can yield valuable screening-type data. This is especially true if such tests are supplemented by high velocity rig test exposures. The combination of these two types of tests will not provide design data, but will aid greatly in initial materials selection and properties screening.

On this program thermal shock resistance was determined by the water quench method, with the initiation of thermal shock damage being detected by internal friction measurement. In conducting this test, internal friction was measured before and after water quench from successively higher temperatures using the flexural resonant frequency Zener bandwidth method. A marked change in internal friction (specific damping capacity) indicated the c   of thermal shock damage (i.e., thermal stress induced crack initiation). This defined the critical quench temperature difference, ΔT_c, which was compared to analytical thermal stress resistance parameters. The parameter which is most applicable to the experimental severe water quench is $R = \sigma(1-\mu)/\alpha E$. The details, interpretation, and limitations of this overall procedure for assessing relative thermal shock resistance were discussed in the semi-annual reports issued on this program.

Tables 18-20 compile the pertinent properties of each material tested to date. The computed R value for each material represents the maximum ΔT allowable before thermal shock initiation, and is compared with experimentally obtained ΔT_c in Tables 18-20 for hot-pressed Si_3N_4, reaction-sintered Si_3N_4, and SiC materials, respectively. The Kawecki-Berylco RSSN was interpreted as behaving in a quasi-static manner, while all other materials behaved in a kinetic manner. This basically means that silicon-base ceramics are normally

TABLE 18

THERMAL STRESS RESISTANCE PARAMETERS FOR HOT-PRESSED Si_3N_4 MATERIALS

Material	Flexural[a] Strength (ksi)	Poisson's[b] Ratio	Thermal[c] Expansion $(10^{-6}/°C)$	Elastic Modulus $(10^6$ psi)	$R = \sigma(1-\mu)/\alpha E$ [d] (°C)	ΔT_c [e] (ΔQ^{-1}) (°C)
Norton NC-132 HPSN (1% MgO)	103.1	0.27	2.50	47.1	639	600
Norton NCX-34 HPSN (8% Y_2O_3)	126.7	0.27	2.63	48.6	724	600-800
Ceradyne 147A HPSN (1% MgO)	87.1	0.27	1.95	47.9	581	500-600
Ceradyne 147Y-1 HPSN (8% Y_2O_3)	83.3	0.29	2.61	45.4	499	500-700
Ceradyne 147Y HPSN (15% Y_2O_3)	87.6	0.28	3.0	44.7	470	400-500

NOTES: (a) All properties at 25°C, unless otherwise noted; computed average of all samples tested; note that
4-point bend strength is used instead of tensile strength.

  (b) Determined at AFML by resonant sphere technique, unless otherwise indicated

  (c) At 500°C

  (d) Analytical thermal stress resistance parameter; maximum ΔT allowable for steady heat flow

  (e) Critical ΔT determined by change in internal friction in water quench tests.

127

TABLE 19

THERMAL STRESS RESISTANCE PARAMETERS FOR REACTION-SINTERED Si_3N_4 MATERIALS

Material	Flexural Strength (ksi) [a]	Poisson's Ratio [b]	Thermal Expansion $(10^{-6}/°C)$ [c]	Elastic Modulus $(10^6$ psi$)$	$R = \sigma(1-\mu)/\alpha E$ (°C) [d]	ΔT_c (ΔQ^{-1}) (°C) [e]
Norton NC-350 RSSN	29.5	0.22	2.29	25.6	393	400-500
Kawecki-Berylco RSSN	21.1	0.24	2.30	20.9	334	600-800
Ford (IM) RSSN	38.2	0.25	2.48	30.7	376	350-450
AiResearch (SC) Airceram RBN-101	37.9	0.24	2.42	32.0	372	400-600
AiResearch (IM) Airceram RBN-122	32.6	0.23	2.44	30.2	341	350-400
Raytheon (TP) RSSN	21.6	0.24(est.)	2.41	23.8	286	~400

Notes: (a) All properties at 25°C, unless otherwise noted; computed average of all samples tested; note that 4-point bend strength is used instead of tensile strength

(b) Determined at AFML by resonant sphere technique, unless otherwise indicated

(c) At 500°C

(d) Analytical thermal stress resistance parameter; maximum ΔT allowable for steady heat flow

(e) Critical ΔT determined by change in internal friction in water quench tests.

128

TABLE 20

THERMAL STRESS RESISTANCE PARAMETERS FOR SILICON CARBIDE MATERIALS

Material	Flexural Strength (ksi)[a]	Poisson's Ratio[b]	Thermal[c] Expansion (10^-6/°C)	Elastic Modulus (10^6 psi)	$R = \sigma(1-\mu)/\alpha E$ (°C)[d]	ΔT_c[e] (ΔQ^{-1}) (°C)
Norton NC-435 Si/SiC	57.2	0.17	3.83	50.7	244	350–400
Carborundum Sint. α-SiC	44.2	0.16	3.8	58.2	168	300
General Electric Sint. β-SiC	63.8	0.16	3.78	54.8	259	375–400
UKAEA/BNF Refel Si/SiC	44.9	0.17	3.79	57.5	171	300–400
UKAEA/BNF Refel Si/SiC (as processed)	33.6	0.17	3.79	52.5	140	—
Ceradyne 146A HP-SiC (2% Al₂O₃)	60.1	0.16	4.0	67.2	188	~300 (est.)
Ceradyne 146I HP-SiC (2% B₄C)	45.6	0.16 (est.)	3.89	65.3	151	300

Notes: (a) All properties at 25°C, unless otherwise noted; computed average of all samples tested; note that 4-point bend strength is used instead of tensile strength.
(b) Determined at AFML by resonant sphere technique, unless otherwise indicated.
(c) At 560°C.
(d) Analytical thermal stress resistance parameter; maximum ΔT allowable for steady heat flow.
(e) Critical ΔT determined by change in internal friction in water quench test.

well sintered and fail catastrophically; the KBI material
was not well sintered and exhibited a much more gradual
damage and crack propagation. The concepts of quasi-static
and kinetic crack propagation were developed by Hasselman.[68]
His theory unified consideration of thermal stress fracture
initiation and the degree of component or sample damage due
to subsequent crack propagation. He showed the materials
parameters required to give greatest resistance to
thermal stress fracture initiation (high strength, low Young's
modulus, high thermal conductivity, low thermal expansion,
etc.) are, in general, mutually exclusive to the requirements
providing greatest resistance to crack propagation and component
damage due to thermal stresses (low strength, high modulus,
high fracture surface energy, etc.). These properties and
the behavior of a component experiencing thermally created
stresses are influenced by the initial size and density of
cracks or flaws (i.e., the total flaw structure of the component).
This structure affects the components ability to store elastic
thermal strain energy, the driving force for crack propagation.
In general, a component resistant to fracture has a low flaw
density, so once a sufficiently high stress level (or level
of stress intensity) is obtained in such a material, its
high stored energy causes the most deleterious flaw to propa-
gate catastrophically or in a kinetic manner. This occurs
because the energy release rate is greater than that needed
to merely balance fracture surface energy. Resistance to
thermal stress damage means the component is resistant to
crack propagation, as opposed to fracture initiation. When
cracks are propagated due to thermal stresses in such a case,
the propagation is quasi-static in that only enough crack
length is generated to absorb the available strain energy. The
rate of strain energy release is lower and less strain energy
is available as a driving force for propagation. This usually
occurs in a more highly flawed component. The above discussion

130

shows why internal friction, as a measure of total flaw structure, is useful in monitoring thermal shock performance.

Analytical and experimental results obtained on this program are directly compared in Fig. 56. The trend line shown is a linear least squares regression data fit for all materials (except KBI RSSN). Very predictable behavior is seen in comparing the analytical and experimental behavior of the sixteen (16) silicon carbide and silicon nitride materials. Good agreement is obtained between analytical and experimental results. Comparison of the materials properties tabulated in Tables 18-20, and the analytical-experimental thermal shock relationship shown in Fig. 56, permits relative ranking of materials. The silicon carbides are the least thermal shock resistant (ΔT_c = 300-400°C) due to their high elastic modulus and thermal expansion. The hot-pressed silicon nitrides exhibit the highest thermal shock resistance (ΔT_c = 500-700°C) due to their lower modulus and thermal expansion (compared to the carbides) and their high strength (when compared to RSSNs which exhibit ΔT_c = 350-500°C). Norton NCX-34 HP-Si_3N_4 (8% Y_2O_3) is seen to be the most thermal shock resistant material evaluated on this program. However, none of the Y_2O_3-doped HPSNs currently evaluated showed the degree of improved thermal shock resistance over MgO-doped HP-Si_3N_4 that Weaver and Lucek[69] have found for NCX-34 vs. NC-132. Recall that this was also the case for the flexure data obtained on this program. The best reaction-sintered material evaluated herein was Norton NC-350 RS-Si_3N_4. This is consistent with the strength and oxidation studies conducted on this program, and results from the fact that NC-350 is highly pure, has small and uniformly distributed porosity, and uniform fine grain microstructure.
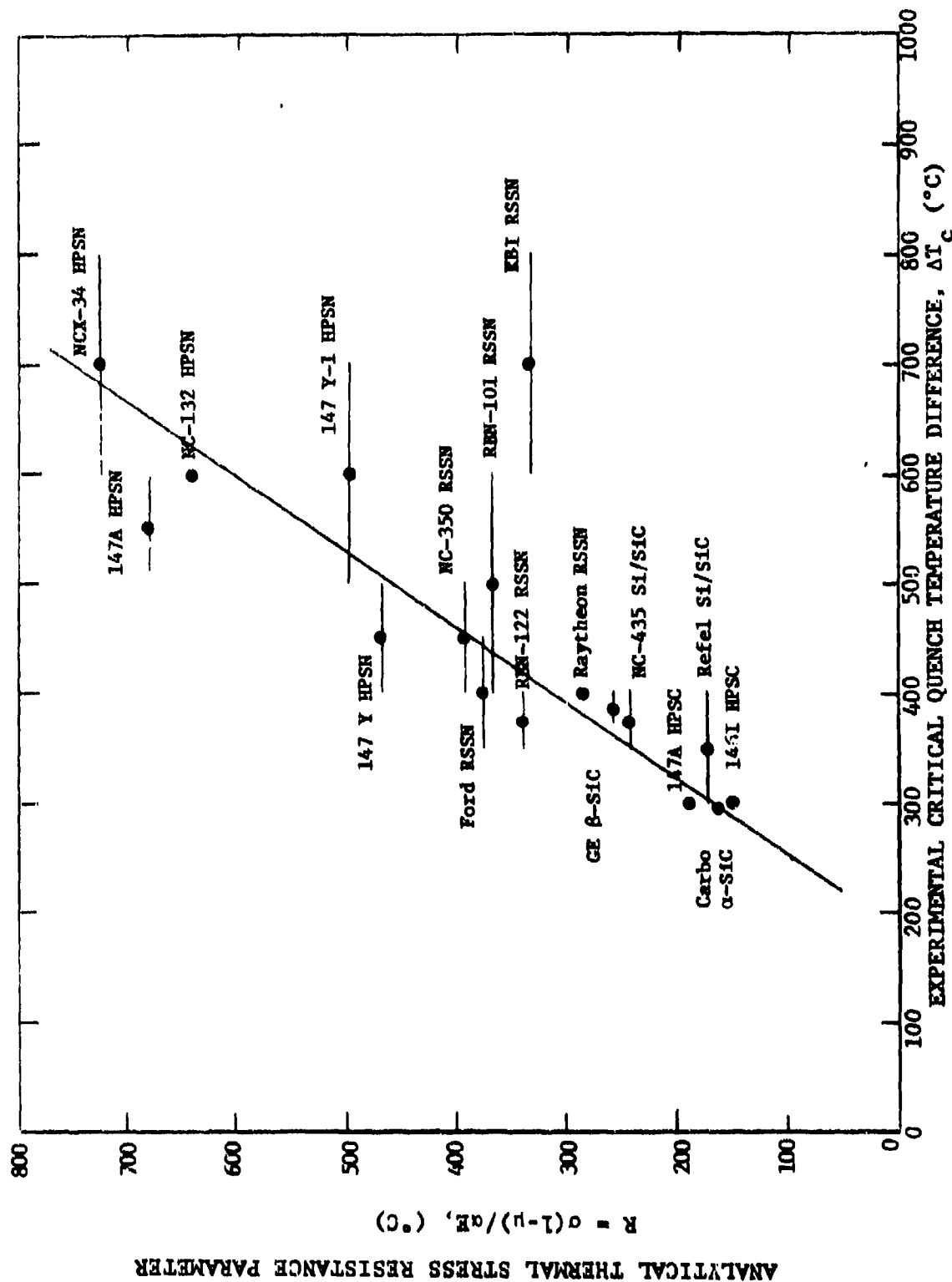
Figure 56   Analytical Vs. Experimental Thermal Shock Results for Various
Si₃N₄ and SiC Materials

132

SECTION XIII

FUTURE WORK

A program with the same objective and scope as this program has been initiated under AFML Contract F33615-79-C-5100. The following materials either have already been supplied to the Air Force for this work, or are expected to be supplied:

- Norton NC-203 HP-SiC (2% Al_2O_3)
- Annawerk Ceranox NR-115H RS-Si_3N_4
- Fiber Materials, Inc. HP-Si_3N_4 (4% MgO)
- Associated Engineering Developments, Nitrasil RS-Si_3N_4
- Norton NC-350 RS-Si_3N_4 (newest version)
- Harbison-Walker HP-Si_3N_4 (10% CeO_2)
- Norton NC-430 SiC (siliconized)
- AiResearch (IM) Sintered Si_3N_4 (8% Y_2O_3, 4% Al_2O_3)[a]
- AFML Developmental HP-Si_3N_4 (with CeO_2, BN additions)
- Chemetal CVD AlN and CNTD SiC
- Coors Si/SiC
- Kyocera Sintered SiC, Sintered Si_3N_4 (Y_2O_3), and RS-Si_3N_4
- GTE Sintered Si_3N_4 (6% Y_2O_3)
- Kawecki-Berylco RS-Si_3N_4

Additionally attempts are being made to obtain the following materials:

- Toshiba, Sintered Si_3N_4 (Y_2O_3, Al_2O_3)
- Annawerk, additional SiC and Si_3N_4
- Carborundum, Sintered α-SiC, others
- AiResearch Casting, SSC and SSN
- University of Washington, RSSN
- Keyes/Lucas, Sialon
- Westinghouse, various
- Rocketdyne - RSSN
- DCI, CVD-SiC
- USAMMRC, HP-Si_3N_4, Sintered Si_3N_4

---

[a]Fabricated on AFML Contract F33615-77-C-5064

SECTION XIV

CONCLUDING REMARKS

This program and its follow-on (Contract F33615-79-C-5100) support current systems design and demonstration efforts by 1) screening candidate materials; 2) generating engineering data on a wide number of properties of available and emerging silicon-base ceramics; 3) interpreting the behavioral mechanisms; and 4) disseminating the information to the various government agencies and their industrial contractors working in this area.

Some of the challenges faced in using silicon-based ceramics in advanced heat engine applications include: dealing with the statistical nature of these brittle materials; low fracture toughness and surface sensitivity; the existence of subcritical crack growth; the lack of data regarding the environmental effects of oxidation, corrosion, erosion, and deposition from the fuel; batch-to-batch variability resulting from inadequate process control; and the lack of an NDE technology capable of detecting strength-controlling critical flaws in test bars or components.

These challenges are compounded by the fact that new candidate materials for advanced heat engine applications are continually emerging, and their properties are strongly dependent on microstructure, purity, and processing history.

Available Si_3N_4 and SiC bodies represent a large family of materials with wide property variation and broad response characteristics during interaction with severe environments. Even though some are termed commercially available, they are in a continual state of development and change. In general, property differences between materials are directly related to: 1) existence of secondary phases; 2) purity; 3) microstructural aspects such as pore size and distribution, grain size, etc.; 4) oxidation rates; 5) phase stability; 6) microstructural stability; 7) existence of subcritical crack growth,

134

and 8) the nature of the critical strength-controlling flaws
(e.g., contaminant inclusions, pores/pore agglomerates, large
grains, unreacted particles, etc.) and how critical flaws
change with time, temperature, and environmental exposure.

REFERENCES

1. M.G. Mendiratta et al. "Fractography of Reaction-Sintered Si3N4," ASME Paper 79-GT-97, 1978.

2. "Ceramic Components for Turbine Engines," Second Interim (Quarterly) Technical Report, AiResearch, Air Force Contract F33615-77-C-5171, June 5, 1978.

3. J.A. Rubin, Ceradyne, Inc., private communication.

4. M. Srinivasan, R.H. Smoak, and J.A. Coppola, "Static Fatigue Resistance of Sintered Alpha SiC," Paper 10-C-79C presented at the American Ceramic Society 3rd Annual Conference on Composites and Advanced Materials, January 21-24, 1979, Merritt Island, Florida.

5. K.D. McHenry, and R.E. Tressler, "Subcritical Crack Growth in Silicon Carbide," Jour. Matls. Sci. 12 1272-78 (1977).

6. G.G. Trantina and C.A. Johnson, "Subcritical Crack Growth-Measurements for Silicon Carbide and Use in Design," G.E. Report No. 75CRD197, September 1975.

7. C.A. Johnson and S. Prochazka, "Investigation of Ceramics for High Temperature Turbine Components," Navy Contract N62269-76-C-0243, General Electric Report SRD-77-145 (June 1977).

8. A.G. Evans and F.F. Lange, "Crack Propagation and Fracture in Silicon Carbide," Jour. Matls. Sci. 10 1659-64 (1975).

9. G.G. Trantina and C.A. Johnson, "Subcritical Crack Growth in Boron-Doped SiC," Jour. Amer. Ceram. Soc. 58 (7-8), 344-5 (1975).

10. A.G. Evans and S.M. Wiederhorn, "Crack Propagation and Failure Prediction in Silicon Nitride at Elevated Temperatures," Jour. Matls. Sci. 9 (2) 270-8 (1974).

11. N.J. Tighe and S.M. Wiederhorn, "Fracture of Brittle Materials at High Temperature," AFML-TR-78-83 (July 1976).

12. S.C. Singhal, "Oxidation of Silicon Nitride and Related Materials," Nitrogen Ceramics, Ed. F.L. Riley, Proceedings of NATO Advanced Study Institute on Nitrogen Ceramics, University of Kent, Canterbury, U.K., August 1976.

13. S C. Singhal, "Oxidation and Corrosion-Erosion Behavior of Si3N4 and SiC," published in Ceramics for High Performance Applications, Ed. J.J. Burke, A.E. Gorum, and R.N. Katz, Brookhill Publishing Co., 1974.

14. W.C. Tripp and H.C. Graham, "Oxidation of Si_3N_4 in the Range 1300° to 1500°C," Jour. Amer. Ceram. Soc. 59 (9-10) 399-403 (1976).

15. S.C. Singhal, "Thermodynamics and Kinetics of Oxidation of Hot-pressed Silicon Nitride," Jour. Matl. Sci., 11 500-509 (1976).

16. S.C. Singhal and F.F. Lange, "Effect of Alumina Content on the Oxidation of Hot-pressed Silicon Carbide," Jour. Amer. Ceram. Soc. 58 (9-10) 1975.

17. J.W. Hinze, W.C. Tripp, and H.C. Graham, "The High Temperature Oxidation of Hot-pressed Silicon Carbide," in Mass Transport Phenomena in Ceramics, Eds. A.R. Cooper and A.H. Heuer, Plenum Press (1975).

18. S.C. Singhal, "Oxidation Kinetics of Hot-pressed Silicon Carbide," Jour. Matl. Sci. 11 1246-53 (1976).

19. S.C. Singhal, "Thermodynamic Analysis of the High-Temperature Stability of Silicon Nitride and Silicon Carbide," Ceramurgia Intl. 2(3) 123-30 (1976).

20. A.J. Kiehle, et al., "Oxidation Behavior of Hot-pressed Si_3N_4," Jour. Amer. Ceram. Soc. 58 (1-2) 17-20 (1975).

21. F.F. Lange and S.C. Singhal, "Si_3N_4-Y_2O_3 System: Effect of Oxidation on Stability" for abstract see Bull. Amer. Ceram. Soc. 54(8) 741, (1975).

22. R.R. Wills, et al., "Stability of the Silicon Yttrium Oxynitrides," Jour. Amer. Ceram. Soc. 59 (5-6) 269-70 (1976).

23. F.F Lange, S.C. Singhal, and R.C. Kuznicki, "Phase Relations and Stability Studies in the Si_3N_4-SiO_2-Y_2O_3 Pseudoternary System," Jour. Amer. Ceram. Soc. 60 (5-6) 249-52 (1977).

24. G.E. Gazza, "Effect of Yttria Additions on Hot-pressed Si_3N_4," Bull. Amer. Ceram. Soc. 54(9) 778-81 (1975).

25 G.Q. Weaver and J.W. Lucek, "Optimization of Hot-pressed Si_3N_4-Y_2O_3 Materials," Bull. Amer. Ceram. Soc. 57(12) 113-36 (1978).

26. G. Gazza, H. Knoch, and G.D. Quinn, "Hot-pressed Si_3N_4 with Improved Thermal Stability," Bull. Amer. Ceram. Soc. 57(11) 1059-60 (1978).

27. M.V. Lawn, "A Note on the Residual Stress About a Pointed Impression in Brittle Solid," Jour. Matl. Sci. 11, 2345-48 (1976).

28. M.S. Seltzer, "High Temperature Creep of Ceramics," AFML-TR12-76-97, June 1976.

29. M.S. Seltzer, "High Temperature Creep of Silicon-Base Compounds," Bull. Amer. Ceram. Soc. $\underline{56}$(4) pp. 418-423 (1977).

30. S. Ud Din and P.S. Nicholson, "Creep of Hot-pressed Silicon Nitride," Jour. Matl. Sci. $\underline{10}$, 1375-80, (1975).

31. R. Kossowsky, D.G. Miller, and E.S. Diaz, "Tensile and Creep Strengths of Hot-Pressed Si_3N_4," Jour. Matl. Sci., $\underline{10}$ 983-97, 1975.

32. T.G. Langdon et. al., "Creep Mechanisms in Ceramic Materials at Elevated Temperatures," Ceramics in Severe Environments, W. Kriegel and H. Palmour, III, Eds., pp. 297-313, Plenum Press (1971).

33. T.G. Langdon, "Grain Boundary Deformation Processes," Deformation of Ceramic Materials, pp. 101-126, R.C. Bradt and R.E. Tressler, Eds., Plenum Press (1975).

34. T.G. Langdon, "The Significance of Grain Boundaries in High Temperature Creep," Canadian Metallurgical Quarterly $\underline{13}$(1) 223-8, (1974).

35. R. Kossowsky, "The Microstructure of Hot Pressed Silicon-Nitride," Westinghouse Research Laboratories Scientific Paper 73-9D4-Foram-P2 (February 22, 1973).

36. J.A. Mangels, "Development of a Creep-Resistant Reaction Sintered Si_3N_4," pp. 195-206, Ceramics for High-Performance Applications, J.J. Burke, et al., Eds., Brookhill (1974).

37. S. Ud Din and P.S. Nicholson, "Creep Deformation of Reaction Sintered Silicon Nitrides," Jour. Amer. Ceram. Soc., $\underline{58}$ (11-12) 500-2 (1975).

38. S. Grathwohl and F. Thürmler, "Creep of Reaction-Bonded Silicon Nitride," Jour. Matl. Sci. $\underline{13}$, pp. 1177-86 (1978).

39. T.G. Langdon, "Dependence of Creep Rate on Porosity," Jour. Amer. Ceram. Soc., $\underline{55}$(12) pp. 630-1 (1972).

40. J.M. Birch and B. Wilshire, "The Compression Creep Behavior of Silicon Nitride Ceramics," Jour. Matl. Sci. $\underline{13}$, pp. 2627-36 (1978).

41 J.M. Birch et al., "The Influence of Stress Distribution on the Deformation and Fracture Behavior of Ceramic Materials Under Compression Creep Conditions," Jour. Matl. Sci. $\underline{11}$ pp. 1817-25 (1976).

42. F.F. Lange, "Non-Elastic Deformation of Polycrystals with a Liquid Boundary Phase," in <u>Deformation of Ceramic Materials</u>, R.C. Bradt and R.E. Tressler, Eds., Plenum Press, New York (1975).

43. T.L. Francis and R.L. Coble, "Creep of Polycrystalline Silicon Carbide," Jour. Amer. Ceram. Soc., <u>51</u>(2) pp. 115-6 (1968).

44. P.L. Farnsworth and R.L. Coble, "Deformation Behavior of Dense Polycrystalline SiC," Jour. Amer. Ceram. Soc. <u>49</u>(5), pp. 264-8 (1966).

45. S. Prochazka, "Investigation of Ceramics for High-Temperature Turbine Vanes," G.E. Report SRD-72-171, Final Report on Navy Contract N00019-72-C-0129, December 1972.

46. R.J. Charles, "High-Temperature Stress Rupture of Polycrystalline Ceramics," General Electric Report 77-CRD-036, May 1977.

47. <u>ASME Metals Handbook</u>, Vol. 1, "Properties and Selection of Metals," 8th Edition, Lyman Taylor, Editor, p. 1222.

48. G.E. Gazza, "Effect of Yttria Additions on Hot-Pressed Si_3N_4," Bull. Amer. Ceram. Soc. <u>54</u>(9), pp. 778-81, 1975.

49. R.R. Wills, R.W. Stewart, and J.M. Wimmer, "Instrinsic Thermal and Mechanical Properties of Reaction-Sintered $Si_4Al_2N_6O_2$ Sialon," Bull. Amer. Ceram. Soc. <u>55</u>(11) 1976.

50. W. George, "Thermal Property Measurement on Silicon Nitride and Silicon Carbide Ceramics Between 290° and 700°K," Proc. Brit. Ceram. Soc., <u>Ceramics for Turbines and Other High-Temperature Engineering Applications</u>, Proceedings 22, pp. 147-167, June 1973.

51. Y.S. Touloukian, R.W. Powell, C.Y. Ho, and M.C. Nicolaou, <u>Thermophysical Properties of Matter</u>, <u>Thermal Diffusivity</u>, Vol. 10, IFI/Plenum (1973).

52. A.L. Loeb, "Thermal Conductivity VIII: A Theory of Thermal Conductivity of Porous Materials," Jour. Amer. Ceram. Soc. <u>37</u> (2, Part II) pp. 96-9 (1954).

53. J. Francl and W.D. Kingery, "Thermal Conductivity IX: Experimental Investigation of Effect of Porosity on Thermal Conductivity," ibid. pp. 99-107.

54. H.W. Russell, "Principles of Heat Flow in Porous Materials," Jour. Amer. Ceram. Soc. <u>18</u>, pp. 1-5 (1935).

55. S.C. Cheng and R.I. Vachon, "A Technique for Predicting the Thermal Conductivity of Suspensions, Emulsions, and Porous Materials," Intl. Jour. Heat Mass Transfer 13 pp. 537-46 (1970).

56. J.P. Moore, cited by D.J. Godfrey and E.R.W. May, "The Resistance of Silicon-Nitride Ceramics to Thermal Shock and other Hostile Environments," in Ceramics in Severe Environments, Materials Science Research, Vol. 5, W.W. Kriegel and H. Palmour, III, Editors, Plenum Press, pp. 149-62 (1971).

57. A. Eucken, "Thermal Conductivity of Ceramic Refractory Materials; Calculation from Thermal Conductivity of Constituents," Forsch, Geb. Ing. Wes. B3, Forschungsheft No. 353, 16 (1932), Ceram Abstr. 11, 576 (1932); 12, 231 (1933).

58. A.F. McLean, et al., "Brittle Materials Design, High Temperature Gas Turbine," AMMRC-CTR-73-9 (March 1973).

59. M.I. Aivazov and I.A. Domashnev, Poroshkovaya Met. 8, 51 (1968).

60. S.K. Rhee, "Porosity-Thermal Conductivity Correlations for Ceramic Materials," Matl. Sci. and Engr. 20, pp. 89-93 (1975).

61. P. Kennedy, et al., "An Assessment of the Performance of Refel Silicon Carbide Under Conditions of Thermal Stress," Proc. Brit. Ceram. Soc., No. 22, pp. 67-87 (June 1973).

62. Carborundum Company, product information literature.

63. J.A. Coppola and C.H. McMurtry, "Substitution of Ceramics for Ductile Materials in Design," paper presented at National Symposium on Ceramics in the Service of Man, Washington, D.C. (June 7, 1976).

64. R.K. Bart, Norton Company, Worcester, Mass., private communication.

65. A.F. McLean, et al., "Brittle Materials Design, High Temperature Gas Turbine," AMMRC-CTR-73-32, (Sept. 1973).

66. S. Prochazka, R.A. Giddings, and C.A. Johnson, "Investigation of Ceramics for High Temperature Turbine Components," General Electric Report SRD-74-123 on Navy Contract N62269-74-C-0255 (November 1974).

67. D.P.H. Hasselman, "Thermal Stress Resistance Parameters for Brittle Refractory Ceramics: A Compendium," Bull. Amer. Ceram. Soc., 49, pp. 1033-37 (1970).

68. D.P.H. Hasselman, "Unified Theory of Thermal Shock Fracture Initiation and Crack Propagation in Brittle Ceramics," Jour. Amer. Ceram. Soc., $\underline{52}$, pp. 600-04 (1969).

69. G.Q. Weaver and J.W. Lucek, "Optimization of $Si_3N_4-Y_2O_3$ Materials," Bull. Amer. Ceram. Soc. $\underline{57}$(12), pp. 1131-36 (1978).